Journal of Physics D:
Applied Physics

PURPOSE-LED PUBLISHING™

TOPICAL REVIEW • OPEN ACCESS

Vertical spintronic devices based on half-metallic Heusler alloys: progress and future outlook

To cite this article: Yuya Sakuraba *et al* 2026 *J. Phys. D: Appl. Phys.* **59** 253003

View the article online for updates and enhancements.

You may also like

- Non-Hermitian cavity magnonics for microwave applications: PT/anti-PT symmetry, complex photon–magnon coupling, and spectral singularities
Junyoung Kim, Bojong Kim and Sang-Koog Kim
- Comparative study on highly anisotropic piezo-active 1–1–3 composites: effects of auxetic polymer and fibrous structures
Vitaly Yu Topolov and Sofya A Kovrigina
- CORRIGENDUM: Electrically tunable permanent dipole moment switching in fullerene: encapsulated water for single: molecule electronics (2025 *J. Phys. D.: Appl. Phys.* 58 385302)
Ying Song, Jing Yang, Yu Zhou et al.

This content was downloaded from IP address 159.28.194.189 on 27/06/2026 at 17:40

Journal of Physics D: Applied Physics

Check for updates

OPEN ACCESS

RECEIVED
3 March 2026

REVISED
9 April 2026

ACCEPTED FOR PUBLICATION
27 May 2026

PUBLISHED
25 June 2026

Original content from this work may be used under the terms of the Creative Commons Attribution 4.0 licence.

Any further distribution of this work must maintain attribution to the author(s) and the title of the work, journal citation and DOI.

TOPICAL REVIEW

Vertical spintronic devices based on half-metallic Heusler alloys: progress and future outlook

Yuya Sakuraba[1,*], **Shinya Yamada**[2,3], **Hirofumi Suto**[1], **Tomoya Nakatani**[1] and **Kohei Hamaya**[2,3]

[1] Research Center for Magnetic and Spintronic Materials, National Institute for Materials Science, Tsukuba, Ibaraki 305-0047, Japan
[2] Center for Spintronics Research Network, Graduate School of Engineering Science, The University of Osaka, Toyonaka, Osaka 560-8531, Japan
[3] Spintronics Research Network Division, Institute for Open and Transdisciplinary Research Initiatives, The University of Osaka, Suita, Osaka 565-0871, Japan
[*] Author to whom any correspondence should be addressed.

E-mail: SAKURABA.Yuya@nims.go.jp and yamada.shinya.es@osaka-u.ac.jp

Keywords: half-metal, Heusler alloy, magnetic tunnel junctions, giant magnetoresistance, spin-transistor

Abstract

Half-metallic Heusler alloys are among the most promising material platforms for spintronics, as they uniquely combine an ideally fully spin-polarized electronic structure at the Fermi level with high Curie temperatures. This combination enables pronounced spin-dependent phenomena and makes these materials highly attractive for practical device applications. To date, vertical spintronic devices such as magnetic tunnel junctions, current-perpendicular-to-plane giant magnetoresistance and spin-torque oscillator devices have demonstrated outstanding performance that clearly reflects the half-metallic nature of Heusler alloys. In addition, significant progress has been achieved in efficient spin injection into semiconductors, a key requirement for next-generation logic and information-processing devices. In this review, we focus on vertical-geometry spintronic devices, which are of particular importance from the viewpoint of device scaling, integration density, and practical implementation. We provide an overview of the experimental and theoretical advances achieved using half-metallic Heusler alloys in these device architectures, and discuss the remaining challenges and future perspectives toward their realization in next-generation spintronic technologies.

1. Introduction

A half-metal is a material in which an energy gap exists at the Fermi level for one spin channel (either spin-up or spin-down), while the other spin channel remains metallic. Owing to this unique electronic structure, half-metals ideally generate fully spin-polarized conduction electrons, thereby strongly enhancing a wide range of spin-dependent phenomena. For example, in magnetic tunnel junctions (MTJs), as described by the Jullière formula [1], a spin polarization $P = 1$ of the magnetic electrodes leads, in principle, to an infinite tunnel magnetoresistance (TMR) ratio:

$$\mathrm{TMR} = \frac{2P_1P_2}{1 - P_1P_2}.$$

Similarly, in current-perpendicular-to-plane giant magnetoresistance (CPP-GMR) devices, the product of the resistance change ΔR and the device area A, denoted as, is given within the two-current model [2]:

$$\Delta RA \propto \frac{\beta^2}{1-\beta^2}\rho_{\mathrm{F}}t + \frac{\gamma^2}{1-\gamma^2}R_{\mathrm{F/N}}A.$$

Here, β and γ represent the spin polarizations of the bulk resistivity of the ferromagnet (FM), respectively. t and $R_{\mathrm{F/N}}A$ represent the thickness of ferromagnetic electrode and the interfacial resistance at the FM/nonmagnet interface, respectively. In an ideal half-metal, both parameters approach unity,

© 2026 The Author(s). Published by IOP Publishing Ltd

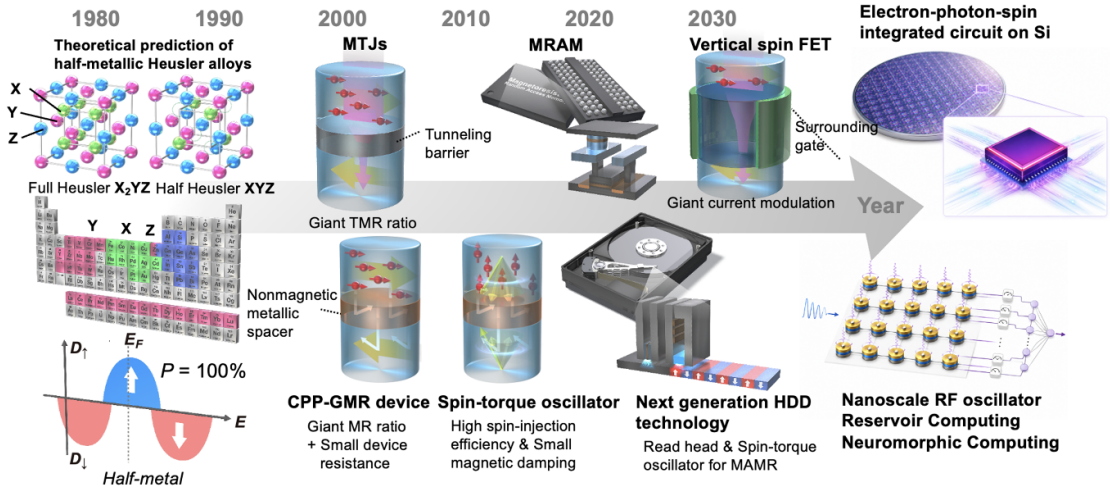


Figure 1. Technology development of the vertical spintronic devices using half-metallic Heusler alloys and future prospects.

resulting in a maximized output signal. Beyond magnetoresistive effects, half-metals are also expected to provide significant advantages for spintronic devices, including enhanced spin-transfer torque (STT) efficiencies [3], highly efficient spin injection into semiconductors (SCs) [4], and reduced magnetic damping [5] and so on. In this sense, half-metals can be regarded as 'ultimate spintronic materials' enabling enhancement of various spin-dependent phenomena and improvement in device performance.

The history of half-metal research dates back to 1983, when de Groot *et al* predicted half-metallicity in the half-Heusler alloy NiMnSb based on first-principles calculations [6] (figure 1)—well before the discovery of GMR [7, 8] and the subsequent rise of spintronics. In the 1990s, driven by rapid developments in spintronics, a variety of half-metallic materials were theoretically proposed, including oxide-based systems such as CrO_2 [9], $La_{1-x}Sr_xMnO_3$ (LSMO) and $La_{1-x}Ca_xMnO_3$ [10] m Fe_3O [11], and Heusler alloys [12] which are the main focus of this review. Notable experimental demonstrations followed these predictions. For instance, in CrO_2 spin polarization as high as 91% at 2 K was observed using Andreev reflection measurements [13]. In LSMO-based MTJs, an extremely large TMR ratio of 1800% was reported at 2 K [14]. However, many oxide-based half metals suffer from relatively low Curie temperatures, which poses a fundamental limitation for practical applications.

In contrast, Co-based full-Heusler alloys exhibit high Curie temperatures such as Co_2YZ (Y = Cr, Mn and Fe etc. Z = Al, Si, Ga, Ge, and Sn etc) and comparatively robust half-metallicity against atomic disorder and off-stoichiometric compositions [15–17]. Owing to these favorable properties, The Co-based full-Heusler alloys have become the central materials platform for half-metal research since the early 2000s. In particular, MTJs and CPP-GMR devices employing Heusler alloys have yielded numerous results that clearly reflect their half-metallic nature, raising strong expectations for applications in practical devices such as next-generation hard-disk-drive (HDD) read heads. Furthermore, spin transistors that integrate SCs with magnetic materials are regarded as key components for future nonvolatile and reconfigurable logic devices. Among various architectures, vertical devices incorporating a SC spacer layer are especially well suited to exploit the highly efficient spin injection enabled by half-metallic electrodes (figure 1).

Because comprehensive review articles covering the very wide fundamental aspects of half-metallicity in Heusler alloys already exist [18], the present review does not revisit these foundational topics. Instead, we focus on vertical spintronic devices that are of particular importance for next-generation applications, and provide an overview of the advantages, challenges, and future prospects of devices based on half-metallic Heusler-alloys.

2. MTJs with half-metallic electrode

As discussed in the previous chapter, the Jullière model provides the most straightforward guideline for enhancing the TMR ratio. According to this model, the TMR ratio increases monotonically with the spin-polarization P of the FM electrodes, and, in the ideal case of a half-metallic FM with $P = 100\%$, an infinite TMR ratio is predicted. Motivated by this expectation, extensive studies on TMR devices employing half-metallic materials have been actively pursued since the 1990s.

In the early stage of their research, half-metallic electrodes were primarily combined with amorphous tunnel barriers, typically Al–O-based barriers, which were dominant at that time. A major breakthrough occurred in 2002 with the introduction of crystalline MgO tunnel barriers, where coherent tunneling enables symmetry-selective transmission of the Δ_1 band [19, 20]. As a result, giant TMR ratios reflecting the spin polarization of the Δ_1 band at the Fermi level were reported in epitaxial systems such as Fe/MgO/Fe and CoFe/MgO/CoFe [21, 22]. Following these findings, considerable efforts were devoted to fabricating devices that combine half-metallicity with coherent tunneling by integrating half-metallic materials with MgO tunnel barriers.

As shown in figure 2, it was theoretically predicted that representative half-metallic Co-based full-Heusler alloys, such as the Co_2FeAl, Co_2FeSi, Co_2MnAl and Co_2MnSi families, possess Δ_1 bands in the majority-spin channel at the Fermi level. This unique band structure suggests that coherent tunneling through the MgO barrier can enhance the TMR ratio. In such systems, the intrinsically high spin polarization of Heusler alloys is further enhanced by the spin-filtering effect associated with coherent tunneling, leading to the expectation of even larger TMR ratios, which is advantageous to the conventional Fe/MgO/Fe-MTJs where the finite tunneling current appears even in anti-parallel state [19]. Despite these promising characteristics, the most critical issue for TMR devices based on Heusler alloys, as discussed later, is their pronounced temperature dependence of the TMR ratio. In addition, from the viewpoint of magnetic random-access memory (MRAM) applications, it remains challenging to realize perpendicular MTJs (pMTJs) using conventional Heusler alloys. This difficulty originates from a fundamental limitation: the cubic crystal structure of Heusler alloys inherently makes it difficult to achieve sufficiently large magnetocrystalline anisotropy. To overcome this limitation, significant attention has been directed toward the compounds with the $D0_{22}$ phase, so called 'tetragonal Heusler alloys' because these compounds retain the same atomic arrangement as conventional Heusler alloys but exhibit a uniaxial distortion from the cubic symmetry. For example, large magnetic anisotropy has been theoretically predicted and experimentally confirmed in $D0_{22}$-Mn_3Ga [23]. At present, TMR devices employing such tetragonal Heusler alloys represent a growing trend in this research field.

In this section, progress, issues and future outlook in the studies on the MTJ with half-metallic Heusler alloys and tetragonal Heusler alloys are introduced.

2.1. MTJs with cubic half-metallic Heusler alloys

Table 1 summarizes the TMR ratios reported so far for MTJs using half-metallic Heusler alloy electrodes. In the following chapters, we review the progress of MTJs with each Heusler alloy, discuss the remaining challenges, and finally outline possible future directions and strategies for further improvement.

2.1.1. NiMnSb-based MTJ

Research on MTJs employing half-metallic Heusler alloy as electrodes was initiated by the work of Tanaka *et al* using polycrystalline NiMnSb half-Heusler alloy electrodes with the Cl_b structure combined with an Al–O tunnel barrier in 1997 [24]. They reported TMR ratios of 2.4% at room temperature (RT) and 7.0% at 77 K, and estimated the spin polarization to be approximately 15%. The authors attributed the reduced TMR ratio primarily to the formation of oxides at the interface. Liu *et al* fabricated the MTJs with epitaxial NiMnSb made by molecular beam epitaxy (MBE) technique and found a TMR ratio of 8.7% at RT and 14.7 at 4.2 K [25], which was still smaller than the expected value from its predicted half-metallic electronic state. To date, studies on MTJs utilizing $C1_b$-structured Heusler alloys remain extremely limited, and no systematic experimental investigations have followed. However, theoretical calculations have shown that in $C1_b$ half-Heusler alloys, the presence of vacancy sites leads to a larger minority-spin bandgap compared with $L2_1$-type full-Heusler alloys [52]. Although controlling atomic ordering in $C1_b$-NiMnSb containing vacancy sites is often challenging in the thin films, if flat and highly atomic ordered single-crystalline electrodes can be realized, the combination with the recent tunnel-barrier growth techniques may enable the achievement of larger TMR ratios that reflect the intrinsic half-metallicity.

2.1.2. Co_2CrAl-based MTJ

Co_2CrAl was predicted to exhibit half-metallicity based on first-principles calculations [53]; however, it was later demonstrated that this compound undergoes spinodal decomposition and consequently phase-separates [54]. It was subsequently shown that substituting more than 40% of Cr with Fe effectively suppresses this phase separation [54], and theoretical studies further predicted that high spin polarization exceeding 70% can be achieved not only in the $L2_1$-ordered structure but also in the B2 structure, in

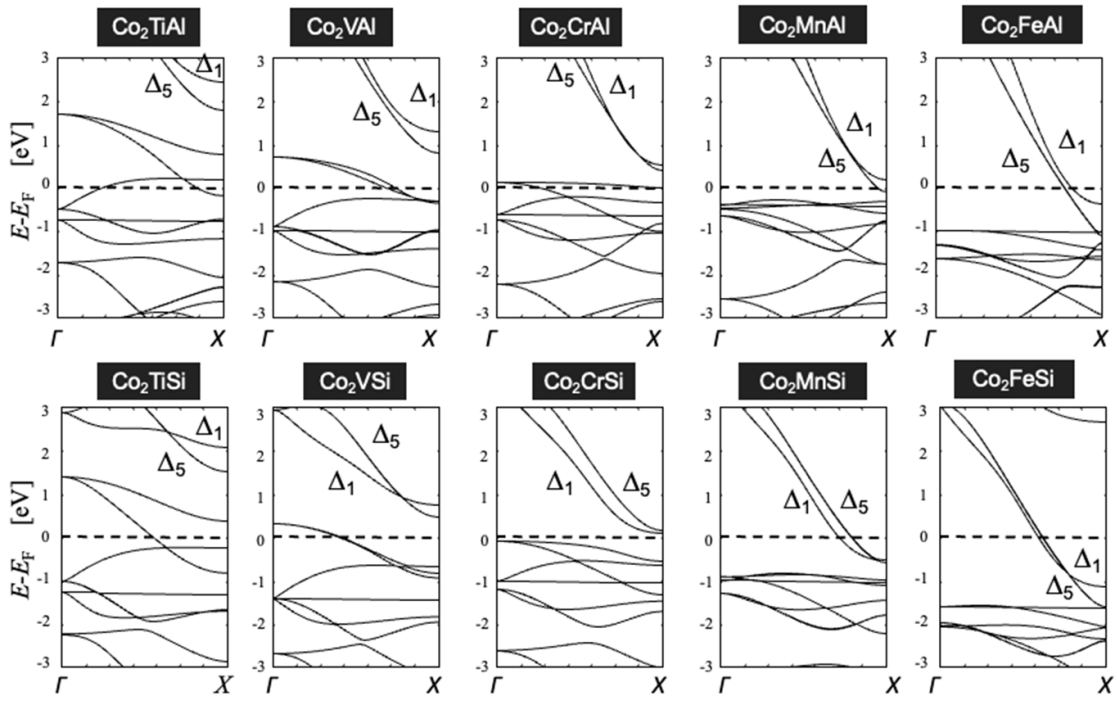


Figure 2. Majority-spin electronic band dispersion to [001]-direction in Co_2YZ (Y = Ti, V, Cr, Mn, Fe, Z = Al, Si) the coherent tunneling can be expected in Co_2MnAl, Co_2FeAl, Co_2MnSi, Co_2FeSi because of the presence of Δ_1 band at the Fermi level.

which Fe, Cr, and Al atoms are disordered [17] (figure 3). Based on these findings, Inomata *et al* fabricated MTJs using $Co_2Cr_{0.6}Fe_{0.4}Al$ electrodes combined with an Al–O tunnel barrier [26]. Even films deposited at RT without post-annealing exhibited a B2 structure, and TMR ratios of 16.5% at RT and 26.5% at 5 K were observed. Although detailed evaluations of the degree of atomic ordering were not conducted, the films deposited at RT are expected to retain a certain level of disorder among Co, Cr, and Fe atoms, which is presumed to be one of the factors limiting the achievable TMR ratio.

2.1.3. Co_2MnAl-based MTJ

The electronic structure of Co_2MnAl was first investigated by Kübler *et al* in 1982 through band-structure calculations [55]. Subsequently, Ishida *et al* explicitly stated that Co_2MnAl possesses an electronic structure close to half-metallicity based on the first-principles calculations [12]. Subsequently, Kubota *et al* fabricated MTJs using polycrystalline Co_2MnAl electrodes combined with amorphous Al–O tunnel barriers and reported a TMR ratio of 40% at RT [56]. A significant improvement was later achieved by Sakuraba *et al*, who developed a method to form an atomically flat Cr buffer layer on MgO substrates. By depositing Co_2MnAl on this Cr buffer layer, they realized much smoother epitaxial B2-ordered Co_2MnAl bottom electrode compared with conventional polycrystalline films [57]. Using this structure, MTJs with Al–O tunnel barriers were fabricated, resulting in a TMR ratio of 65% at RT [30] (figure 4), which exceeded that of devices employing CoFe bottom electrodes that were widely used at that time. The corresponding spin polarization was estimated to be 0.59, which is relatively high but still smaller than the theoretically predicted value of 0.76. This discrepancy is likely attributable to oxidation at the Co_2MnAl electrode surface during the plasma oxidation process used for the Al–O barrier formation. In particular, Mn and Al have a strong affinity for oxygen, making it difficult to fully suppress interfacial oxidation under conventional oxidation conditions.

As a side note, although Co_2MnAl was initially expected to be a half-metal, it was later experimentally reported to exhibit a remarkably large anomalous Hall effect [58]. Subsequent theoretical studies revealed that this behavior originates from the presence of Weyl points in the majority-spin electronic bands of Co_2MnAl [59]. Consequently, Co_2MnAl has attracted strong interest as a material with unconventional topological properties rather than as a simple half-metal. Notably, Co_2MnAl is currently recognized as the material exhibiting the largest experimentally observed anomalous Hall resistivity at RT among all known materials [60].

Table 1. Summary of the MTJs with half-metallic Heusler electrodes. The units of the numbers in parentheses within the "Stacking structure" are in nm.

Heusler alloy	Atomic order in Heusler layer	Substrate	poly/epi	Stacking structure	TMR ratio (RT)	TMR ratio (LT)	TMR(RT)/ TMR(LT)	Ref.
NiMnSb	$C1_b$	Si-SiO_2	poly	NiMnSb/Al-O/$Ni_{0.8}Fe_{0.2}$	2.40%	7.0% (77 K)	0.34	Tanaka *et al* [24]
	$C1_b$	InP	epi	NiMnSb/Al-O/CoFe	8.70%	14.7% (4.2 K)	0.59	Liu *et al* [25]
$Co_2Cr_{0.6}Fe_{0.4}Al$	B2	Si-SiO2	poly	CCFA(10)/ Al-O(3)/CoFe/IrMn	16%	26.5% (5 K)	0.60	Inomata *et al* [26]
	B2	Si-SiO2	poly	CCFA/MgO (3)/CoFe/IrMn	30%	56% (20 K)		Rata *et al* [27]
	B2	MgO(001)	epi	MgO-buffer/CCFA/ MgO(2)/CoFe	42%	74% (55 K)	0.57	Marukame *et al* [28]
Co_2MnAl	B2	Si-SiO2	poly	Cr/Co_2MnAl (20)/Al-O (2)/CoFe/IrMn	40%	65% (10 K)	0.62	Oogane *et al* [29]
	B2	MgO(001)	epi	Cr/Co_2MnAl (20)/Al-O (2)/CoFe/IrMn	65%	83% (10 K)	0.78	Sakuraba*et al* [30].
Co_2MnSi		Si-SiO_2	poly	V/Co_2MnSi(100)/Al-O/CoFe/IrMn	33%	86% (10 K)	0.38	Schmalhorst *et al* 2004, [31]
	$L2_1$	MgO(001)	epi	Cr/Co_2MnSi(30)/Al-O(1.3)/CoFe/IrMn	70%	159% (2 K)	0.44	Sakuraba*et al* [32]
	$L2_1$	MgO(001)	epi	Cr/Co_2MnSi (30)/Al-O (1.3)/Co_2MnSi(10)/IrMn	67%	570% (2 K)	0.12	Sakuraba*et al* [33]
	$L2_1$	Al_2O_3 substrate	epi	Ta/W/Cr/Co_2MnSi(30)/Al(1.3)-O/CoFe/IrMn	40%	120% (2 K)	0.33	Hattori *et al* [34]
	$L2_1$	MgO(001)	epi	Cr/Co_2MnSi(30)/MgO(2–2.5)/CoFe/IrMn	217%	753 K (2 K)	0.29	Tsunegi *et al* [35]
	$L2_1$	MgO(001)	epi	MgO/Co_2MnSi(30)/CoFeB(0.5)/ MgO(2.3)/CoFe/IrMn	222%	510% (10 K)	0.44	Tsunegi *et al* [36]
	$L2_1$	MgO(001)	epi	MgO/Co_2MnSi(30)/MgO (2.0–3.0)/Co_2MnSi(3–5)/Ru/CoFe/IrMn	236%	1135% (4.2 K)	0.21	Ishikawa *et al* [37]
	$L2_1$	MgO(001)	epi	MgO/CoFe/Co_2MnSi(3)/MgO(1.4–3.2)/Co_2MnSi(3)	330%	1995% (4.2 K)	0.17	Liu *et al* [38]

(Continued.)

Table 1. (Continued.)

$Co_2(Mn,Fe)Si$	$L2_1$	MgO (001)	epi	$Cr/Co_2Fe_{0.4}Mn_{0.6}Si(30)/Al(1.3)$-O/CoFe/IrMn/	75%			Kubota *et al* [39]
	$L2_1$	MgO(001)	epi	MgO/CoFe/CMFS(3)/MgO(1.4–3.2)/CMFS(3)/CoFe/IrMn	429%	2610% (4.2 K)	0.16	Liu *et al* [40, 41]
Co_2MnGe	$L2_1$	MgO(001)	epi	$Co_2MnGe/MgO/Co_{50}Fe_{50}$	14%	70% (7 K)	0.20	Marukame *et al* [42]
	$L2_1$	Al_2O_3 substrate	epi	Co_2MnGe/Al_2O_3 /Co	9%	27% (77 K)	0.33	Verdui [43]
	$L2_1$	MgO (001)	epi	MgO/Co_2MnGe(50)/MgO(2–3)/CoFe/Ru/CoFe/IrMn	160%	376% (4.2 K)	0.43	Taira *et al* [44]
	$L2_1$	MgO (001)	epi	MgO/Co_2MnGe(30)/MgO(2–3)/Co_2MnGe(10)/Ru/CoFe/IrMn	220%	650% (4.2 K)	0.34	Yamamoto *et al* [45]
Co_2FeAl	B2	MgO(001)	epi	MgO/Cr/CFA(30)/MgO(1.8)/CFA(5)/IrMn	360%	785% (10 K)	0.46	Wang *et al* [46]
	B2	MgO (001)	epi	Cr/CoFe/Co_2FeAl(5)/CoFe(0.5)/Mg(0.45)Mg19Al81(0.75)-O/Co_2FeAl(5)/CoFe/IrMn	342%	616% (4 K)	0.56	Scheike *et al* [47]
Co_2FeSi	$L2_1$	MgO (001)	epi	MgO/Cr/Co_2FeSi/MgO(2)/CoFe(5)/MnFe	117%	165% (15 K)	0.71	Sterwerf *et al* [48]
	$L2_1$	MgO (001)	epi	Cr/Co_2FeSi/Al(1.3)-O/CoFe/IrMn	48%	80% (2 K)	0.60	Oogane *et al* [49]
$Co_2FeAl_{0.5}Si_{0.5}$	$L2_1$	MgO(001)	epi	Cr/CFAS(30)/MgO/CFAS(5)/CoFe/IrMn	220%	390% (5 K)	0.56	Tezuka *et al* [50]
	B2	MgO(001)	epi	Cr/CFAS(80)/($MgAl_2$)Ox/CoFe/IrMn	102%	162% (26 K)	0.63	Shan *et al* [51]
Fe_2CoSi	$L2_1$	MgO (001)	epi	MgO/Cr/Fe_2CoSi/MgO(2)/CoFe(5)/MnFe	159%	262% (15 K)	0.61	Sterwerf *et al* [48]

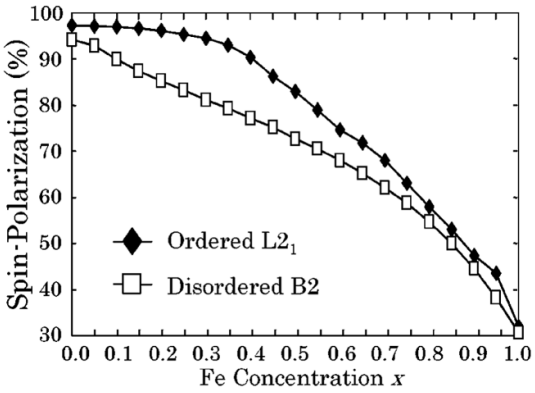


Figure 3. Fe concentration dependence of spin-polarization in $L2_1$-ordered and B2 disordered $Co_2(Cr_{1-x}Fe_x)Al$ calculated theoretically, Copyright (2004) by the American Physical Society. Reprinted (figure) with permission from [17], Copyright (2004) by the American Physical Society.

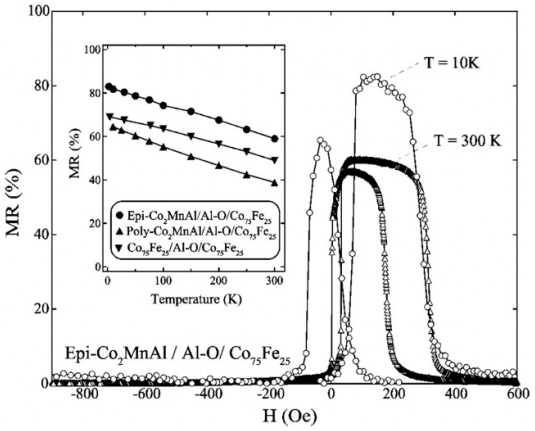


Figure 4. TMR curves for epitaxial Co_2MnAl/Al-O/CoFe. Reprinted from [30], with the permission of AIP Publishing. Inset shows the temperature dependence of TMR ratio.

2.1.4. Co_2MnSi-based MTJ

Co_2MnSi is widely regarded as the most representative half-metallic Heusler alloy to date, and its half-metallicity was theoretically predicted by Ishida *et al* [12] This compound exhibits a high Curie temperature of 985 K, and theoretical studies have shown that the half-metallic gap is preserved even in the B2-type disordered structure, where Mn and Si atoms are partially randomized [16]. These characteristics provide a significant advantage from practical application perspectives. Kämmerer *et al* were the first to fabricate MTJs using polycrystalline Co_2MnSi electrodes combined with amorphous Al–O tunnel barriers, reporting TMR ratios of 33% at RT and as high as 86% at 10 K [61]. Considering the characteristics of Co_2MnSi confirmed by the following studies, i.e. large temperature dependence of TMR ratio, the large TMR ratio observed at low temperature (LT) can be regarded as an early experimental indication of the half-metallic nature of Co_2MnSi. Subsequently, Sakuraba *et al* succeeded in fabricating Co_2MnSi electrodes with atomically flat surfaces and a high degree of $L2_1$ ordering by employing MgO substrates and Cr buffer layers. In MTJs using CoFe as the top electrode, TMR ratios of 70% at RT and 159% at 2 K were achieved [32]. Furthermore, when Co_2MnSi was used as both the bottom and top electrodes, even larger TMR ratios of 67% at RT and 570% at 2 K were observed [33] (figure 5). When converted into spin polarization values using the Jullière model, the TMR ratio at 2 K corresponds to an exceptionally high spin polarization of 0.89. As the TMR ratio was obtained through incoherent tunneling with conventional Al–O amorphous tunnel barrier, these results provide clear experimental evidence that Co_2MnSi possesses half-metallic characteristics.

Subsequently, numerous studies reported MTJs combining single-crystalline Co_2MnSi electrodes with MgO tunnel barriers [38]. In fully epitaxial (001)-oriented Co_2MnSi/MgO/Co_2MnSi junctions, giant TMR ratios as high as 330% at RT and 1995% at LTs were observed [38] (figure 6). Such extraordinarily large TMR ratios were concluded to originate from the synergistic contribution of Δ_1 -band-selective

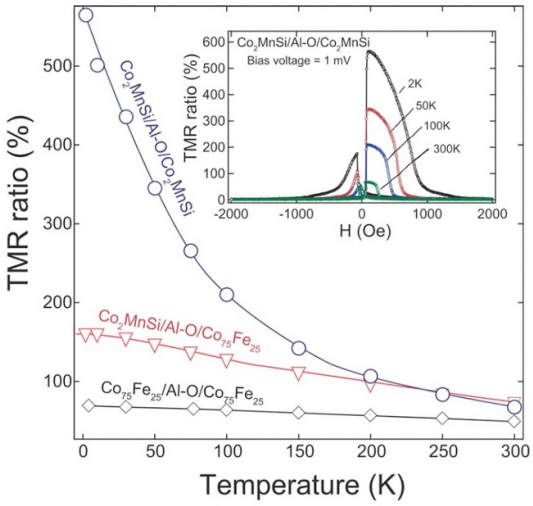


Figure 5. Temperature dependence of TMR ratio for Co_2MnSi/Al-O/Co_2MnSi-MTJ. Reprinted from [33], with the permission of AIP Publishing.

coherent tunneling through the MgO barrier and the half-metallic nature of Co_2MnSi as indicated by the theoretical calculation (figure 2). It is particularly important to note that these giant TMR ratios were not achieved in stoichiometric Co_2MnSi, but rather in intentionally Mn-rich compositions, such as $Co_2Mn_{1.35}Si_{0.88}$ (figure 6). In Co_2MnSi, theoretical studies had predicted that Co–Mn disorder and Co antisite defects severely degrade the half-metallic character [16]. In this context, Hülsen *et al* predicted that increasing the Mn content beyond the stoichiometric composition can suppress Co antisite formation from a thermodynamic viewpoint while simultaneously preserving half-metallicity from an electronic-structure perspective [62]. These findings convey an important general message: although many materials are theoretically predicted to exhibit half-metallic electronic structures, the robustness of half-metallicity against atomic disorder and off-stoichiometry is a crucial factor. The results for Co_2MnSi clearly demonstrate that, in practical materials design, achieving ideal stoichiometry is not necessarily optimal, and deliberate deviation from stoichiometry can be essential for realizing the intrinsic half-metallic properties.

First-principles calculations incorporating the on-site Coulomb interaction U demonstrated that partial substitution of Mn with Fe in Co_2MnSi shifts the Fermi level toward the center of the minority-spin gap, while maintaining a high degree of $L2_1$ ordering over a wide range of Mn:Fe composition ratios [63]. Motivated by these theoretical predictions, Kubota *et al* fabricated MTJs using single-crystalline Co_2(Mn,Fe)Si (CMFS) electrodes combined with amorphous Al–O tunnel barriers and systematically varied the Mn:Fe ratio. As a result, they achieved a maximum TMR ratio of 75% at RT for a composition with approximately 60% Fe, exceeding those of Co_2MnSi (67%) and Co_2FeSi (46%) [39] (figure 7(a)). The enhancement of the TMR ratio at this composition was further supported by the composition dependence of the magnetic damping constant, which is considered to be proportional to the total density of states at the Fermi level (figure 7(b)). This observation indicates that the spin polarization is maximized at this specific Mn:Fe ratio.

Furthermore, Liu *et al* reported MTJs employing CMFS electrodes and MgO tunnel barriers, in which all four elemental compositions were precisely tuned for optimization. They observed exceptionally large TMR ratios of 429% at RT and 2610% at LTs for a non-stoichiometric composition of $Co_2Mn_{1.24}Fe_{0.16}Si_{0.84}$ [40, 41] (figure 8). The enhancement of the TMR ratio in this case was attributed to the suppression of Co antisite defects by adjusting the total Mn + Fe content to approximately 1.40. The low-temperature TMR ratio of 2610% represents the highest value reported to date and far exceeds those of conventional MgO-based MTJs employing CoFeB or CoFe electrodes, which exhibit maximum RT TMR ratios of 1144% [64] and 1143% [65], respectively. This remarkable enhancement can be reasonably attributed to the half-metallic nature of CMFS.

Thus, MTJs based on Co_2MnSi and Co_2(Mn,Fe)Si with both Al-O amorphous barrier and MgO crystalline barrier exhibit extraordinarily large TMR ratios at LTs, which clearly arises from half-metallic nature. However, the TMR ratio decreases rapidly with increasing temperature, and to date, no RT-TMR values surpassing those of CoFe/MgO-based systems have been reported. The origin of this pronounced temperature dependence will be discussed in section 2.2.

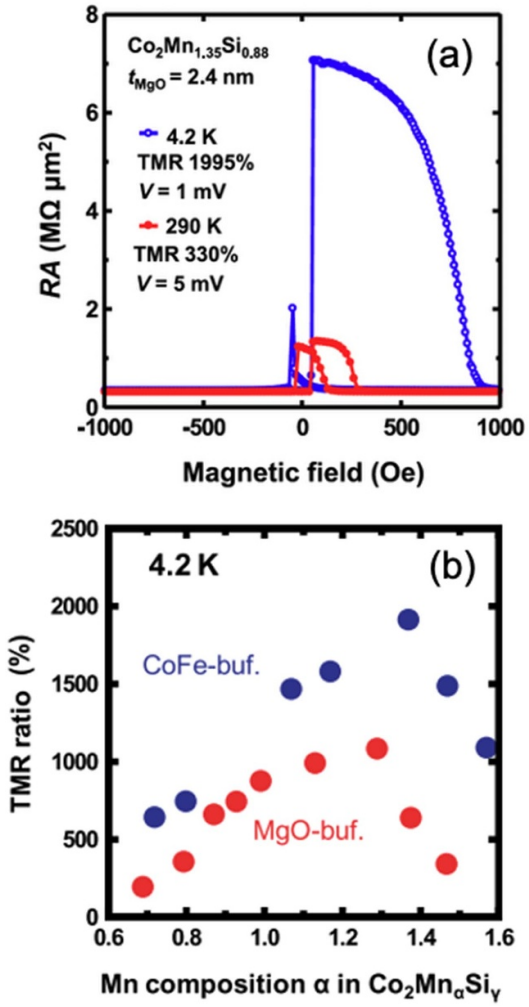


Figure 6. (a) TMR curves for $Co_2Mn_{1.35}Si_{0.88}$ /MgO/ $Co_2Mn_{1.35}Si_{0.88}$ MTJ. (b) Mn composition dependence of TMR ratio at 4.2 K in $Co_2Mn_\alpha Si_\gamma$/MgO/ $Co_2Mn_\alpha Si_\gamma$ grown CoFe-buffer and MgO buffer layers. Reprinted from [38], with the permission of AIP Publishing.

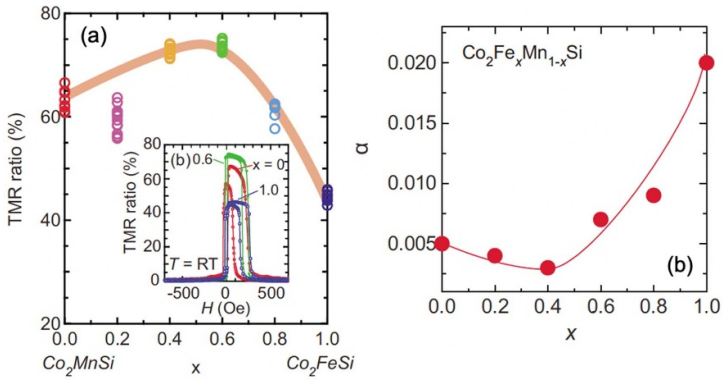


Figure 7. (a) Fe composition x dependence of TMR ratio at RT in the CMFS/Al-O/CoFe MTJs and (b) damping constant in the CMFS films. Reprinted from [39], with the permission of AIP Publishing.

2.1.5. Co_2MnGe-based MTJ

Co_2MnGe, in which Ge with the same valence electron number as Si occupies the Z site, is also a representative Heusler alloy that has been theoretically predicted to exhibit half-metallicity. This compound possesses a high Curie temperature of about 900 K. As summarized in Table 2, Co_2MnGe has a lower melting point than Co_2MnSi, resulting in higher motive force to form $L2_1$ ordered structure. Consequently, a high degree of $L2_1$ ordering can be more readily achieved even in thin films

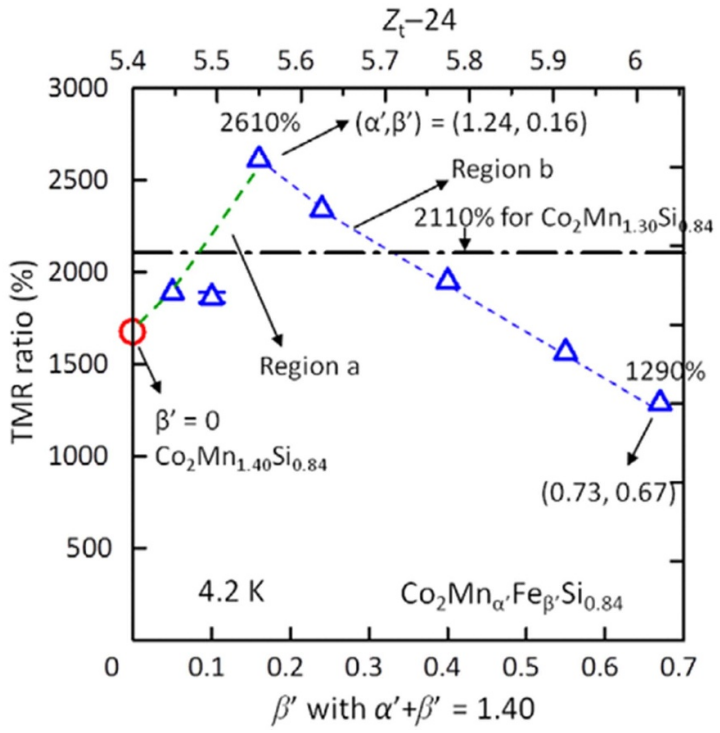


Figure 8. TMR ratio at 4.2 K as a function of β' in the $Co_2Mn_{\alpha'}Fe_{\beta'}Si$/MgO/$Co_2Mn_{\alpha'}Fe_{\beta'}Si$ MTJs. Reproduced from [40]. © IOP Publishing Ltd All rights reserved.

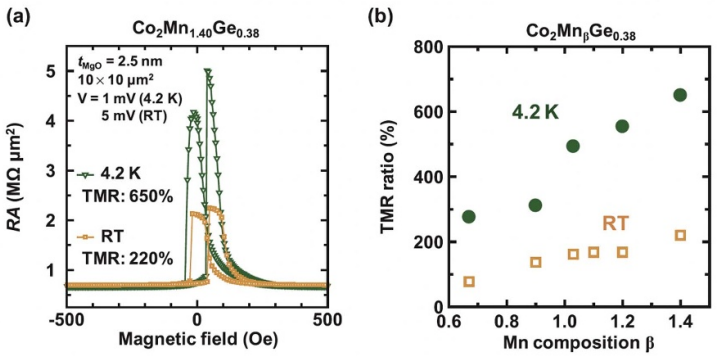


Figure 9. (a) TMR curves at 4.2 K and RT for the MTJ with $Co_2Mn_{1.40}Ge_{0.38}$ electrode. TMR ratio at 4.2 K as a function of β in the $Co_2Mn_\beta Ge_{0.38}$/MgO/$Co_2Mn_\beta Ge_{0.38}$. Reproduced from [45]. © IOP Publishing Ltd All rights reserved.

through relatively low-temperature post-annealing, which constitutes a practical advantage for device fabrication [66, 67]. Yamamoto *et al* fabricated $Co_2Mn_bGe_{0.38}$/MgO/ $Co_2Mn_bGe_{0.38}$ MTJs using Mn off-stoichiometric electrodes and systematically investigated the composition dependence of the TMR ratio. They successfully observed a maximum TMR ratio of 220% at RT and as high as 650% at 4.2 K for the most Mn-rich composition with $\beta = 1.40$ [45] (figure 9). Similar to the case of Co_2MnSi, the enhancement of the TMR ratio with increasing Mn content was attributed to the suppression of Co antisite defects. Although the TMR ratios of Co_2MnGe/MgO MTJs are smaller than those reported for Co_2MnSi/MgO MTJs, the underlying reason for this difference has not yet been fully clarified. It should be noted, however, that in the experiments by Yamamoto *et al* [45], the Ge concentration was approximately 10 at.%, which is significantly lower than the stoichiometric value of 25 at.%. Therefore, further optimization of the chemical composition, including the Ge content, may enable the realization of larger TMR ratios in Co_2MnGe -based MTJs.

2.1.6. Co_2FeAl and Co_2FeSi MTJ

Co_2FeAl is a material that has been theoretically predicted to exhibit a pseudogap-like structure in the minority-spin band, even when it crystallizes in either the $L2_1$ or B2 structure [17]. As summarized in

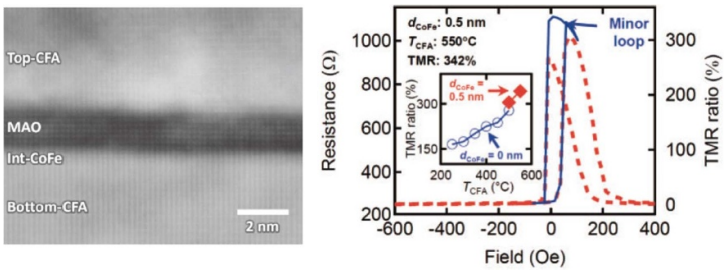


Figure 10. Cross-sectional scanning transmission electron microscopy image and TMR curves of the MTJ with $Co_2FeAl/CoFe/MgAl_2O_4/Co_2FeAl$ MTJ. Reproduced from [47]. © 2016 The Japan Society of Applied Physics.

Table 2 in section 3.2.1, Co_2FeAl has a high melting point and a low order–disorder transition temperature, which makes it extremely difficult to realize a fully $L2_1$-ordered structure in thin films. Because the minority-spin band does not possess a complete gap, the spin polarization does not reach 100%. Nevertheless, as shown in figure 2, the electronic band structure reveals that along the Γ–X direction the Δ_1 band exists in the majority-spin channel at Fermi level. Consequently, when combined with an MgO tunnel barrier, coherent tunneling mediated by Δ_1 symmetry filtering is expected to yield a large TMR ratio. Wang *et al* reported giant TMR ratios of 360% at RT and 785% at 10 K in fully epitaxial $Co_2FeAl/MgO/Co_2FeAl$ MTJs employing single-crystalline Co_2FeAl electrodes [46]. In addition, Scheike *et al* successfully fabricated fully epitaxial MTJs using a $MgAl_2O_4$ spinel tunnel barrier, which exhibits an extremely small lattice mismatch with Co_2FeAl, and reported TMR ratios of 342% at RT and 616% at LT [47] (figure 10). It has been reported that when the thickness of the Co_2FeAl electrode is reduced to approximately 1 nm, perpendicular magnetic anisotropy (PMA) emerges at the Co_2FeAl/MgO tunnel-barrier interface, resulting in the formation of pMTJs. Using such a structure, a TMR ratio of 91% at RT under a perpendicular magnetic field was achieved [69]. However, subsequent microstructural analyses revealed that Al atoms from the ultrathin Co_2FeAl layer diffuse into the MgO barrier. This interdiffusion was suggested to be the origin of the observed interfacial PMA rather than an intrinsic property of the Co_2FeAl/MgO interface [70].

Co_2FeSi is a material whose half-metallic character has been extensively debated both theoretically and experimentally. In first-principles calculations that do not include on-site Coulomb interactions (U), the Fermi level of Co_2FeSi lies close to or crosses the conduction band edge of the minority-spin half-metallic gap [71]. Consequently, the calculated magnetic moment deviates from an integer value in units of the Bohr magneton [52], leading to the conclusion that Co_2FeSi is not a half-metal. In contrast, experimental measurements yield an integer magnetic moment of 6 μ_B per formula unit, which motivated the introduction of on-site Coulomb interactions in theoretical calculations. When U is included, Co_2FeSi has been claimed to exhibit half-metallic behavior [71]. However, since U is treated as an empirical free parameter, there is no clear consensus regarding either the appropriate magnitude of U or the specific atomic sites to which U should be applied.

From an experimental perspective, analyses of the temperature dependence of electrical resistivity and magnetoresistance (MR) in bulk single-crystalline Co_2FeSi indicated that the energy separation between the Fermi level and the valence-band edge is extremely small, 8.9 meV [72]. Similarly, Sakuraba *et al* analyzed the valence band electron number and temperature dependences of the anisotropic MR (AMR) effect and concluded that the Fermi level in Co_2FeSi is located very close to the conduction-band edge, implying that half-metallicity, if present, is realized only at LTs [73] (figure 11(a)). More recently, Sumida *et al* investigated the partial density of states of Fe using resonant photoemission spectroscopy (PES) and concluded that introducing U at the Fe site in first-principles calculations exaggerates discrepancies with experimentally observed spectra, suggesting that a U correction at the Fe site is unnecessary [74]. In contrast, Zhou *et al* analyzed the temperature dependence of the anomalous Hall and Nernst effects in single-crystalline Co_2FeSi thin films and found that calculations without U are entirely inconsistent with experimental results, leading them to conclude that a moderate U of approximately 1–2 eV applied to the Co site is reasonable [75] (figure 11(b)). Taking these results together, it was concluded that while a U correction is likely required to accurately describe the electronic density of states in Co_2FeSi, the Fermi level is situated very close to the conduction-band edge, rendering Co_2FeSi an unstable half-metal at RT.

Experimental reports on MTJs employing Co_2FeSi electrodes remain limited. Sterwerf *et al* reported TMR ratios of 117% at RT and 165% at LT in MTJs using single-crystalline Co_2FeSi electrodes

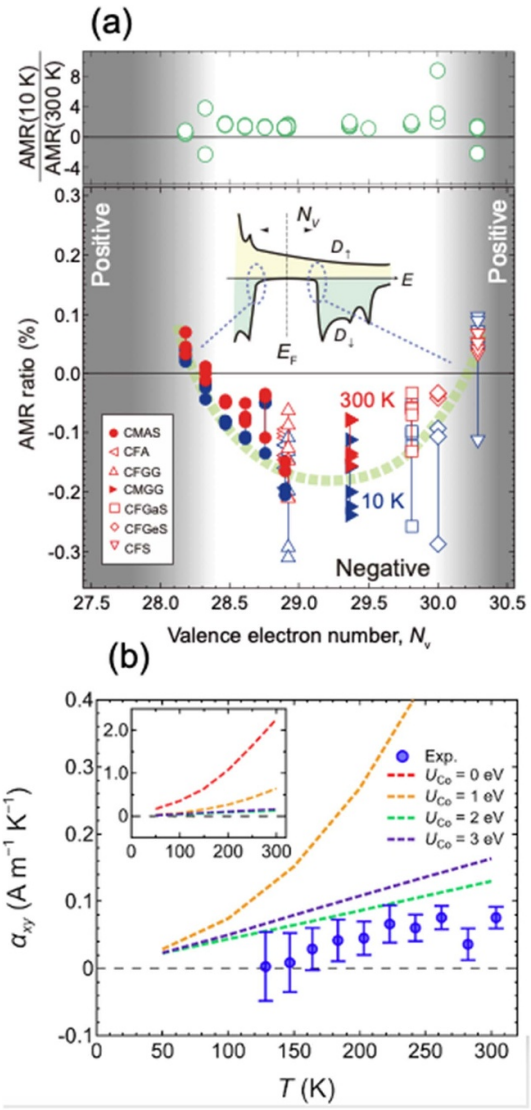


Figure 11. (a) Valence electron number dependence of AMR at 10 K and 300 K in various Co-based Heusler alloy thin films. Here CFS stands for Co_2FeSi. Negative AMR, suggesting a half-metallic nature, appears only at 10 K for Co_2FeSi. Reprinted from [73], with the permission of AIP Publishing. (b) Temperature dependence of anomalous Nernst conductivity in Co_2FeSi thin film and the comparison with the theoretical calculations with adding U on Co-site [75].

combined with MgO tunnel barriers [48]. Compared with MTJs based on Co_2MnSi or Co_2MnGe, MTJs employing Co_2FeAl and Co_2FeSi exhibit a weaker temperature dependence of the TMR ratio. However, because their low TMR ratios at LT are comparable to those of MTJs using conventional CoFe electrodes, it is reasonable to conclude that coherent tunneling through the MgO barrier, rather than intrinsic half-metallicity, plays the dominant role for large TMR ratios in these systems.

Quaternary Heusler alloys of the $Co_2Fe(Si,Al)$ system enable rigid-band–like tuning of the Fermi level by mixing trivalent Al and tetravalent Si, shifting the Fermi level toward the center of the half-metallic gap, as theoretically demonstrated [76]. As discussed above, although it is difficult to realize highly $L2_1$-ordered thin films of Co_2FeAl, partial substitution of Al with Si facilitates $L2_1$ ordering, which represents a significant advantage for practical device applications [77]. Shan *et al* reported MTJs employing single-crystalline $Co_2FeAl_{0.5}Si_{0.5}$ electrodes, achieving TMR ratios of 102% at RT and 162% at LT, which were among the largest values reported at the time [51]. Based on analyses of the temperature dependence of the tunnel conductance, they estimated the spin polarization of $Co_2FeAl_{0.5}Si_{0.5}$ to be as high as 0.91 at 300 K and claimed that half-metallicity persists even at RT. However, because the $(MgAl)O_x$ tunnel barrier employed in their study was clearly crystalline, the possibility that coherent tunneling enhanced the effective spin polarization of the CoFe top electrode leading to the overestimation of the spin-polarization of $Co_2FeAl_{0.5}Si_{0.5}$ cannot be entirely excluded. Actually, this study motivated subsequent reports by the same group, in which large TMR ratios were observed using spinel-type $MgAl_2O_4$ tunnel barriers that promote coherent tunneling [47].

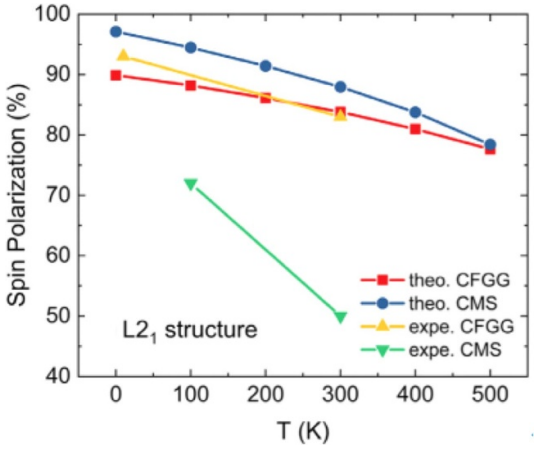


Figure 12. Temperature dependence of spin-polarization for CFGG and CMS theoretically calculated by DLM method. Experimentally evaluated bulk spin-polarization is also plotted for comparison. Reprinted from [81], Copyright (2021), with permission from Elsevier.

2.2. Mechanism of large temperature dependence of TMR ratio in Heusler-based MTJ

As described above, MTJs employing half-metallic Heusler alloys, particularly those based on Co_2MnSi and $Co_2(Fe,Mn)Si$, exhibit extremely large TMR ratios at cryogenic temperatures that directly reflect their half-metallic nature. However, despite high Curie temperatures of about 1000 K, these devices show a remarkably strong temperature dependence of the TMR ratio, which decreases to only 10%–30% of its low-temperature value at RT (see TMR(RT)/TMR(LT) in Table 1). Owing to this pronounced temperature dependence, the RT-TMR ratios of Heusler-alloy-based MTJs are inferior to those of conventional CoFeB/MgO/CoFeB junctions [64]. This limitation has been one of the primary reasons why MTJs using Heusler alloys have not become the mainstream approach for practical applications such as HDD read heads and MRAM.

Two possible origins of this strong temperature dependence can be considered. One is an intrinsic reduction of spin polarization in the bulk regions of Co_2MnSi and $Co_2(Fe,Mn)Si$ with increasing temperature. The other is the emergence of interfacial issues at the tunnel barrier interfaces, such as those involving Al–O or MgO barriers, which may degrade the effective spin polarization contributing to tunneling. In this section, we review previous studies relevant to the origin of this temperature dependence and discuss possible strategies for mitigating this issue.

2.2.1. Temperature dependence of bulk spin-polarization in half-metallic Heusler alloys

The temperature dependence of spin polarization in the bulk regions of half-metallic Heusler alloys has been extensively investigated by first-principles calculations. Chioncel *et al* employed dynamical mean-field theory (DMFT) to demonstrate that non-quasiparticle states originating from virtual magnons, which arise from the coupling between minority-spin states and majority-spin electron bands, emerge just above the half-metallic gap in NiMnSb [78] and Co_2MnSi [79]. They predicted that these states could significantly reduce the bulk spin polarization at finite temperatures. However, the DOS obtained from these calculations differs substantially from the bulk DOS of Co_2MnSi observed experimentally by hard x-ray PES, (HAXPES) suggesting that further verification of this theoretical approach is required [80] Kurniawan *et al* incorporated finite-temperature effects into first-principles calculations using the disordered local-moment (DLM) method and evaluated the temperature dependence of bulk spin polarization in Co_2MnSi and $Co_2FeGa_{0.5}Ge_{0.5}$(CFGG) [81]. As shown in figure 12, their results indicate that the temperature dependence of the bulk spin polarization is much weaker than that inferred from the temperature dependence of the TMR ratio, and is predominantly governed by factors such as the Curie temperature and the position of the Fermi level within the half-metallic gap.

PES is one of the most widely used techniques for evaluating the spin polarization of magnetic materials. However, the escape depth of photoelectrons strongly depends on the photon energy [82]. In the vacuum ultraviolet (VUV) and UV regimes, PES is extremely surface sensitive, whereas soft x-ray excitation provides bulk sensitivity on the order of a few nanometers, and HAXPES enables probing depths exceeding several tens of nanometers. Jourdan *et al* reported a spin polarization of approximately 0.93 at RT using surface-sensitive spin-resolved (SR) UV PES [83]. To overcome the intrinsic difficulty of SR

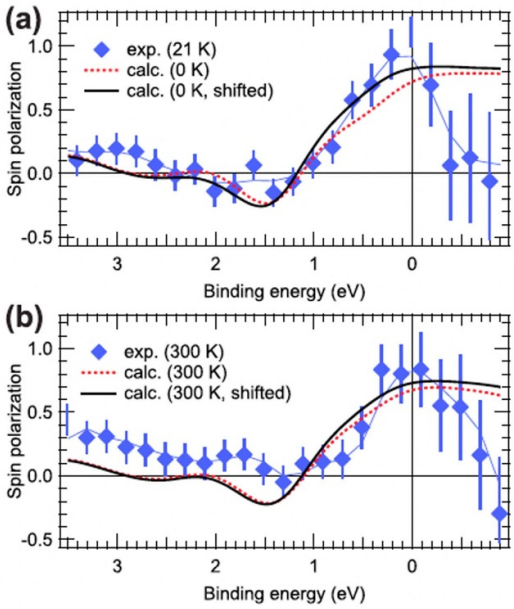


Figure 13. Binding energy dependence of spin-polarization at 21 K and 300 K for Co_2MnSi epitaxial thin film measured by SR-HAXPES. Reproduced from [85]. CC BY 4.0.

measurements in HAXPES due to the small photoionization cross section, Ueda *et al* developed a dedicated sample holder that integrates an Au thin film serving as a Mott detector together with the sample, and realized SR-HAXPES using a two-dimensional photoelectron detector [84]. Using this technique, they measured the temperature dependence of the bulk spin polarization in single-crystalline Co_2MnSi thin films and observed a spin polarization of approximately 0.9 at 21 K. Moreover, they demonstrated that the half-metallic character remains nearly unchanged up to 300 K (figure 13) [85].

In addition, Ikhtiar *et al* analyzed the temperature dependence of the bulk spin polarization of CFGG in nonlocal spin-valve (SV) devices using CFGG spin-injector and detector and a Cu channel. By applying a one-dimensional spin-diffusion model for the transparent interface condition, they determined that the bulk spin polarization remains high, with values of 0.93 at 10 K and 0.83 at RT, indicating only a weak temperature dependence and confirming that robust half-metallic behavior persists even at RT [86] (figure 14).

Although indirect, AMR measurements can also provide valuable information about the temperature dependence of half-metallic nature in the bulk region. Kushwaha *et al* demonstrated that the temperature dependence of the AMR-induced resistance change is strongly governed by the electronic structure near the Fermi level, and that when the Fermi energy E_F is located close to the center of the half-metallic gap, the temperature dependence of the resistance change becomes extremely small [87]. From these results, it is suggested that half-metallicity is preserved up to RT in CFGG thin films with a high degree of atomic ordering and without Co antisite defects.

Based on these theoretical and experimental findings, it is reasonable to conclude that the pronounced temperature dependence of the TMR ratio observed in MTJs using Heusler alloys is unlikely to be dominantly caused by a degradation of the spin polarization in the bulk region of the electrode material although there should be a certain level of the contribution from the bulk region due to the position of Fermi level in half-metallic gap.

2.2.2. Temperature dependence of interface spin-polarization in half-metallic Heusler alloys

In MTJs employing Heusler alloys, the TMR ratio exhibits not only a strong temperature dependence but also a pronounced bias-voltage dependence. In Co_2MnSi/Al–O/Co_2MnSi MTJs, where an exceptionally large TMR ratio of 570% was first observed at LT, the TMR ratio is reduced by half at a bias voltage as small as 60 mV [33]. This characteristic voltage scale is nearly one order of magnitude smaller than that typically observed in MTJs using conventional electrodes such as CoFe. Initially, this strong bias dependence was attributed to the position of the Fermi level in Co_2MnSi, which was presumed to lie close to the valence-band edge of the half-metallic gap [88]. However, subsequent studies demonstrated that even in $Co_2MnAl_xSi_{1-x}$ (CMAS)/Al–O/CoFe MTJs—where the Fermi level is shifted downward by substituting Si with Al—the bias dependence of the TMR ratio remains essentially unchanged, regardless

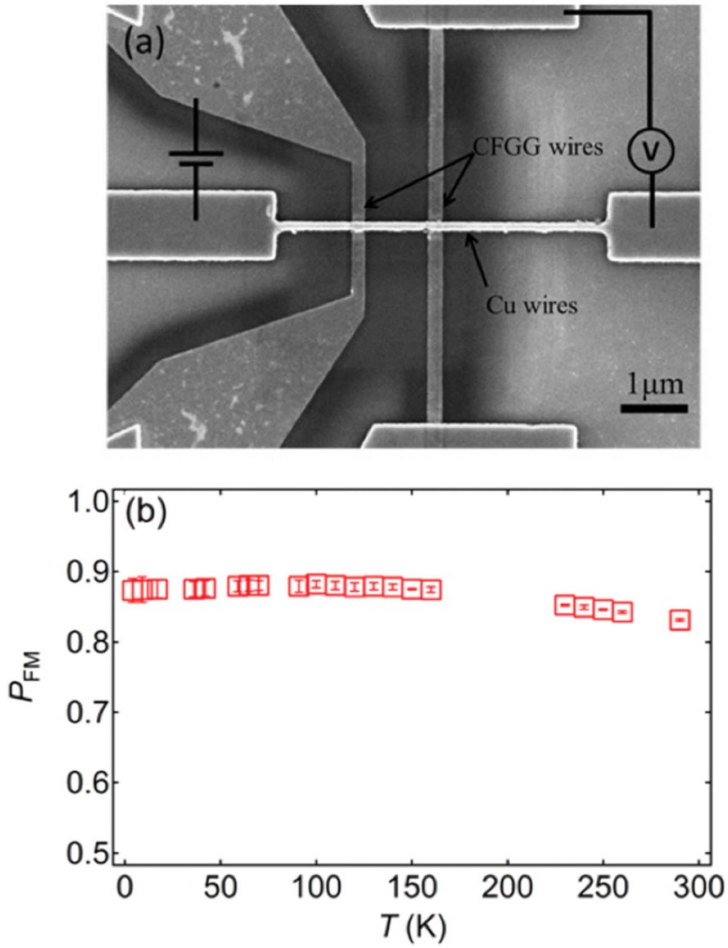


Figure 14. (a) Scanning electron microscopy image of the NLSV device made with CFGG wires and Cu channel wire. (b) Temperature dependence of bulk spin-polarization of CFGG evaluated from the spin-accumulation signal in NLSV. Reprinted from [86], with the permission of AIP Publishing.

of the Al concentration [89]. As shown in figure 15(a), when the bias polarity is the direction of that tunneling electrons flow from the CMAS electrode to the CoFe electrode, a clear shift of the valence-band edge of the half-metallic gap is experimentally observed. In contrast, when electrons tunnel from the CoFe electrode into the CMAS electrode, the tunneling conductance always increases at low bias, and the conduction band appears to be effectively pinned just above the Fermi level. As illustrated in figure 15(b), these observations have been explained in terms of tunneling via interface states formed within the half-metallic gap, combined with inelastic tunneling processes involving spin-flip scattering mediated by interface magnon excitations [90]. Sakuma *et al* predicted from first-principles calculations that, in Co_2MnAl/MgO and Co_2MnSi/MgO junctions, the magnetic moment and exchange energy of Co atoms at the interface termination layer are significantly reduced compared with those in the bulk [91]. (figure 16) This implies a substantial lowering of the magnon excitation energy at the interface, which naturally enhances inelastic tunneling processes accompanied by spin flips, in good agreement with experimental interpretations. Furthermore, a local reduction of the Curie temperature near the barrier interface is also expected, providing a consistent explanation for the strong temperature dependence of the TMR ratio. Miura *et al* further calculated the reduction in the TMR ratio caused by noncollinear tilting of magnetic moments in the interfacial termination layer of Co_2MnSi/MgO and predicted a significant impact of such interfacial magnetic disorder [92].

These interfacial magnetic effects have also been experimentally verified. Tsunegi *et al* employed depth-resolved XMCD to element-selectively measure the Co magnetic moments in the bulk and interfacial regions of Co_2MnSi [93]. In the reference CoFe/MgO system, the Co magnetic moments at the bulk and in the interface were 2.30 μ_B and 1.90 μ_B, respectively, indicating that approximately 80% of the bulk moment is retained at the interface. In contrast, for Co_2MnSi/MgO, the corresponding moments were much smaller—1.06 μ_B at the interface and 0.60 μ_B in the bulk—revealing that the interfacial magnetic moment is reduced to about 60% of the bulk value. Because the exchange stiffness energy is

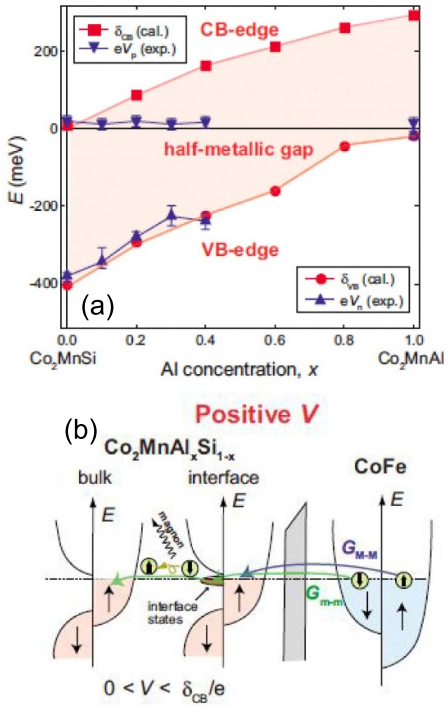


Figure 15. (a) Bias voltages where the tunneling conductance rapidly increase in CMAS/Al-O/CoFe(eV_p and eV_m) and the theoretically calculated edges of conduction band and valence band of half-metallic gap (and δ_{VB}) as a function of Al concentration x. (b)In elastic tunneling process in parallel configuration from CoFe to CMAS electrodes through the interface states and magnon excitations. Reprinted (figure) with permission from [89], Copyright (2010) by the American Physical Society.

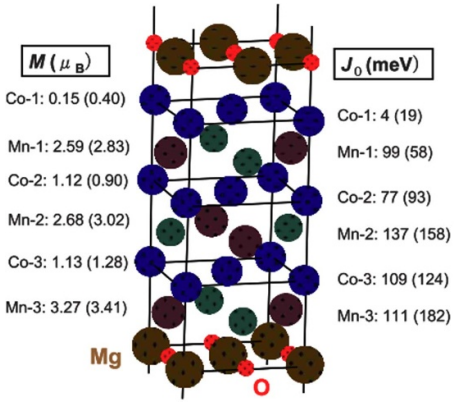


Figure 16. Magnetic moments and the exchange constants of each atom in the $Co_2MnAl(Si)$ /MgO structure calculated by the first principles calculations. The values in the parentheses are for Co_2MnSi/MgO. Co-1 and Mn-3 indicate two interfacial layers with MgO. Reprinted from [91], with the permission of AIP Publishing.

proportional to the square of the magnetic moment, such a pronounced reduction in the interfacial magnetic moment provides a natural explanation for the experimentally observed strong temperature and bias-voltage dependences of the TMR ratio in Heusler-alloy-based MTJs.

2.2.3. Potential solutions to obtain larger TMR ratio in half-metallic Heusler alloy-based MTJs at RT

Based on the mechanisms discussed above for the pronounced temperature dependence of the TMR ratio, we now outline possible guidelines for realizing a large TMR ratio originating from half-metallicity even at RT—ideally exceeding that of conventional CoFeB/MgO-based MTJs. First, regarding the bulk electronic structure of half-metallic Heusler alloys, it has been demonstrated that Co_2MnSi can retain a high spin polarization even at RT [83, 85]. In contrast, Co_2FeSi exhibits a significant degradation of half-metallicity from LT to RT, even in the bulk state [73]. This comparison indicates that tuning the Fermi level as close as possible to the center of the half-metallic gap is a necessary condition. However, since

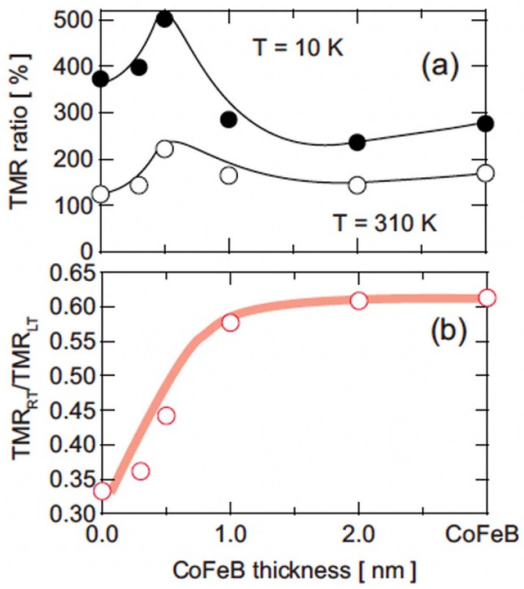


Figure 17. (a) Inserted CoFeB thickness dependence of TMR ratios at 310 K and 10 K and (b) the ratio of TMR at 310 K to that at 10 K in Co_2MnSi/CoFeB/MgO/CoFe-MTJ. Reprinted from [36], with the permission of AIP Publishing.

interfacial effects at the tunnel barrier are dominant, this condition alone is clearly insufficient to achieve a giant RT TMR ratio.

The key to realizing large TMR ratios at RT lies, therefore, in two interfacial factors: (i) enhancement of the magnetic stiffness at the tunnel barrier interface and (ii) suppression of in-gap states within the half-metallic gap. To enhance the interfacial magnetic stiffness, atomic-scale control of the termination layers at the tunnel barrier interface is expected to be effective. Tsunegi *et al* demonstrated that inserting a 0.5-nm-thick CoFeB layer at the Co_2MnSi/MgO interface increases the RT TMR ratio by approximately a factor of two, while simultaneously reducing its temperature dependence [36] (figure 17). As high magnetic stiffness of the FeCo/MgO interface has also been confirmed by XMCD [93] and related measurements, these results strongly suggest that inserting one or two atomic layers of Fe–Co-based materials at the interface is an effective strategy for enhancing magnetic stiffness. Nevertheless, whether such an approach is fully compatible with maintaining the half-metallic gap at the interface remains an open question and requires careful verification, including first-principles calculations.

A second, and equally important, strategy for improving the temperature dependence of the TMR ratio is the suppression of interfacial states within the half-metallic gap. As illustrated in figure 15, the formation of such interfacial states constitutes the first step toward spin-independent, inelastic tunneling processes accompanied by magnon excitation. If these interfacial states are eliminated, electron tunneling in the antiparallel configuration could be strongly suppressed in the first place. Miura *et al* theoretically showed that inserting an ultrathin layer of Co_2CrAl or Co_2MnAl at the Co_2MnSi/MgO interface can suppress the reduction of interfacial spin polarization [94, 95] (figure 18). In particular, Co_2MnAl was predicted to be highly promising because it possesses a Δ_1 band in the majority-spin channel (figure 2) [95]. Experimentally, Ozawa *et al* demonstrated that inserting a 0.5-nm-thick Co_2MnAl layer at the Co_2MnSi/MgO interface in Co_2MnSi/MgO/CoFe MTJs leads to an approximately twofold enhancement of the RT TMR ratio [96].

Although such interfacial engineering approaches remain relatively limited so far, these results clearly indicate that there is substantial room for further improvement. Through meticulous control of Heusler electrodes and their interfaces, even larger TMR ratios may be achievable. MTJs are extremely sensitive to interface quality: even in conventional CoFe/MgO/CoFe junctions, the TMR ratio remains below 10% without careful optimization, whereas it can exceed 600% when the interfaces are precisely controlled [65]. Similar persistence and systematic optimization will undoubtedly be required for Heusler-based half-metallic MTJs.

Finally, it should be noted that the strong temperature dependence of the TMR ratio has so far been observed mainly in systems combining Co_2MnSi or $Co_2(Fe,Mn)Si$ electrodes with Al–O or MgO barriers [33, 36, 38, 41, 45]. For Heusler alloys with different compositions or for alternative barrier materials, a variety of experimental studies [97–99] and theoretical predictions [100–105] have recently been reported. Since interfacial state formation and magnetic stiffness are expected to be highly sensitive to

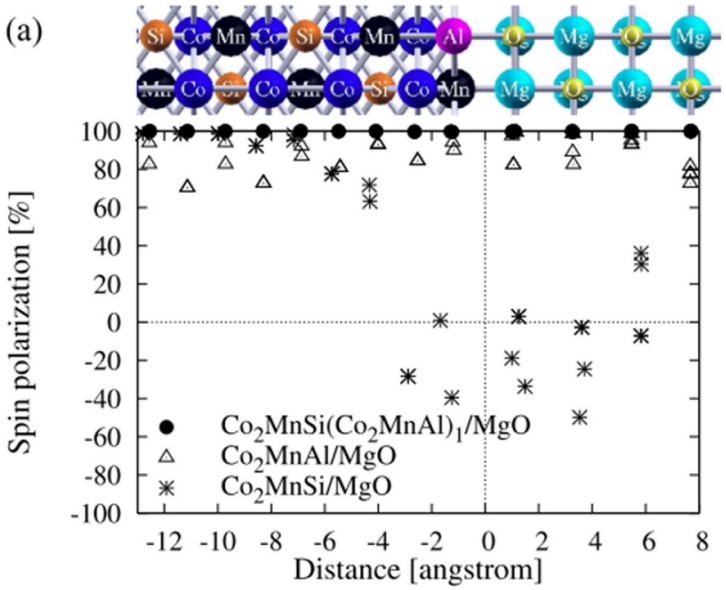


Figure 18. The spin-polarization at the Fermi level projected on to each atomic sphere as a function of the distance from interface for $Co_2MnSi/(Co_2MnAl)_1$/MgO(001), Co_2MnAl/MgO(001) and Co_2MnAl/MgO(001), respectively. Schematic figures of the supercell of the $Co_2MnSi/(Co_2MnAl)_1$/MgO(001) junction are shown above the spin-polarization. Reproduced from [95]. © IOP Publishing Ltd CC BY 3.0.

specific material combinations, continued exploration of new Heusler compounds and barrier materials represents a promising direction for overcoming the remaining limitations and achieving robust giant TMR effects at RT.

Data-driven material exploration and optimization can be one of the potential solutions to realize a breakthrough. Heusler alloys constitute a highly versatile class of multicomponent materials, as they can incorporate a wide variety of elements from the periodic table. When extended to quaternary, quinary, or even higher-order compositions, the number of possible combinations becomes extraordinarily large, opening up vast unexplored compositional spaces. Within such uncharted regions, there may exist materials that simultaneously exhibit high bulk spin polarization and improved interfacial properties, potentially overcoming current limitations in TMR performance. Although the exploration of these complex multicomponent systems has long been hindered by the huge size of the materials search space, recent advances in high-throughput computational and experimental techniques, together with machine-learning-based materials discovery, have enabled much more efficient and systematic exploration. For example, Iwasaki *et al* have developed an autonomous first-principles-based materials exploration framework that optimizes multiple target properties, such as a large half-metallic gap, a high majority-spin d-state density of states, and a high Curie temperature, and successfully identified novel half-metallic compounds [106]. Extending such approaches to more complex parameter spaces, including interfacial composition, local magnetic structure, and atomic-scale structural variations, is expected to provide a promising route toward future breakthroughs.

2.3. MTJs with tetragonal Heusler alloy electrodes

One of the most important applications for MTJs is spin-transfer-torque MRAM (STT-MRAM). Achieving high-density integration, sufficient thermal stability, and low switching current simultaneously requires MTJs that exhibit strong PMA, so called pMTJ. Conventional half-metallic Heusler alloys mentioned in the earlier section, however, tend to suffer from intrinsically low magnetocrystalline anisotropy due to their cubic structure, making their direct use in pMTJs challenging. Hiratsuka *et al* demonstrated that ultrathin Co2MnSi films deposited on $L1_0$-CoPt can exhibit PMA below 3 nm, but controlling Co2MnSi film quality at such small thicknesses remains difficult [107], and no large TMR ratios have been reported for such hybrid structures.

Meanwhile, the currently mainstream CoFeB/MgO-based pMTJs rely on interface-induced anisotropy [108] and therefore lose thermal stability as device dimensions shrink below 10 nm. Although shape-anisotropy-driven PMA has recently shown promising performance [109], fabricating sufficiently thick magnetic layers at such small dimensions presents a significant processing challenge.

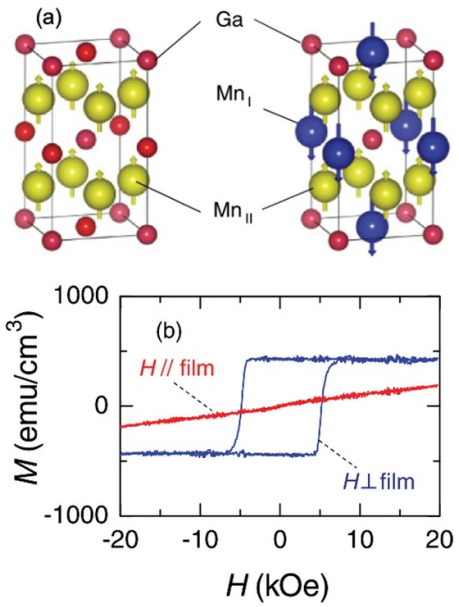


Figure 19. (a) Schematic view of the crystal structures of $L1_0$-MnGa(left) and $D0_{22}$-Mn_3Ga. (b) *M*-*H* curve of $Mn_{62}Ga_{38}$ epitaxial film grown on Cr-buffered MgO(001) substrate. Reprinted (figure) with permission from [113], Copyright (2012) by the American Physical Society.

In contrast, PMA derived from the intrinsic bulk crystalline magneto-anisotropy of the magnetic layer is highly attractive for future high-density STT-MRAM, as it can maintain thermal stability even in ultrathin films. $L1_0$-ordered alloys such as FePt, FePd and CoPt are one of the most promising materials for obtaining large PMA. It was theoretically predicted that FePt/MgO/FePt MTJs could show TMR ratios up to 380% for Fe-terminated interfaces [110]. Kim *et al* reported the TMR at RT in the MTJ with $L1_0$-CoPt alloy and MgO barrier for the first time in 2008 [111]. Afterwards TMR ratios exceeding 100% were observed by inserting Fe or CoFe at the FePt/MgO interface [112]. Nevertheless, practical implementation is hindered by the necessity of high annealing temperatures (∼500 °C) to achieve strong anisotropy and by the inherently large magnetization and damping of FePt, which impede low-current STT switching.

Mn_3Ga an Mn_3Ge and related compounds that crystallize in the $D0_{22}$ structure (figure 19) [113] Owing to the symmetry lowering induced by the tetragonal distortion from cubic full-Heusler phase ($L2_1$ space group $F_{m\bar{3}m}$), they adopt the space group $I4/mmm$ and are therefore often referred to as tetragonal Heusler compounds. In terms of crystal system, $D0_{22}$ shares the tetragonal setting with the $L1_0$ structure ($P4/mmm$), which is also known for strong uniaxial magnetocrystalline anisotropy along the *c* axis. However, because the lattice centering and the detailed atomic arrangement differ, $D0_{22}$ is treated as a distinct ordered phase rather than a simple variant of $L1_0$ (compare figure 19(a)) These $D0_{22}$ Heusler-type materials have attracted substantial interest as MTJ electrode candidates for STT-MRAM. Beyond the large PMA inherent to the tetragonal lattice, theory predicts a high spin polarization [23]. Experimentally, their ferrimagnetic nature can yield small net magnetization, and low damping has also been reported [114], both of which are favorable for reducing the STT switching current. First-principles studies further suggest that combining $D0_{22}$ electrodes with an MgO tunnel barrier can produce large TMR ratios; in particular, Mn_3Ge has been predicted to exhibit TMR exceeding 4000% due to its half-metal-like character of Δ_1-band [115].

Experimentally, Kubota *et al* fabricated epitaxial $Mn_{3-\delta}$ Ga/MgO/CoFe MTJs in 2011 and reported a RT TMR of 9.8% [116]. Introducing an Fe interlayer at the interface improved the TMR to 24% (or 57% if a fully antiparallel configuration is assumed) [117]. Sugihara *et al* subsequently demonstrated MTJs employing $D0_{22}$-Mn_3Ge/MgO and observed a RT TMR of 11.3% [118]. In these early demonstrations, however, Mn_3Ga and Mn_3Ge layers were typically thick (∼30 nm) and required relatively high growth temperatures (⩾300 °C), while MgO interface control remained insufficient; consequently, the observed TMR values were still far below what would be required for practical STT-MRAM.

A major step forward was reported in 2016 by Suzuki *et al*, who realized an extremely flat template by optimizing a Cr/B2-CoGa underlayer on MgO(001) [119]. Using this template, atomic ordered Mn–Ga ($Mn_{60.5}Ga_{39.5}$) films could be sputter-deposited at RT while retaining clear PMA even at a thickness of only 1 nm. Furthermore, by inserting Mn [119], a metastable bcc-CoMn binary alloy [120], or an

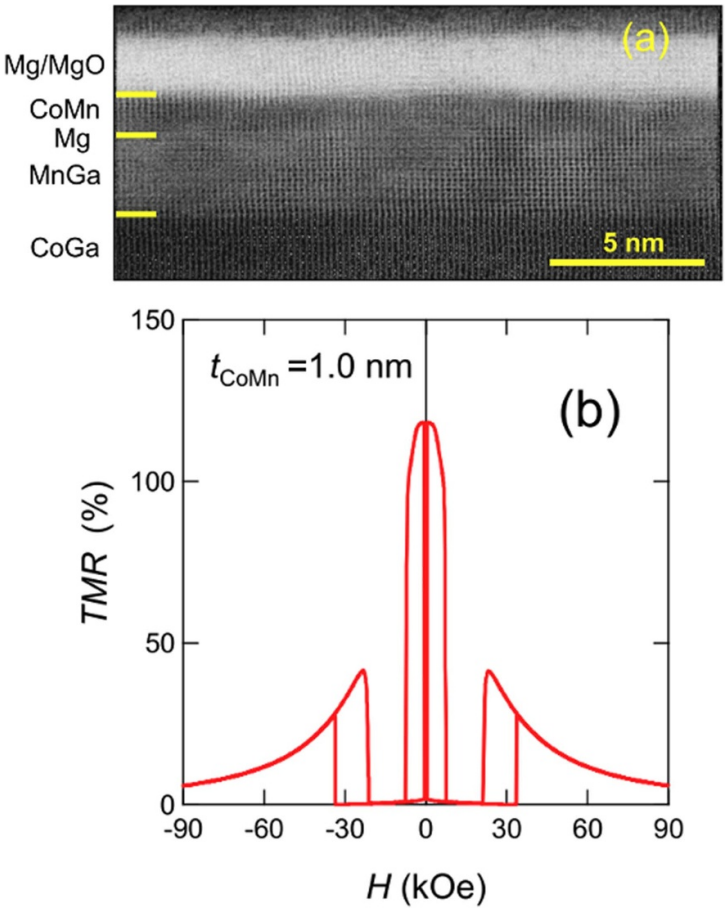


Figure 20. (a) The cross-sectional HAADF-STEM image and (b)MR curve of p-MTJ (MgO(001) substrate/Cr(40)/$Co_{55}Ga_{45}$(30)/$Mn_{61}Ga_{39}$(3)/Mg (0.4)/$Co_{80}Mn_{20}$(1.0)/Mg(0.4)/ MgO(2)/$Fe_{60}Co_{20}B_{20}$(1.4)/Ta(3)/Ru(5). Reproduced from [121]. CC BY 4.0.

ultrathin Mg/$Co_{80}Mn_{20}$ interlayer [121] at the interface between ultrathin Mn–Ga and the MgO barrier, maximum TMR ratios of 18%, 85%, and 118% at RT (figure 20) were achieved, respectively. The beneficial role of such underlayers in promoting ordering and interfacial quality—even for RT deposition—was systematically investigated by Filippou *et al* and described as a chemical templating layer (CTL) effect [122] which was shown to be extendable to a broad range of tetragonal Heusler-related materials, including Mn_3Sn, Mn_3Sb, and Mn_2CoSn.

More recently, by employing CoAl as a CTL on Si/SiO_2 substrates, which is compatible with CMOS technology, has also been explored. Mn_3Ge films were grown with a high TMR of 87%, and STT switching was demonstrated at a low current density of 10 MA/cm^2 even under short 0.5 ns write pulses [123]. Collectively, these advances highlight tetragonal Heusler alloys with PMA as promising material platforms for next-generation STT-MRAM. In parallel, first-principles screening is expanding the candidate space up to ternary compositions [124], motivating further experimental exploration and materials development.

3. CPP-GMR devices with half-metallic Heusler alloys

As discussed in the last chapter, MTJs employing half-metallic Heusler alloys suffer from a serious practical limitation: a pronounced temperature dependence of the TMR ratio, which originates mainly from magnetic and electronic reconstruction at the tunnel-barrier interfaces. In contrast, CPP-GMR devices, with a nonmagnetic metallic spacer, provide a more suitable platform for exploiting the intrinsic advantages of half-metallicity for the following reasons.

(i) In CPP-GMR devices the MR is governed not only by spin-dependent scattering at FM/nonmagnet interfaces but also by spin-dependent scattering within the FM bulk layers [2]. As a result, interface-specific problems tend to have a much weaker impact on the overall MR ratio.

(ii) The transport in CPP-GMR occurs via spin-dependent diffusive conduction, rather than ballistic transport like tunneling. Consequently, inelastic processes associated with high-energy electrons—such as magnon and phonon excitations that strongly degrade MR—are largely suppressed.

(iii) In MTJs, the MgO tunnel barrier plays a unique and somewhat 'magical' role in MTJs: coherent tunneling through evanescent states leads to strong band-selective transport, enabling conventional FMs such as Fe into materials exhibiting nearly half-metallic transport characteristics. In CPP-GMR devices, however, metallic diffusive transport does not preserve electron momentum or orbital symmetry. Therefore, such band-selective enhancement of spin polarization does not occur, and conventional FMs cannot easily generate exceptionally large spin-dependent scattering.

For these reasons, in CPP-GMR systems the intrinsic half-metallicity of the FM material itself becomes critically important, making Heusler alloy-based half-metals particularly attractive for achieving large and thermally robust MR. In addition, CPP-GMR devices inherently exhibit lower resistance–area products (RA) than TMR devices as they do not contain an insulating tunnel barrier. This low resistance is advantageous for important applications like HDD read head, as explained in detail later in section 3.2. In this chapter, the advancement of the single crystalline and polycrystalline CPP-GMR devices will be reviewed.

3.1. Single-crystalline CPP-GMR

Magnetic Heusler alloys, extensively studied as promising spintronics materials, typically possess lattice constants in the range of 5.6–5.9 Å. Epitaxial growth of single-crystalline Heusler alloy thin films has been successfully demonstrated on various substrates with matching lattice constants, such as GaAs, MgO. Among them, MgO (001) substrates are the most widely used for CPP-GMR studies owing to its chemical stability and lattice constant of = 5.957 Å, close to the lattice constants of Heusler alloys, which enables (001)-oriented epitaxial growth with the relationship of Heusler(001) [113]//MgO(001) [122]. MgO substrates are usually cleaned by ultrasonication with acetone, ethanol, and de-ionized water, followed by *in-situ* ion milling or annealing at around 600 °C. Buffer layers consisting of materials like Cr, Ag, CoFe, W as well as MgO itself are often deposited on MgO substrates, which can improve surface flatness and crystallinity and suppress secondary phase formation. These effects of buffer layers originate from the modified interfacial lattice misfit and interfacial energy. The metallic buffer layers also serve as bottom electrode in CPP-GMR devices. While polycrystalline GMR films reviewed in the later section are compatible with the fabrication process for important practical applications such as read head elements in HDDs, single-crystalline GMR films are indispensable for fundamental research aimed at exploring the intrinsic potential of Heusler alloys, for the following reasons.

First, compared with polycrystalline films, single-crystalline GMR films exhibit superior stability during high-temperature annealing. Such annealing process is essential for promoting atomic ordering in Heusler alloy films. However, in polycrystalline films, annealing typically above 450 °C disturbs the nanometer-sized layered structure, which is related to the grain boundary of polycrystalline films, affecting recrystallization and atomic diffusion. In this respect, single-crystalline films with no grain boundary can withstand high temperature annealing, allowing the intrinsic properties of the material to be accessed.

Second, single-crystalline films enable detailed structural analysis using XRD and transmission electron microscope (TEM). The degree of atomic ordering in Heusler layers can be quantitatively evaluated using established methods based on the XRD intensity ratios between fundamental and superlattice. In particular, for Heusler alloys containing Co, Fe, and Mn with close atomic numbers, synchrotron-based anomalous XRD (AXRD) [87, 125] has proven to be a powerful tool for precise analysis of atomic ordering. In TEM observation, accurate alignment of zone axis is possible with single-crystalline films, allowing atomic resolution imaging.

Third, single-crystalline films grown with (001) texture allow for well-defined interfaces between Heusler alloy and spacer layers. These sharp and coherent interfaces contrast with those in polycrystalline films, where Heusler generally form (110) texture creating unmatching interface with widely used spacer materials such as fcc-based Cu and Ag, and such unmatched interfaces can hinder spin-dependent transport due to increased electron scattering. In this respect, matched interfaces in single-crystalline GMR films allow investigating the intrinsic spin-dependent transport.

3.1.1. Epitaxial CPP-GMR device with Heusler alloys with positive spin polarization

Co-based Heusler alloys such as Co_2MnSi are prototypical half-metallic materials and have been widely used as electrodes in CPP-GMR devices. After it became clear that the strong temperature dependence

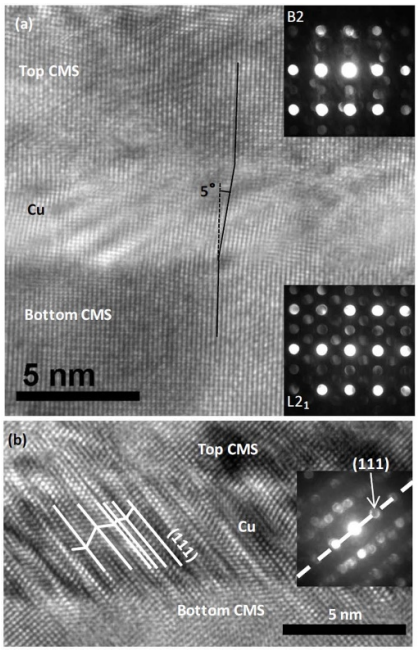


Figure 21. Cross-sectional TEM image and nanobeam diffraction patterns obtained from CMS/Cu/CMS structure for electron beam parallel to the (a) [122] and (b) [113] directions. Reprinted from [128], with the permission of AIP Publishing.

of the TMR ratio in MTJs originates primarily from interfacial effects, research efforts aimed at extending these materials to CPP-GMR systems intensified. In this section, we review studies on nonmagnetic spacer materials, interfacial modification, and related approaches that have been carried out to achieve larger MR ratios in epitaxial CPP-GMR structures.

3.1.1.1. Cr spacer

In 2006, GMR devices employing Co_2MnSi (CMS) Heusler alloy first demonstrated an MR ratio of 2.4% in CPP configuration [126]. The pseudo-SV (PSV) structure was MgO(001)sub./Cr(10 nm)/CMS(40 nm)/Cr(3 nm)/CMS(10 nm)/Cr(3 nm), where the bottom CMS layer was deposited at 300 °C while the layers above the bottom CMS layer were deposited at RT, leaving the top CMS layer unannealed. The devices were fabricated by patterning the film into pillar structures with lateral dimensions of 0.50 × 0.23 μm^2. The *RA* value was calculated to be 0.794 $\Omega \cdot \mu m^2$ from device resistance and area, which was relatively high compared to values reported in subsequent studies. This large calculated *RA* is likely due to non-uniform current distribution. The thin bottom Cr layer, in relation to the lateral size of the pillar, may have caused current concentration near the pillar edges, leading to the high *RA* value.

3.1.1.2. Cu spacer

Cu was also explored for a spacer material as Cu has large spin-diffusion length and is the standard spacer material for GMR devices using conventional CoFe-based material. In 2009, MR ratio of 8.6% at RT (30.7% at 6 K) was demonstrated for the SV structure consisting of MgO(001) sub./Cr(10 nm)/Ag(200 nm)/Cr(10 nm)/CMS(20 nm)/Cu(4 nm)/CMS(5 nm)/CoFe(2 nm)/IrMn(10 nm) /Ru(5 nm), annealed twice at 400 °C after the deposition of the bottom CFAS layer and at 300 °C after the device fabrication [127]. The Cu spacer layer was grown epitaxially with relationship of CMS(100) [122]//Cu(001) [001], but a small lattice rotation of about 5° between CMS and Cu and defects were observed, which is likely due to the large lattice mismatch of −9.7% between CMS and Cu. The defects of the Cu spacer were identified as multitwins on the (111) planes (figure 21) [128]. Such dense disorder in Cu spacer might hinder a spin transport as well as deteriorate a structural thermal stability.

3.1.1.3. Ag spacer

In 2008, a higher MR ratio of 6.9% at RT (14% at 6 K) was reported for CPP-GMR devices with $Co_2FeAl_{0.5}Si_{0.5}$ (CFAS) and an Ag spacer [129]. The use of the Ag spacer was motivated by better lattice matching with CFAS and its long spin-diffusion length. The SV structure was MgO(001)sub./Cr(10

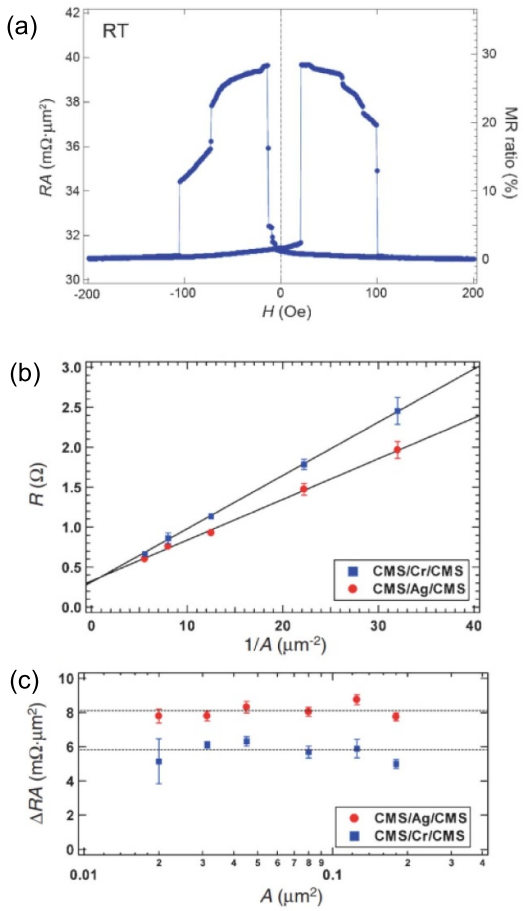


Figure 22. (a) MR curve showing 28.8% MR ratio at RT. (b) Device size dependence of device resistance and (c) ΔRA for Ag and Cr spacers. Reproduced from [130]. ©2009 The Japan Society of Applied Physics.

nm)/Ag(200 nm)/CFAS(20 nm)/Ag(5 nm)/CFAS (5 nm)/CoFe(2 nm)/IrMn(10 nm)/Ru(8 nm). The bottom CFAS layer was deposited RT and post-annealed at 400 °C, followed by annealing at 250 °C in an in-plane field after the device fabrication to induce exchange bias via the IrMn layer.

In 2009, a significantly large MR ratio of 28.8% at RT was reported for a device consisting of MgO(001)subs./Cr(20 nm)/Ag(40 nm)/Cr(10 nm)/CMS(8.8 nm)/Ag(5 nm)/CMS(8.8 nm)/Ag(2 nm)/Au(5 nm), as shown in figure 22(a) [130]. The observed MR ratio was nearly an order of magnitude larger than MR ratio reported in conventional polycrystalline CoFe/Cu/CoFe device [131], suggesting a contribution of half-metallic nature of CMS on the enhancement of MR ratio even at RT. Both bottom and top CMS layers were post-annealed at 500 and 450 °C, respectively, after deposition of each layer to induce $L2_1$-ordering. The use of a thick, low-resistivity Ag buffer layer contributed to improved current uniformity inside the pillar, enabling accurate estimation of *RA*. The accuracy of *RA* was confirmed by the linear relation of the device resistance on the inverse of the device area for devices with various sizes (figure 22(b). Here, the slope represents *RA*, which is estimated to be 51.4 $m\Omega{\cdot}\mu m^2$, and the intercept represents the parasitic resistance due to the current crowding in the bottom and top electrodes. This study compared Ag and Cr spacers, and the devices with a Cr spacer showed higher *RA*. This increased *RA* cannot be explained by the different bulk resistivity between Ag and Cr, indicating higher interface resistance. Moreover, the Ag spacer sample exhibited higher ΔRA (figure 22(c), demonstrating its advantages.

A report in 2010 investigated the mechanism behind the large MR achieved with Ag spacers by combining experiments with first-principles calculation on the CMS/Ag/CMS system [132]. The devices consisting of MgO(001)subs./Cr(20 nm)/Ag(40 nm)/CMS(t_{CMS} nm)/Ag(5 nm)/CMS(t_{CMS} nm)/Ag(2 nm)/Au(5 nm) with various t_{CMS} from 3 to 11. By measuring the dependence of MR property on t_{CMS} (figure 23(a), bulk and interfacial spin-asymmetry contributions are separated using Valet–Fert model, which indicated a large interfacial spin asymmetry at CMS/Ag. First-principles calculations indicated the high majority-spin conductance at the CMS/Ag interface owing to good Fermi-energy matching, supporting the experimental findings. This study also reported the post-annealing temperature

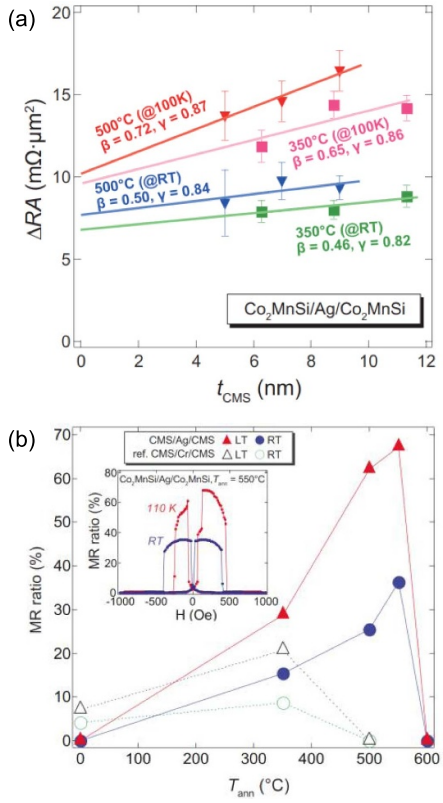


Figure 23. (a) CMS thickness dependence of ΔRA for the samples annealed at 350 and 500 °C with fitting based on the Valet–Fert model. (b) Annealing temperature dependence of MR ratio for CMS/Cr/CMS and CMS/Ag/CMS. Reprinted (figure) with permission from [132], Copyright (2010) by the American Physical Society.

dependence of MR ratio (figure 23(b), In which increased monotonically up to 550 °C, reaching 36.4% at RT, and decreased at 600 °C. In contrast, CMS/Cr/CMS devices showed degradation at 500 °C due to interdiffusion between CMS and Cr, indicating the superior thermal tolerance of Ag spacers. Higher temperature tolerance of Ag spacer is advantageous as annealing at higher temperatures can improve half-metallicity of the Heusler layers through promoted atomic ordering.

The analysis on bulk and interfacial spin asymmetry was advanced in 2011 by a study on CFAS/Ag/CFAS [133, 134]. The resistance of the $[CFAS/Ag(5)]_N$/CFAS multilayers (N = 1, 3, and 5) was measured to estimate the interfacial resistance between CFAS and Ag (figure 24(a)). Further, MR properties were measured from the devices with MgO subs./Cr(10 nm)/Ag(100 nm)/CFAS(t_F)/Ag(5 nm)/CFAS(t_F)/Ag(5 nm)/Ru (8 nm) with t_F = 2.5–22 nm annealed at 500 °C (figure 24(b)). Based on these results, interfacial contribution was decomposed into interfacial resistance for parallel configuration and spin-asymmetry coefficients, yielding their values of 0.25 mΩ·μm^2 and 0.77 at RT, respectively.

In 2011, pseudo-spin valve structure consisting of MgO(001)subs./Cr(20 nm)/Ag(50 nm)/CFMS (20 nm)/Ag(5 nm)/CFMS(10 nm)/Ag(3 nm)/Ru(3 nm), annealed twice at 500 °C and 450 °C after deposition of each CFMS layers, demonstrated an MR ratio of 74.8%, which belongs to the highest reported values [135]. Regarding the high MR values, $Co_2FeGe_{0.5}Ga_{0.5}$(CFGG) has been playing a central role since its first report in 2011 [136] Co2Fe-based Heusler alloys generally exhibit higher thermal tolerance than Co2Mn-based due to the lower solubility of Fe in Ag than Mn, enabling high annealing temperatures for improved atomic ordering. The advantage of CFGG was supported by the first-principles calculation, which indicated high majority-spin conductance and high exchange stiffness at CFGG/Ag interface [137]. In 2013, MR ratio of 57% at RT (183% at 10 K) was reported for CFGG/Ag/CFGG PSV structure annealed at very high temperature of 600 °C [138]. This study also reported that *in-situ* post-annealing after the deposition of top CFGG layer and before the deposition of capping Ag/Ru layers can suppress diffusion at this high temperature annealing.

3.1.1.4. Ultrathin insertion layer effect at Ag spacer interface

Several studies reported the effect of thin insertion layer at the interface between the magnetic layer and spacer layer. The NiAl thickness dependence on the MR properties for CFGG(10 nm)/NiAl(t_{NiAl})/Ag(5 nm)/NiAl(t_{NiAl})/CFGG showed maximum at t_{NiAl} = 0.2 nm (figure 25), where MR ratio reached 82%

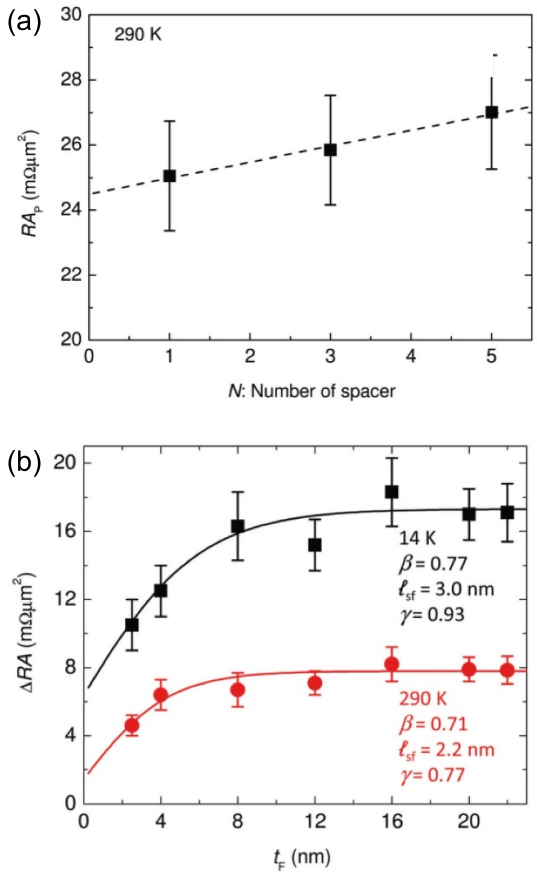


Figure 24. (a) Dependence of *RA* on *N* for $[CFAS/Ag(5)]_N$/CFAS multilayer in the parallel configuration. (b) CFAS thickness dependence of ΔRA at RT and 14 K with fitting based on the Valet–Fert model. Reprinted from [133], with the permission of AIP Publishing. Reprinted from [134], with the permission of AIP Publishing. Reprinted from [123], with the permission of AIP Publishing.

at RT (285% at 10 K) [139]. The NiAl thickness dependence on the MR properties for CFGG(10 nm)/NiAl(t_{NiAl})/Ag(5 nm)/NiAl(t_{NiAl})/CFGG showed maximum at t_{NiAl} = 0.2 nm (figure 25) TEM observation revealed enrichment of Ni, Al and Ga at the Ag/CFGG interface, indicating the formation of B2-ordered Ni(Al,Ga). First-principles calculations showed that CFGG and NiAl exhibit better band matching than CFGG and Ag and that NiGa have similar properties to NiAl, supporting the experimental results. This high MR ratio was reproduced by using a similar structure using CFGG and NiAl insertion in 2022, reporting 87.9% which is the highest value to date [140]. The study also found a crucial role of Ge compositions in obtaining high MR ratio, demonstrating the advantage of Ge-rich CFGG.(figure 26). It was also reported that, by inserting an ultrathin Ni layer with a thickness of approximately 0.2 nm at the CFGG/Ag interface, the MR ratio was enhanced by nearly 1.5 times [141]. Atomic-resolution TEM revealed that Co atoms in the terminating layer of CFGG at the interface are replaced by Ni. First-principles calculations based on this interfacial structural model demonstrated that this substitution increases the interfacial transmission probability of majority-spin electrons, which was identified as the microscopic origin of the MR enhancement. The fact that the MR ratio can be significantly improved by modifying the interface structure at the single–atomic-layer level is particularly noteworthy, even in a system governed by diffusive metallic transport.

3.1.1.5. Composition tuning of Heusler electrodes

Composition tuning is crucial for improving MR in Heusler alloy-based CPP-GMR devices as already discussed regarding the Ge composition of CFGG [140] Other than that, there have been various study on composition tuning. For example, the Fe/Mn ratio was focused in $Co_2Fe_xMn_{1-x}Si$ (CMFS), and the GMR devices with $Co_2Fe_xMn_{1-x}Si$(20 nm)/Ag(5 nm)/$Co_2Fe_xMn_{1-x}Si$(7 nm) for x = 0, 0.2, 0.3, 0.4, 0.5, 1 annealed at 500 °C exhibited the maximum MR ratio at x = 0.4 reaching 48% (figure 27) [142]. The effect of composition tuning is understood by various mechanisms, such as adjusting the Fermi energy near the center of the band gap, improved exchange stiffness at interfaces by substitution of Mn with Fe, exclusion of abundant atoms to promote atomic ordering. Recently, high-throughput experimental

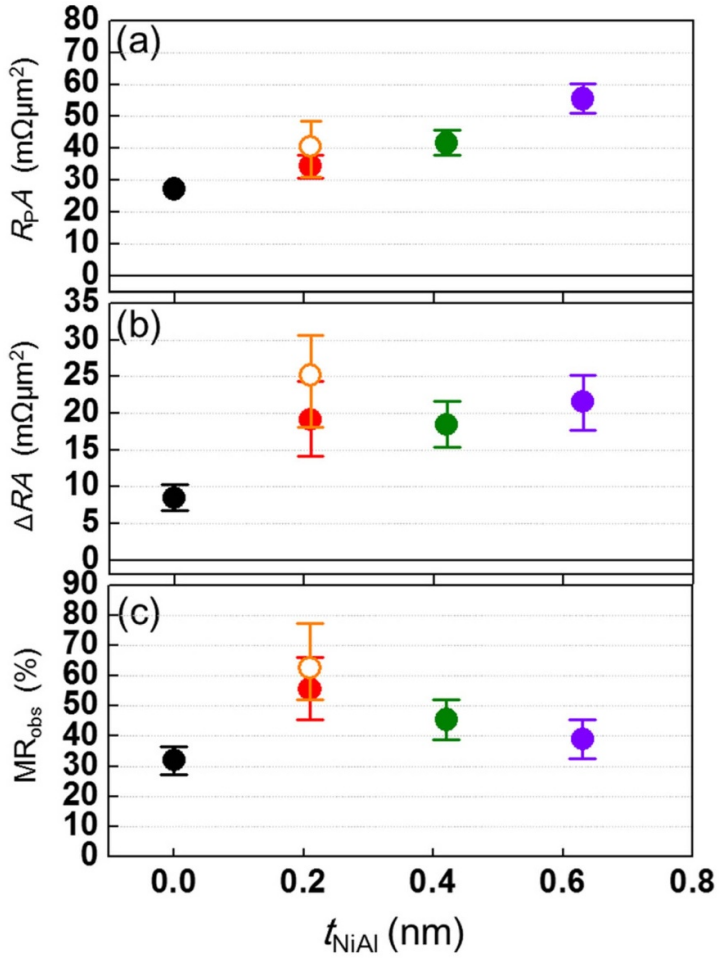


Figure 25. NiAl thickness dependence of (a) *RA*, (b)Δ*RA*, and (c) MR ratio for CFGG/NiAl/Ag/NiAl/CFGG. Reprinted from [139], with the permission of AIP Publishing.

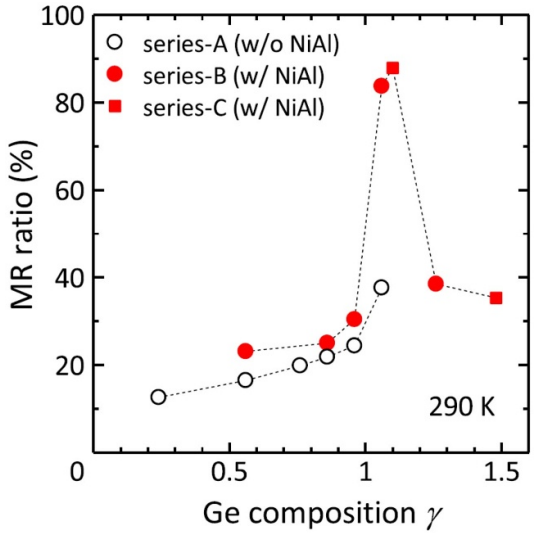


Figure 26. Ge-composition dependence of MR ratio for GMR stack with and without NiAl insertion. Reproduced from [140]. © IOP Publishing Ltd All rights reserved.

method for composition optimization was developed and applied to the Fe/Mn ratio in $Co_2Mn_xFe_{1-x}Ge$ [143]. In this method, composition gradient layers were fabricated by the combinatorial sputtering system. This system enables an alternating deposition of wedge-shaped CFG and CMG layers with each having gradual thickness change from 0 to 0.5 nm. Repeating the set of deposition of CFG and CMG

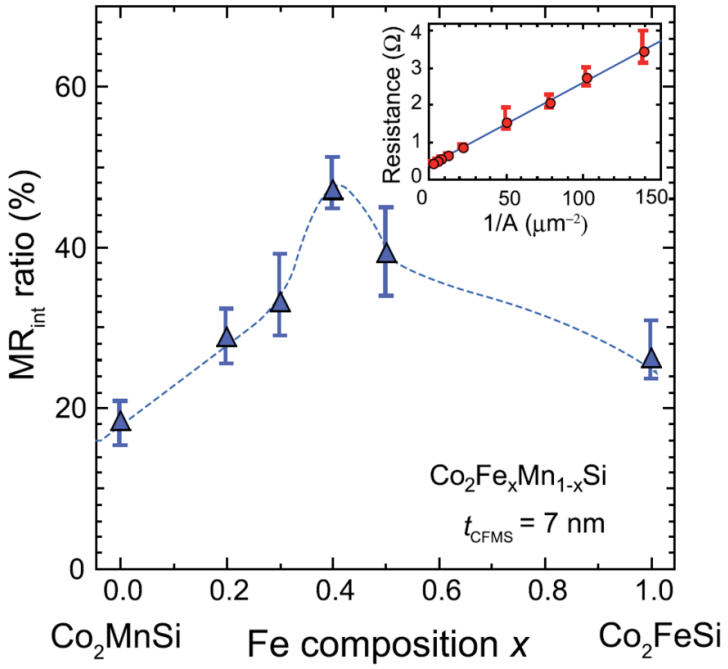


Figure 27. Fe composition dependence of MR ratio for CMFG/Ag/CMFG. Reprinted from [142], with the permission of AIP Publishing.

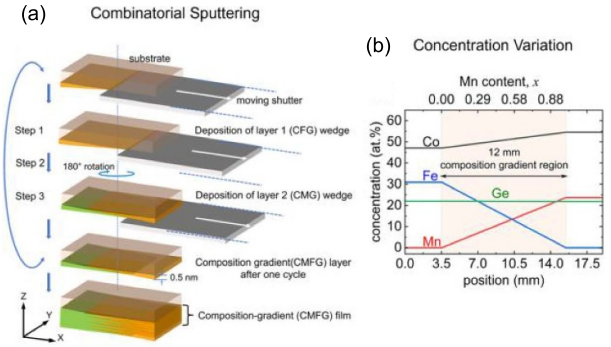


Figure 28. (a) Schematic showing the combinatorial sputtering deposition process. (b) Variation of atomic concentration in $Co_2Mn_xFe_{1-x}Ge$ composition-gradient film. Reproduced from [143]. CC BY 4.0.

for 14 times fabricated 7 nm thick $Co_2Mn_xFe_{1-x}Ge$ layer ($0 \leqslant x \leqslant 1$), which was used in the library sample consisting of $Co_2Mn_xFe_{1-x}Ge$(7 nm)/AgSn(5 nm) $Co_2Mn_xFe_{1-x}Ge$(7 nm). CPP-GMR devices fabricated densely across the sample enabled examination of the composition at fine intervals, achieving significantly higher throughput than the conventional approach of preparing samples for each studied composition. (figure 28) The MR ratio showed clear composition dependence, peaking at $x = 0.85$ for post-annealing at 250 °C, successfully identifying the optimal composition. This study reported 38% and 45% MR ratio at annealing temperatures of 250 °C and 350 °C, respectively, which is highest for the devices processed in this relatively low annealing temperature range, demonstrating the advantage of this materials system for the use with temperature limitation.

3.1.1.6. Spin-dependent scattering at half-metallic FM/normal FM interface

In the studies presented above, magnetic layers in GMR devices were composed of a single Heusler alloy. In 2021, a new approach using bilayer consisting of two FM layers CoFe/CFMS was presented for enhanced MR properties [144]. The PSV structure was MgO(001)subs./Cr (20 nm)/Ag(80 nm)/$Co_{50}Fe_{50}$(7 − t nm)/CFMS(t nm)/Ag(5 nm)/CFMS(t nm)/$Co_{50}Fe_{50}$(7 − t nm)/Ag(5 nm)/Ru(8 nm) with various t of 0 (pure CoFe), 0.75, 1.5, 3, 4, 5, and 7 nm(pure CFMS), which was annealed twice at 450 °C after the deposition of bottom and top CFMS layers, respectively. The MR ratio showed a maximum of 50% at $x = 4$ nm, which is significantly higher than 25% at $x = 7$ nm

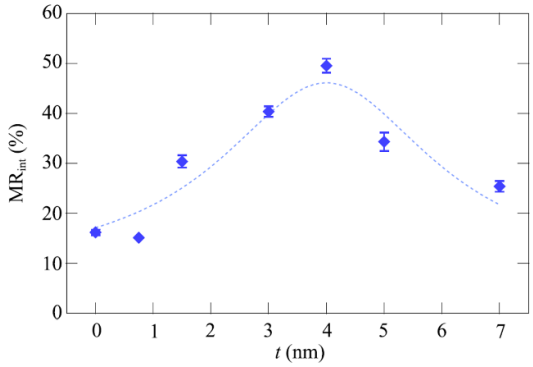


Figure 29. (a) CFMS thickness dependence of MR ratio for CoFe(7 − t nm)/CFMS(t nm)/Ag(5 nm)/CFMS(t nm)/CoFe(7 − t nm)/. Reprinted (figure) with permission from [144].

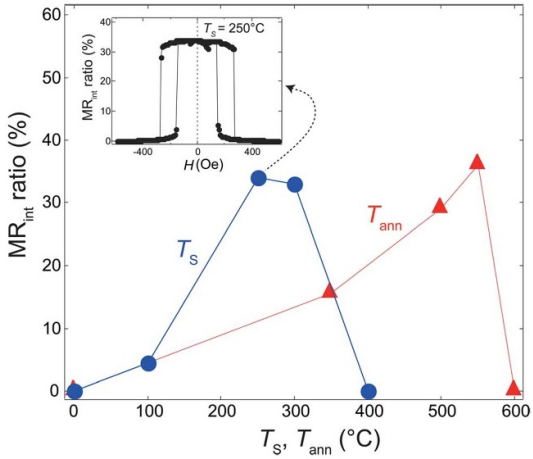


Figure 30. (a) Process temperature dependence of MR ratio for CMS/Ag/CMS obtained from devices fabricated with elevated temperature deposition and post annealing. © (2013) IEEE. Reprinted, with permission, from [145].

(pure CMFS) (figure 29). First-principles calculation indicated that the principle behind this enhancement of MR is spin-scattering asymmetry at FM CFMS/CoFe interface. The calculated majority- and minority-spin conductance at this interface showed a large difference, providing additional contribution to MR change in the device with a shorter CFMS thickness than its spin-diffusion length.

3.1.1.7. Elevated temperature deposition of Heusler electrode

Heusler layers in these studies have been treated mainly by two thermal processes: post-deposition annealing and elevated temperature deposition. Post-annealing is more commonly employed as this method can suppress interdiffusion and roughness increase. On the other hand, elevated temperature deposition can generally achieve higher atomic ordering than post-annealing when compared at the same process temperature. This advantage is attributed to the additional energy provided by incoming sputtered particles, which assist atomic ordering beyond the solo effect of temperature. A study in 2013 compared these two methods for CMS(20 nm)/Ag(5 nm)/CMS(9 nm) devices [145]. The devices with elevated-temperature deposition of two CMS layers yielded a maximum MR ratio of 35% at 250 °C, with degradation occurring at 400 °C (figure 30). Note that the Ag spacer was deposited after cooling down. Post-annealing achieved similarly high MR ratios at 550 °C, with degradation occurring at 600 °C. These results demonstrated the advantage of elevated-temperature deposition for devices with strict thermal budgets.

3.1.1.8. Wafer bonding of single crystalline CPP-GMR

Utilizing the superior properties of single-crystalline devices in practical applications is ideal, but it is hindered by the requirement for epitaxial growth on special single-crystalline substrates. In addition, incompatibility of heat treatment at high temperatures in device manufacturing processes is

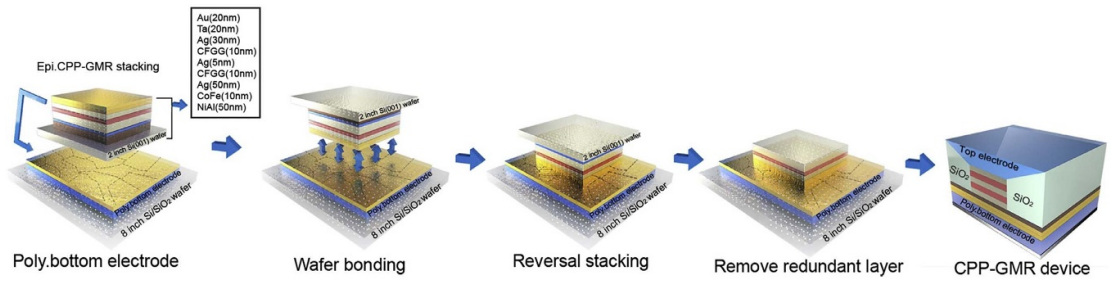


Figure 31. Process of transferring single-crystalline CFGG/Ag/CFGG device films by direct wafer bonding and substrate removal, followed by device fabrication. Reproduced with permission from [146]. CC BY-NC-ND 4.0.

an issue. Namely, when Heusler alloys are implemented in MRAMs and HDD read heads, the process temperatures are limited by the thermal stabilities (thermal budget) of the back-end-of-line Cu interconnects typically at up to 400 C and NiFe magnetic shields at up to 300 C, respectively, and these temperature limitation prevent Heusler alloys from fully exhibiting their potential. To overcome this issue, transferring single-crystalline device films onto device structures by direct wafer bonding and substrate removal has been explored (figure 31) [147] In this technique, epitaxial Si(001)sub./NiAl/CoFe structure was developed to achieve single-crystalline (001)-oriented growth, as MgO substrates are unpractical from the viewpoints of limited available wafer size and high costs. The single-crystalline PSV film consisting of Si(001)sub./NiAl(50 nm)/CoFe(10 nm)/Ag(50 nm)/CFGG(10 nm)/Ag(5 nm)/CFGG(10 nm)/Ag(5 nm)/Au(5 nm) annealed at 500 °C was transferred to a polycrystalline electrode with an Au capping layer by means of *in-situ* Ar ion cleaning and bonding of the two Au surface in vacuum. CPP-GMR devices fabricated after the film transfer exhibited MR properties identical to those fabricated from the original film prior to transfer, confirming the viability of this integration method. This was the first demonstration of the wafer bonding of epitaxial spintronic device on the polycrystalline electrode.

3.1.1.9. STT application

Other than the large MR effects discussed so far, efficient STT arising from high spin polarization is another advantage of Heusler-based devices. In addition, half-metallic Heusler alloys exhibit very low damping parameter, and thus use of Heusler alloys in free magnetic layers whose magnetization direction is manipulated by STT can reduce the operation current. The physics behind low damping is explained as follows. Damping is considered to be proportional to DOS at E_F, and the presence of only one type of (spin-up or down) DOS in half-metallic material can result in low α. Furthermore, spin-flip scattering channels are suppressed by half-metallicity, contributing to a further reduction in the damping. STT serves as the operation principle for magnetization switching in magnetoresistive memory devices and magnetization oscillation in spin-torque oscillators (STOs). In particular, GMR-based STT devices have been applied in STOs used in microwave-assisted magnetic recording, a next-generation HDD technology [148]. In this application, an STO is integrated into the write gap of a write head with typical gap distance of 20 nm, and high-frequency magnetic field in the GHz range generated from the magnetization oscillation induces excitation of media magnetizations to assist magnetization switching. Because the STOs for this purpose require strong STT to induce oscillation of a large magnetic volume for enhanced assist effect, all-metallic GMR structures with high current-density durability, combined with the enhanced spin polarization provided by Heusler alloys, are suitable.

In 2016, magnetization oscillation was demonstrated in a mag-flip type STO. The structure consist of MgO(001)sub./Cr(10 nm)/Au(100 nm)/$L1_0$-FePt(10 nm)/CFGG (3 nm)/Ag(5 nm)/CFGG(7 nm)/Ag(5 nm)/Ru(7 nm) fabricated with complex thermal treatments: annealing at 600 °C after the Au layer to improve the surface flatness, followed by elevated-temperature deposition of FePt at 450 °C to induce $L1_0$ atomic ordering, and annealing at 500 °C after the deposition of the top CFGG layer to promote the atomic ordering of the CFGG layers [149]. In this type of STO, the FePt and bottom CFGG layer constitute the spin-injection layer (SIL), where the FePt and CFGG layers provide perpendicular magnetization and high spin polarization, respectively. The top CFGG layer serves as the field-generating layer (FGL), where magnetization oscillation is induced by STT via spin injection from SIL. By applying a bias current with a current density on the order of 10^8 A cm^{-2}, resistance change indicating magnetization oscillation of FGL and high-frequency signals at approximately 15 GHz were detected (figure 32). The high-frequency signal originated from the resistance oscillation by MR effect due to the magnetization

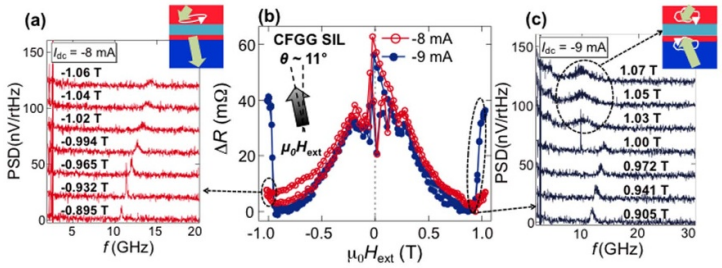


Figure 32. (a) Spectrum of high-frequency STO signal at bias current of −8 mA. (b) Corresponding field dependence of ΔR. (c) Spectrum of high-frequency STO signal at bias current of −9 mA. Reprinted from [149], with the permission of AIP Publishing

oscillation and thus represents the oscillation frequency. This study also fabricated a comparative sample using CoFe in SIL instead of CFGG and demonstrated that the samples with CFGG can reduce the operation current by 50%, providing evidence of superior spin-injection efficiency of CFGG due to its high spin polarization. This study was further advanced in 2017 by employing CoFe in FGL [150]. As the oscillation of a large magnetic volume is a key in this application, CoFe with high M_s is ideal for this layer.

Subsequently, a different type of STO, referred to as all-in-plane STO, was proposed and studied. Unlike mag-flip STOs, this design eliminates the need for materials with PMA, reducing the device thickness, which is suitable for devices fabricated in a small write gap. Additionally, all-in-plane STOs operate with complex dynamics, in which magnetizations in both field-generating and spin-injection layers oscillate through the mutual spin injection. While this complex operation offers benefits such as reduced operation current and short onset time of magnetization oscillation, it also complicates the material design. Experimental and simulation study all-in-plane STOs with CoFe SIL(3 nm)/Ag (5 nm)/CoFe FGL (7 nm) and CFAS SIL(3 nm)/Ag (5 nm)/CoFe FGL (7 nm) revealed that using CFAS SIL increased operation current, which was explained as follows [151]. In this type of STO, reversal of the SIL magnetization typically initiates the oscillation process, and high spin polarization in SIL can decrease STT acting on SIL hindering its oscillation. These results demonstrated the importance of carefully designing spin polarization in devices with complex dynamics.

Recently, a simplified method for analyzing STT efficiency was proposed, using basic GMR structures with in-plane magnetic layers and resistance measurement in a perpendicular magnetic field [152]. In this STT measurement, the magnetization directions are first aligned to the perpendicular direction by a strong magnetic field to overcome the demagnetizing field, and then magnetization reversal of one magnetic layer is induced by applying a bias current and detected through the resistance change, from which STT efficiency can be estimated. This technique was applied to GMR devices with CMFG(15 nm)/Ag(5 nm)/NiFe(7 nm) annealed at 350 °C after the deposition of CMFG layer, where the NiFe magnetization was reversed against the perpendicular field via spin injection from the CMFG layer [143]. The results demonstrated approximately two-fold increase in the STT efficiency of CMFG in comparison with CoFe.

3.1.2. Epitaxial CPP-GMR device with Heusler alloys with negative spin polarization

In contrast to positive spin polarization materials discussed above, several types of Mn-based Heusler alloys are predicted to have a gap in the majority-spin band, resulting in conduction of highly spin polarized electrons with spin direction opposite to the magnetization direction (negative spin polarization) [153]. Consequently, negative spin polarization materials can reverse the sign of MR and STT, as follows. Asymmetric GMR devices consisting of positive and negative spin polarization materials exhibit high (low) resistance for a parallel (antiparallel) magnetic configuration, opposite to the standard MR behavior. Spin injection from negative spin polarization materials can exert STT with opposite direction to that from positive spin polarization materials. In particular, STT application attracts attention because negative spin polarization materials can increase freedom in device designs, enabling performance improvements beyond the limitation of positive spin polarization materials. Despite its potential, negative spin polarization materials have been far less explored than positive spin polarization materials.

In 2024, Mn_2VAl (MVA) demonstrated negative MR, indicating negative spin polarization [154]. The PSV structure consisting of MgO(001)sub./Cr(5 nm)/Ag(100 nm)/Cr(5 nm)/W(5 nm)/MVA(10 nm)/Ag(5 nm)/$Co_{50}Fe_{50}$(7 nm)/Ru(8 nm), where MVA layer was deposited at 500 °C, reported a negative MR of −4.4% at RT (figure 33). This value is much higher than that reported in PSV CPP-GMR with

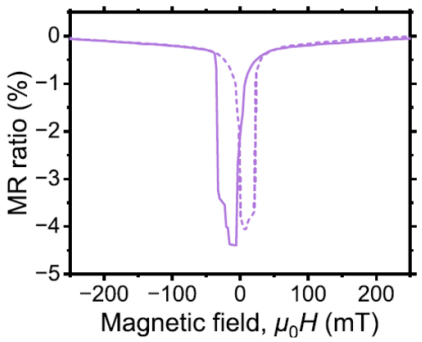


Figure 33. MR curve showing −4.4% MR ratio for MVA/Ag/CoFe. Reproduced from [154]. CC BY 4.0.

conventional negative spin-polarized materials such as FeCr [155] and the highest value ever reported, though its amplitude is much lower than those reported in positive spin polarization materials. The small negative MR is partly due to the CoFe layer with lower spin polarization used in the positive spin polarization side. In addition, first-principles calculation showed that minority-spin conductance at Ag/MVG interface is much lower than majority-spin conductance of CFGG/Ag, suggesting that Ag spacer is not suitable in this system. The STT measurement confirmed high STT efficiency with direction reflecting negative spin polarization of MVA, demonstrating its potential for controlling STT direction in advanced device architectures. Similarly, negative spin polarization was reported in Mn_2VGa [156].

3.1.3. Compound spacer materials

3.1.3.1. NiAl spacer

Ag has been found to be a suitable single-element spacer material for Heusler alloy-based CPP-GMR devices, with advantages such as thermal stability and high majority-spin conductance. To further improve the MR property from the viewpoint of spacer materials, compound materials have been explored. In 2012, *B*2 NiAl was studied for a spacer in CPP-GMR devices with $Co_2MnGa_{0.5}Sn_{0.5}$ (CMGS) [157] -based *B*2 structure can form a matching interface for either (001)- or (110)-textured Heusler alloy films. This is in contrast to fcc Ag, which does not form a matching interface with (110)-textured Heusler alloys typically obtained in polycrystalline films, such unmatching interfaces potentially lead to degraded spin transport. Additionally, NiAl exhibits good band matching with Ag, as already discussed regarding NiAl insertion [139]. The SV structure was MgO(001)sub./Cr(10 nm)/Ag(75 nm)/NiAl(10 nm)/CMGS(20 nm)/NiAl(5 nm)/CMGS(5 nm)/CoFe (2 nm)/IrMn(10 nm)/Ru(8 nm). From the annealing temperature dependence of MR, NiAl was found to achieve high temperature tolerance up to 550 °C in comparison with 400 °C for Ag spacer. However, MR ratio of 7.0% for the NiAl spacer sample was smaller than that of the Ag spacer sample, presumably due to the short spin diffusion length of NiAl, which was reported to be 8.1 nm.

3.1.3.2. CuZn spacer

*B*2 CuZn, which contains neither heavy nor magnetic elements, has longer spin diffusion length than NiAl and was also employed as a spacer material. Experimental report in 2012 used the PSV structure of MgO(001)sub./Cr(10 nm)/Ag(100 nm)/CFGG(10 nm)/CuZn(5 nm)/CFGG(10 nm)/Ag(5 nm)/Ru(8 nm) annealed at several temperatures from 300 °C to 500 °C [158]. At 350 °C, MR ratio reached a high value of 25.3%, which surpasses that of the reference sample with Ag spacer at around similar annealing temperatures, demonstrating its advantage. TEM observation confirmed the formation of CuZn spacer and revealed that the thin CuZn spacers formed *A*2 structure, despite that single-layer 50 nm CuZn deposited on MgO(001) substrate showed *B*2 structure (figure 34(a)). At 400 °C, significant change of the GMR stack occurred, as revealed by change in XRD and TEM analysis (figure 34(b)). A Ag spacer was formed instead of CuZn as Cu and Zn diffuse to several places in the stack. Interestingly, the film after the structural change at 400 °C still shows MR though the distribution in MR is large. These results indicate that CuZn spacer is promising for applications with process temperature below 350 °C due to the low thermal stability. Recent detailed theoretical study on Cu-based spacer materials with *B*2 structure reported higher majority spin conductance of CuZn/CFGG than Ag/CFGG originating from better Fermi-energy matching, which supports the advantage of CuZn over Ag [159].

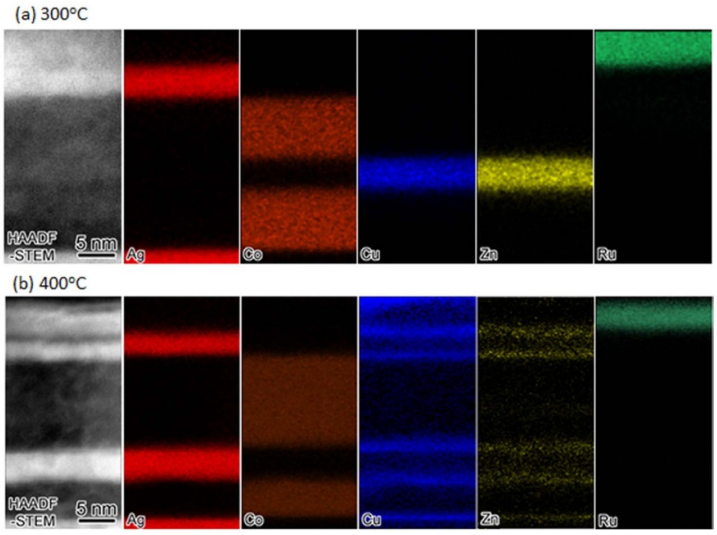


Figure 34. HAADF-STEM images and EDS mappings of CFGG/CuZn/CFGG for annealing temperature of (a) 300 °C and (b) 400 °C. Reprinted from [158], with the permission of AIP Publishing.

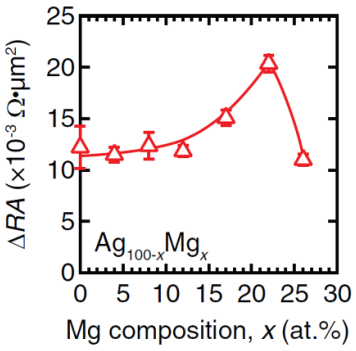


Figure 35. Mg composition dependence of ΔRA *for* CFMS/$Ag_{100-x}Mg_x$/CFMS. Reproduced from [160]. © IOP Publishing Ltd All rights reserved.

3.1.3.3. Ag_3Mg spacer

$L1_2$ Ag_3Mg is another potential spacer material. Although Ag_3Mg shares the fcc-based structure of Ag and thus faces similar interface mismatching issues with (110)-textured films, first-principles calculation indicated better majority-spin electronic band matching at Ag_3Mg/CFMS than at Ag/CFMS suggesting superior property. Experimental study in 2017 fabricated series of PSV samples having MgO(001)sub./Cr(20 nm)/Ag(40 nm)/CFMS(20 nm)/$Ag_{100-x}Mg_x$(5 nm)/CFMS(7 nm)/Ag(2 nm)/Au(5 nm) with x ranging from 0 (pure Ag) to 26% [160]. TEM observation confirmed fcc-based structure in x range of 0%–22% and clear $L1_2$ atomic ordering at x= 22%. The ΔRA value showed maximum at x = 22% with an MR ratio of 56% demonstrating the advantage of $L1_2$ Ag_3Mg spacer (figure 35). At x= 26%, epitaxial growth was disturbed, resulting in decreased MR. In addition to the predicted good band matching, it was suggested that incorporating Mg into spacer can suppress interdiffusion between CMFS/spacer. In relation to this study, there have been reports on the fabrication of (001)-textured Heusler based CPP-GMR stacks in polycrystalline films, suggesting that fcc-based spacer materials can be adapted for practical applications through such techniques [161].

3.1.3.4. Nonmagnetic Heusler spacer

Heusler alloy spacer materials offer structural compatibility with either (001)- or (110)-textured films due to their shared crystal structure with the magnetic layers. In 2009, Nikolaev *et al*, reported achieving a CPP-GMR ratio of 6.7% and a RA of 4 Mω μm^2 using a SV structure with Co_2MnGe FM Heusler layers and Rh_2CuSn (RCS) non-magnetic Heusler spacer [162]. In 2016, Cu_2TiAl (CTA) Heusler alloy was investigated as a spacer material for the use with $Co_2MnGa_{0.5}Ge_{0.5}$ (CMGG) magnetic layers [163]. Among the vast variety of Heusler alloys, CTA was selected on the basis of first-principles transport

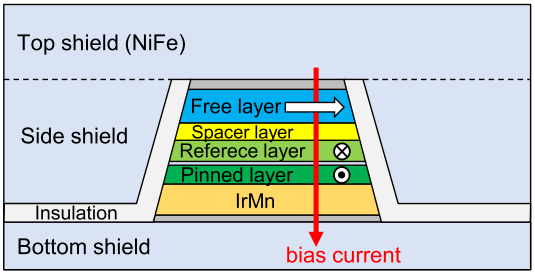


Figure 36. Schematic structure of the CPP-GMR read head from the recording media side (air bearing surface).

calculation, which predicted the good properties both for (001) or (110) textures. The 001-textured PSV structure was prepared with MgO(001)sub./Cr(10 nm)/Ag(100 nm)/CMGG(10 nm)CTA(t_N nm)/CMGG(10 nm)/Ag(5 nm)/Ru(8 nm), where the CMGG and CTA layers were deposited at 300 °C. At $t_N = 2$ nm, an MR ratio of 17% was obtained, comparable to that of a reference sample with an Ag spacer, demonstrating the potential of CTA. However, the MR ratio decreases severely with increasing t_N, indicating short spin-diffusion length of CTA. This study also fabricated (110)-textured single crystalline films on sapphire(110)subs. /Ta(10 nm)/W(100 nm) and demonstrated an MR ratio of 12.5%. These results indicated that CTA spacer could mitigate the orientation dependence of MR output, which is usually observed in Ag-spacer CPP-PSV. The smaller MR for (110)-texture could be attributed to the different atomic ordering of the CMGG layers due to the different underlayer.

3.2. Polycrystalline CPP-GMR device with Heusler alloys for read head application

As discussed in previous sections, several Co-based Heusler alloys exhibit half-metallic electronic band structures and Curie temperatures well above RT. This makes them promising candidates for generating highly spin-polarized currents and spin sources in spintronic devices. For this reason, Co-based Heusler alloys have been implemented as the FM layers in CPP-GMR devices for the application to future read heads of HDDs [162, 164–167]. CPP-GMR devices with metallic spacer layers typically exhibit a lower *RA* of approximately 0.05 Ω μm^2, compared to over 0.2 Ω·μm^2 for TMR devices. This lower *RA* helps reduce thermal Johnson noise in read heads [168, 169].

Figure 36 shows the schematic structure of a read head from the air bearing surface facing the magnetic recording media. SV type magnetic sensors are surrounded by NiFe magnetic shields that absorb magnetic flux from the adjacent recording bits, improving the spatial resolution of the read head. To fabricate the read heads, the SV stack is deposited on a NiFe bottom shield fabricated by plating and planarized by chemical-mechanical polishing. Therefore, CPP-GMR devices for read head applications must be composed of polycrystalline films. In this section, we review the development of polycrystalline CPP-GMR devices.

As shown in figure 36, the bottom-pinned SV structure is used for read heads due to the stronger pinning field of the magnetic pinned layer (PL) compared to the case with top-pinned SV structure. In the bottom-pinned structure, the (0001)-textured Ru underlayer achieves the high (111)-texture of the IrMn anti FM layer, which is critical for strong exchange bias. The magnetic PL is usually a Co-rich bcc-CoFe alloy, e.g. $Co_{70}Fe_{30}$, from an exchange bias perspective [170]. The PL/Ru/reference layer (RL) trilayer is often referred to as a synthetic anti FM (SAF) structure. The magnetizations of the PL and RL are usually designed to be equal, though this is not necessarily required. They are strongly coupled in an antiparallel direction by the anti FM interlayer exchange coupling of the typically 0.8-nm-thick Ru layer. The usage of the SAF structure reduces the magnetic stray field from the PL to the free layer (FL) and enhances the stability of the pinning. Co-based Heusler alloys can be used for both PL and FL. Additionally, selecting the appropriate nonmagnetic spacer layer is important for high-performance CPP-GMR devices.

There are two major requirements for Heusler alloy-based CPP-GMR read heads: First, the annealing temperature is typically limited to up to 300 °C. This is due to the degradation of the soft magnetic properties of the NiFe shields. Second, the total thickness of the sensor stack, corresponding to the spacing between the top and bottom shields (shield-to-shield spacing, SSS), is limited to below 25 nm, because SSS determines the spatial resolution of the read head in the bit length direction. Considering the thickness of each layer in the SV structure, the RL and FL should be approximately 5 nm or thinner.

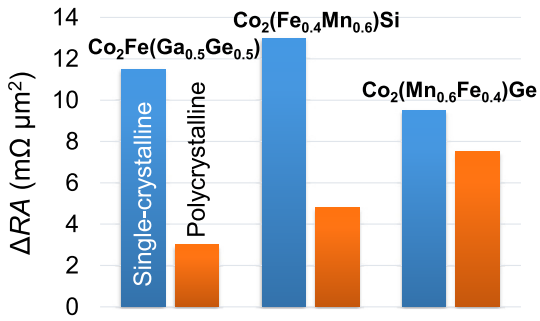


Figure 37. ΔRA of single-crystalline (blue) and polycrystalline (orange) pseudo spin-valve devices with $Co_2Fe(Ga_{0.5}Ge_{0.5})$, $Co_2(Fe_{0.6}Mn_{0.4})Si$, and $Co_2(Mn_{0.6}Fe_{0.4})Ge$ Heusler alloys. © (2018) IEEE. Reprinted, with permission, from [68].

3.2.1. Selection of Heusler alloy composition

Of the many variations of Co-based Heusler alloys with high spin polarizations, a consensus has emerged regarding the composition of alloys suitable for polycrystalline CPP-GMR devices. These are Co_2MnGe [167] and Co_2(Mn, Fe)Ge [171], based on experimental observations showing a high MR ratio than other compositions under the restriction of annealing temperature. Although reports on systematic comparisons of different alloy systems are limited, Nakatani *et al* [68] compared three representative quaternary Heusler alloys for CPP-GMR, $Co_2Fe(Ga_{0.5}Ge_{0.5})$ (CFGG) [136], $Co_2(Mn_{0.6}Fe_{0.4})Si$ (CMFS) [142], and $Co_2(Mn_{0.6}Fe_{0.4})Ge$ (CMFG) [171]. These alloys exhibit relatively high ΔRA values and CPP-GMR ratios. Figure 37 shows the ΔRA values of the CPP-GMR devices with epitaxially grown (001) single-crystalline and polycrystalline structures. The single-crystalline devices were annealed at various temperatures ranging from 300 °C to 600 °C; the polycrystalline devices were annealed at a fixed temperature of 300 °C. Devices with CFGG and CMFS exhibited high ΔRA values above 11 mΩ μm^2 through high-temperature annealing at 600 °C and 500 °C, respectively. This was attributed to the $L2_1$ ordering of these alloys. Conversely, the polycrystalline films annealed at 300 °C retained the B2 ordered structure for all alloys, with CMFG showing the highest ΔRA. The reason for the higher ΔRA value of CMFG compared to those with CFGG and CMFS has not been reported; however, the difference in the degree of B2 order (S_{B2}) is likely to be the key factor.

The B2 ordering tendency of Heusler alloys can be qualitatively predicted based on the melting point (T_m) and the order-disorder transformation temperature ($T_{order-disorder}$). T_m indicates the mobility of atoms. Atoms are more mobile at a given temperature for a material with lower melting point. $T_{order-disorder}$ indicates the phase stability of the $L2_1$ ordered structure. Sputtered films are quenched from vapor to solid during deposition; therefore, as-sputtered Heusler alloy films are usually in a non-equilibrium disordered state with either an A2 or B2 structure. Upon annealing, the degree of order in the films improves. Considering the kinetics and driving force of atomic ordering, lower T_m and higher $T_{order-disorder}$ are preferred, respectively.

Table 2 summarizes the T_m and $T_{order-disorder}$ of various Co-based Heusler alloys in bulk samples. No $T_{order-disorder}$ has been observed for Co_2MnSi, Co_2MnGe, and Co_2FeGe, indicating that their $L2_1$-ordered structures are stable up to T_m. This indicates that these alloys have a high driving force for the atomic ordering from a disordered state. The Ge-containing alloys, such as Co_2MnGe and Co_2FeGe, have lower T_m than the other alloys. Therefore, Co_2MnGe and Co_2FeGe have higher atomic mobility than the other alloys and are advantageous for achieving high degree of order. Page *et al* studied the compositional dependence of ΔRA and S_{B2} in polycrystalline CPP-GMR SVs with $Co_2(Mn_{1-x}Fe_x)Ge$ (x = 0.0–0.4) [171]. As shown in figure 38(a), ΔRA for $x = 0.2$ and 0.4 was significantly higher than that for $x = 0.0$ and 0.1. Conversely, S_{B2}, as measured by a laboratory XRD system, was the highest for $x = 0.0$ and decreased as x increased, as shown in figure 38(b). While these results appear contradictory, the authors argue that *s–d* scattering may explain the higher ΔRA for $x = 0.2$ and 0.4.

3.2.2. Amorphous underlayer enhancing ordering

Choi *et al* [172] reported an enhancement in the ΔRA of SVs with $Co_2(Mn_{0.6}Fe_{0.4})Ge$ (CMFG) when a thin CoFeBTa (CFBT) underlayer of less than 1 nm was inserted for the CMFG layer. CFBT contains 7 at. % of Ta to stabilize its amorphous structure at elevated temperatures. Figure 39(a) shows the saturation magnetization of a 5-nm-thick CFBT film during continuous heating from a RT to a high temperature. At ∼450 °C, the magnetization-temperature curve of the CFBT film exhibited a kink,

Table 2. Melting point (T_m) and order-disorder temperature ($T_{order-disorder}$) of bulk Heusler alloys. $T_{order-disorder} > T_m$ indicates that $T_{order-disorder}$ is not observed below T_m, namely, intermetallic compound. © (2018) IEEE. Reprinted, with permission, from [68].

Alloy	T_m (K)	$T_{order-disorder}$ (K)
Co_2MnAl	∼1400	950
Co_2MnSi	1438	$> T_m$
Co_2MnGa	1440	1200
Co_2MnGe	1346	$> T_m$
Co_2FeAl	∼1700	990
Co_2FeSi	1520	1400
Co_2FeGa	∼1550	1100
Co_2FeGe	1420	$> T_m$

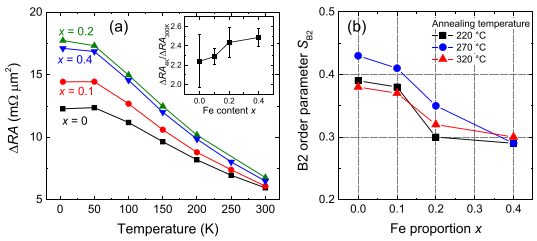


Figure 38. (a) Temperature dependence of ΔRA of CPP-GMR spin-valves with $Co_2(Mn_{1-x}Fe_x)Ge$ ferromagnetic layers with various Fe content x. (b) S_{B2} for various x and annealing temperatures. Reprinted from [171], with the permission of AIP Publishing.

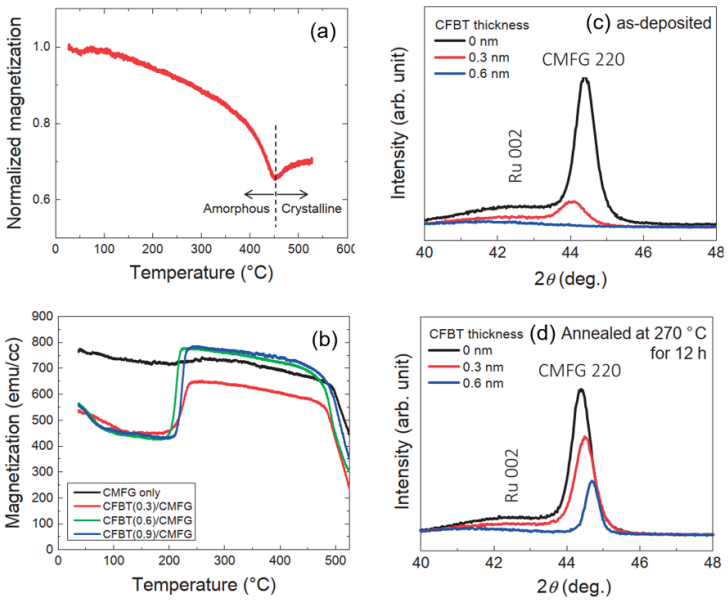


Figure 39. Magnetization-temperature curves of (a) CFBT (5) and (b) Ta (5)/Ru (5)/CFBT (0–0.9)/CMFG (20)/Ru (10) (thickness in nm) films during continuous heating. Out-of-plane XRD profiles of Ta (5)/Ru (5)/CFBT (0–0.9)/CMFG (20)/Ru (10) films (c) in the as-deposited state and (d) after annealing at 270 °C for 12 h. Reproduced from [172]. © 2017 The Japan Society of Applied Physics.

corresponding to the crystallization of the amorphous CFBT film. Figure 39(b) shows the magnetization-temperature curves of CMFG films deposited on Ru and CFBT underlayers. At RT, the CMFG films on a CFBT underlayer exhibited lower saturation magnetization than that on a crystalline Ru underlayer. When the films were heated to ∼220 °C, the magnetization of the CMFG film deposited on the CFBT underlayer increased. This increase corresponds to the crystallization of the CMFG films from amorphous to (110)-text polycrystals, as shown in the XRD profiles (figures 38(c) and (d)).

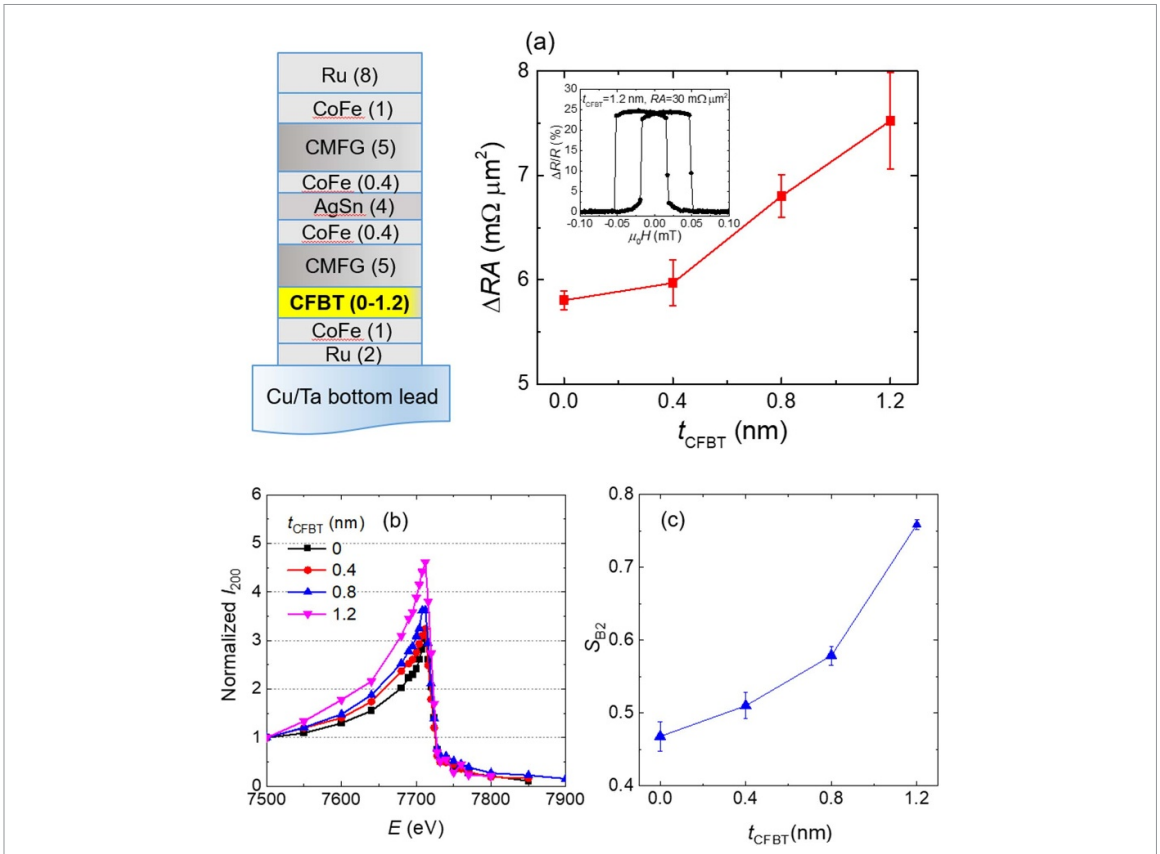


Figure 40. (a) Structure of CPP-GMR pseudo spin-valves and their ΔRA values for CFBT thickness (t_{CFBT}). (b) AXRD measurements: x-ray energy (E) dependence of the XRD intensity from the (200)-plane of CMFG (30 nm) plane (I_{200}) normalized at the value at $E = 7500$ eV. (c) S_{B2} of the CMFG (30 nm) films estimated by the AXRD measurements. Reprinted from [66], Copyright (2018), with permission from Elsevier.

Li *et al* [66] studied the effect of the amorphous CFBT underlayer on the S_{B2} of CMFG films. They characterized the atomic ordering between Co and *Y*-elements (Mn and Fe) using AXRD with synchrotron x-ray sources. Due to their similar atomic scattering factors, the atomic ordering between Mn, Fe, and Co cannot be distinguished by laboratory x-ray sources, such as Cu-K_α line. The atomic scattering number is modulated at the x-ray energy (E) of absorption edge of the elements (6537.7 eV, 7110.8 eV, and 7708.8 eV for the K absorption edge of Mn, Fe, and Co, respectively [173]), which is called anomalous dispersion effect. Thus, the atomic ordering between these elements exhibits contrast near the absorption edges of the constituent elements. As shown in figure 40(a), ΔRA increased when a CFBT underlayer was inserted below the CMFG RL, consistent with the report by Choi *et al* [172]. Figure 40(b) shows the XRD intensity of the 200 B2 superlattice reflection (I_{200}) for different E. At around the K-absorption edge of Co ($E = 7708.8$ eV), I_{200} shows contrast for different CFBT thickness (t_{CFBT}), reflecting different values of S_{B2}. Figure 40(c) shows the dependence of S_{B2} on t_{CFBT}, obtained by comparing the experimental data (figure 40(b)) with simulations. S_{B2} significantly increases with increasing t_{CFBT}. The enhancement of S_{B2} in the polycrystalline CMFG layers by inserting a CBFT underlayer is considered to be due to B2 ordering that occurs simultaneously with crystallization from the amorphous state of CMFG.

In a follow-up study, Nakatani *et al* [174] reported that the dependence of S_{B2} on the CMFG thickness for both with and without a CFBT underlayer. With a CFBT underlayer, a 4-nm-thick CMFG film maintained S_{B2} of 0.85, which was much higher than the S_{B2} value of 0.57 for a 4-nm-thick CMFG film without a CFBT underlayer.

3.2.3. Spacer materials

3.2.3.1. AgSn alloy spacer

In the early development of Heusler alloy-based CPP-GMR read heads, Cu spacer layers were used [165–167]. However, since an Ag spacer layer performs better than a Cu spacer layer in epitaxially grown single-crystalline CPP-GMR devices (see section 3.1.1), Ag was considered for use as a spacer layer in polycrystalline CPP-GMR devices. However, there are fundamental issues with using Ag as a spacer

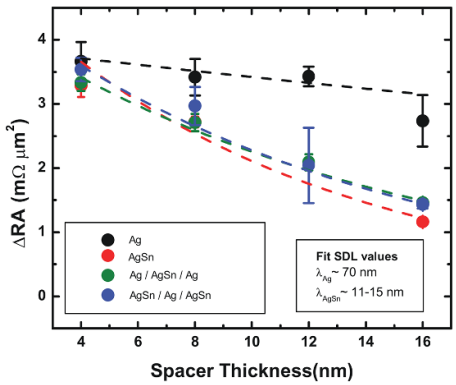


Figure 41. ΔRA for thickness of Ag and $Ag_{84}Sn_{16}$ spacer layers, yielding the spin diffusion length of Ag and $Ag_{84}Sn_{16}$ to be ∼70 nm and 11–15 nm, respectively. Reprinted from [176], with the permission of AIP Publishing.

layer in polycrystalline devices. For example, the surface of Ag films tends to be relatively rough, which increases the FM orange-peel coupling between the FM layers separated by a Ag spacer. Additionally, Ag has poor corrosion resistance during the rapping process of recording head manufacturing. Additionally, polycrystalline Ag thin films tend to agglomerate due to recrystallization at elevated temperatures during annealing of the Heusler alloy FM layers [175]. This increases the roughness of the Ag spacer layer and further increases the orange-peel coupling.

To overcome the disadvantages of Ag spacer layer, Read *et al* developed a AgSn alloy spacer layer containing Sn of up to 20 at. % [176]. Alloying Sn with Ag significantly improved corrosion resistance, as demonstrated by submerging Ag and AgSn films in distilled water. The grain size of the AgSn films was smaller than that of the Ag films, and the AgSn films exhibited a smaller tendency toward grain growth (recrystallization) at elevated temperatures compared to the Ag films. Due to these properties of AgSn, the thickness of AgSn spacers can be reduced to 2–3 nm while maintaining a relatively small orange-peel coupling strength. This ensures magnetization rotation in response to an external magnetic field. This is also advantageous for reducing the total thickness of CPP-GMR devices, which is crucial for improving the spatial resolution of read heads. Alloying Sn with Ag increases its resistivity up to ∼70 $\mu\Omega$·cm and reduces the spin diffusion length to 11–15 nm at RT (∼70 nm for pure Ag), as shown in figure 41. The spin diffusion length of AgSn with 4% Sn has been reported to be ∼26 nm at 4.2 K [177, 178]. However, the AgSn spacer layer thickness of 3 nm is much shorter than the spin diffusion length of AgSn. Thus, the CPP-GMR ratios using AgSn spacer layers are comparable to those using pure Ag spacer layers. Currently, AgSn is used as a standard spacer material for polycrystalline CPP-GMR devices [68, 161, 171, 179].

3.2.3.2. Unconventional spacers

In addition to metal and alloy spacers, various other spacer materials have been developed. In the early stages of CPP-GMR head development, as illustrated in figure 42, a current confinement path (CCP) spacer layer was used for CoFe FM layers [180–182]. In the CCP spacer layer, metal channels, typically made of Cu, are dispersed in an insulating matrix, such as amorphous AlO_x. The electric current is concentrated through the metal channels, which enhances the MR ratio. Such a Cu:AlO_x nanocomposite CCP spacer layer is formed by oxidizing a CuAl film. CCP spacer layers have also been adopted for use in Heusler alloy-based CPP-GMR devices [183].

Shimazawa *et al* reported a CPP-GMR ratio of 21.4% at $RA = 0.2\ \Omega\ \mu m^2$ using SVs with CoFe FM layers and a Cu/ZnO/Zn spacer layer, as shown in figure 43(a) [184]. Based on the TEM observations and the noise characteristics of the devices, they concluded that the electronic transport through the Cu/ZnO/Zn spacer layer was metallic and not tunneling, and that formation of CCP was not confirmed. Later, they reported a CPP-GMR ratio of 25% at $RA = 0.2\ \Omega\ \mu m^2$ using a Cu/GaO_x/Zn spacer layer, where the GaO_x was amorphous [185].

Nakatani *et al* reported an MR ratio of 25% at $RA = 0.1\ \Omega\ \mu m^2$ with CPP-GMR SVs using CFMG FM layers and a Ag/In–Zn–O (IZO)/Zn spacer layer [179, 186]. IZO is known to be a transparent conductive oxide. Using a AgSn metallic spacer layer for SV yielded an MR ratio of 15% at $RA = 0.05\ \Omega\ \mu m^2$. Obtaining a large MR ratio at $RA = 0.1\ \Omega\ \mu m^2$ is significant because the required MR ratio for 2 Tbit/in^2 is minimized at this RA value [168, 169]. However, this RA range had never

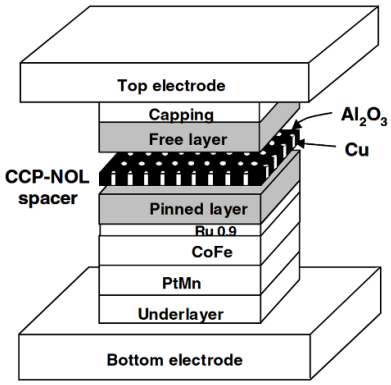


Figure 42. Schematic structure of CPP-GMR spin-valve with CCP-spacer where Cu metallic paths are dispersed in insulating Al_2O_3 matrix. Reproduced from [182]. © IOP Publishing Ltd All rights reserved.

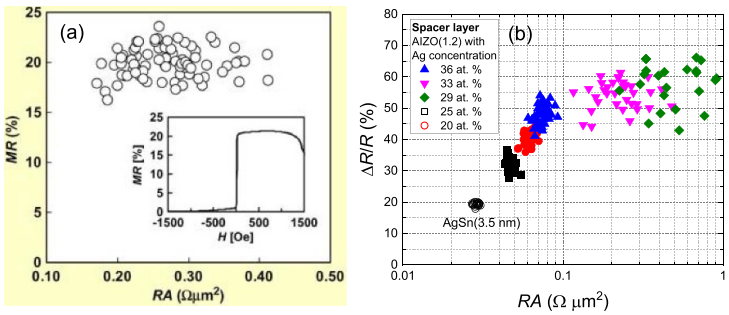


Figure 43. MR ratio vs. *RA* of (a) spin-valves with CoFe ferromagnetic layers and a Cu/ZnO/Zn spacer layer, © (2010) IEEE. Reprinted, with permission, from [184] and (b) pseudo spin-valves with CMFG ferromagnetic layers and Ag–In–Zn–O spacer precursors, which resulted in Ag–In:Mn–Zn–O nanocomposite spacer layers. Reprinted from [188], with the permission of AIP Publishing.

been achieved by either CPP-GMR devices with metallic spacers or TMR devices. Through TEM analysis, the MR enhancement mechanism using the Ag/IZO/Zn spacer layer was found to be similar to that of CCP spacer layers, such as Cu:AlO_x [187]. They found that the actual spacer structure in the nominally CMFG/CoFe/Ag/IZO/Zn/CoFe/CMFG CPP-GMR device was a nanocomposite where Ag-In metallic paths were dispersed in a Mn–Zn–O matrix (Ag–In:Mn–Zn–O nanocomposite). This nanostructure is believed to result from a reduction-oxidation reaction between In_2O_3 in IZO and Mn in CMFG, i.e. $In_2O_3 + 3Mn \rightarrow 2In + 3MnO$. The reduced In atoms alloy with Ag, and the Ag–In paths are formed. Using an Ag–In–Zn–O 'precursor' co-sputtered from Ag and IZO targets further improved the MR ratio [188]. The Ag–In–Zn–O precursor also resulted in an Ag–In:Mn–Zn–O nanocomposite spacer, and an MR ratio of up to 54% at $RA = 0.075\ \Omega\ \mu m^2$ in pseudo SVs with CMFG FM layers, as shown in figure 43(b). This large MR ratio is explained by the high spin polarization of the CMFG layers and the good matching of the spin resistance between the CMFG layers and the Ag-In paths, as predicted by the theoretical model developed for CCP spacers [189].

3.2.4. Summary and future outlook

In this chapter, we have reviewed the progress of CPP-GMR devices employing Heusler alloys, covering both single-crystalline and polycrystalline films. Single-crystalline CPP-GMR devices allow investigation of the intrinsic potential of Heusler alloys and a microscopic understanding of spin-dependent transport, owing to well-defined crystal structures, high thermal stability, and atomically sharp matched interfaces. Large MR ratios and high STT efficiency are demonstrated, clearly highlighting the advantage of half-metallic Heusler alloys. Through these extensive studies, the design principles have been established, revealing the importance of precise composition tuning of Heusler alloys, spacer materials with high majority-spin conductance at the interface, interfacial tailoring at the monolayer level.

In contrast, polycrystalline CPP-GMR devices play a central role in practical applications, particularly HDD read heads. This application imposes two major requirements: the annealing temperature and the

thickness of the stack are limited to typically below 300 °C and 25 nm, respectively Accordingly, extensive efforts have been made for optimization under these limitations, including the selection of Heusler alloy compositions, underlayers, and spacer materials. In particular, a CCP spacer layer is unique and has been proven effective in increasing MR ratio and tuning *RA* into an optimal range for application. As a result, sizable performance has been achieved even under severe thermal and structural constraints. Nonetheless, a performance gap remains between single- and polycrystalline devices, which primarily originate from incomplete atomic ordering in thin polycrystalline Heusler alloys layers due to limited annealing temperature, as well as from unmatched interface with the spacer. A key challenge is therefore the development of fabrication technique to induce high atomic and interfacial order in polycrystalline films within thermal budgets. Several promising directions have been reported from recent studies, as introduced below.

Non-equilibrium annealing using nanosecond-pulsed laser offers one such approach, as it prevents sustained exposure to high temperatures. Because laser absorption and heat generation occur predominantly near the film surface, steep temperature gradients along the thickness direction can provide sufficient thermal energy to Heusler-based device layers at the surface while protecting underlying structures with strict thermal limits [190].

Controlling the texture of the polycrystalline films has been considered. While Heusler alloys in polycrystalline films tend to form (110)-texture corresponding to the densest atomic plane, engineering the growth direction toward (001)-texture can prevent the problem of unmatched interface with fcc-based spacer materials such as Ag. Recent studies have reported fabrication of (001)-texture polycrystalline Heusler-based films and its advantage over the conventional (110) texture, indicating the benefits of controlled texture on interfacial spin transport [161].

In addition, the use of underlayers with atomic ordering can promote atomic ordering of Heusler layers deposited on top, which is called chemical template layer. During the growth of Heusler alloys, sputtered constituent atoms occupy a specific site on the template layer due to the preferential chemical bonding, promoting the atomic ordering at the initial growth. Using this method, improved magnetic properties have been reported for Mn-based Heusler alloys with thicknesses as small as approximately 2 nm [122].

Continued efforts to employ the above emerging techniques, as well as to explore other novel strategies, will be essential for further improving the performance of Heusler-based CPP-GMR devices and for narrowing the gap between single-crystalline and polycrystalline devices in future magnetic recording and spintronic applications.

4. Ge-based vertical spintronic devices based on Heusler compounds

4.1. Issues in SC-based spintronic devices and proposal for vertical-type Ge-channel spin field-effect transistors (FETs)

As emerging technologies for low-electric-power consumption SC devices, spin FETs [191, 192], which combine the processing functionality of conventional transistors with nonvolatile memory functionality due to the MR effect, have been extensively explored [193–202]. Until now, prototype operations of back-gate-type spin metal–oxide–SC FETs (MOSFETs) [203] and vertical-type spin MOSFETs [204] have been demonstrated. In [203], however, an insulator MgO tunnel barrier was used for achieving spin injection from a FM into silicon (Si), resulting in high resistance of the SC devices. In addition, the channel layer was made of a commercially available Si-on-insulator substrate with doping. Because the gate electrode was a simple back-gate structure, a high voltage above 50 V was required to achieve the switching operation and their prototype devices were not suitable for high device integration. Furthermore, the magnitude of the MR ratio was ∼0.04%, significantly lower than conventional TMR and CPP-GMR devices and insufficient for actual applications. A vertical-type spin MOSFET, where a current flows perpendicular to the film plane and is controlled by a gate electrode applied from the side surface of the SC channel, has been expected to achieve both large MR ratio and large current modulation at low voltages. A GaMnAs-based vertical spin MOSFET is one of the examples of experimental demonstration [204]. While the large MR ratio up to ∼7% was obtained and the operating gate voltages were lower than Ref [203], the operation temperature was limited to LTs because of the low Curie temperatures of the GaMnAs FM layers. From the viewpoint of practical applications and RT operation, technological breakthroughs are required to overcome these limitations.

For the next-generation SC-based spintronic devices with ultra-low electric power consumption and RT operation, a germanium (Ge)-based vertical-type spin transistor based on FM Heusler alloys (figure 44(a)) has been proposed [194]. Ge has higher electron and hole mobility than Si, making it

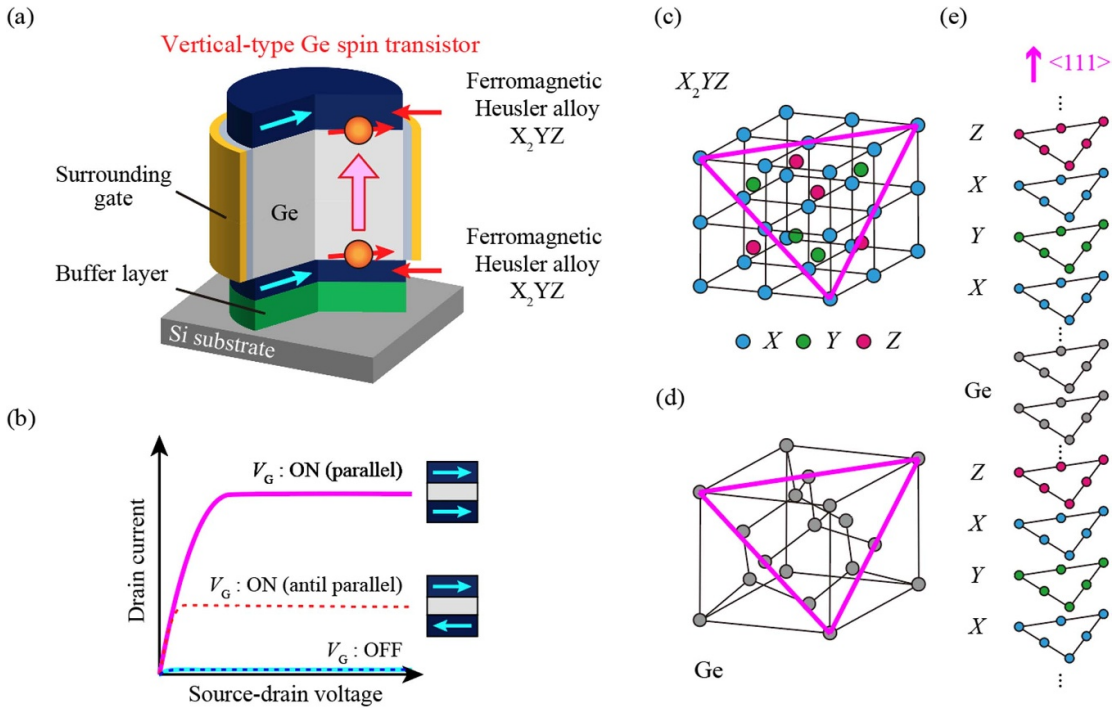


Figure 44. (a), (b) Schematic of a vertical-type Ge-based spin transistor based on Heusler alloys and its device operation (c)–(e) Schematics of crystal structures and atomic-layer stacks of $L2_1$-ordered X_2YZ and Ge along the <111> direction. The solid lines mean the (111) plane for Heusler alloy and Ge.

an ideal candidate for next-generation SC material. Although details will be given later, Ge has good compatibility with Heusler alloys, as shown in figures 44(c) and (d). The basic device structure of the Ge-based vertical-type spin transistors is similar to conventional FETs [205–208]. Source and drain FM electrodes consist of highly spin-polarized FM Heusler alloys and an intermediate Ge layer is composed of a SC Ge. Similar to the spin MOSFET proposed in [192] it is expected that spin transistors show magnetoresistive effect depending on the magnetization configuration between top and bottom FM electrodes in addition to the switching operation by a gate voltage, as shown in figure 44(b). To achieve the vertical-type Ge spin transistor, it is necessary to develop growth techniques of a vertically stacked FM/Ge/FM heterostructure and to observe magnetoresistive effect in Ge-based vertical SV (VSV) devices. Then, after observing gate modulation of drain currents in a vertically stacked FM/Ge/FM structure with a surrounding gate, magnetoresistive effect and the switching operation by a gate voltage must be simultaneously observed [205–208]. Because of the difficulty in fabricating all-epitaxial FM metal/SC/FM metal heterostructures, there have been not many reports demonstrating the fabrication of such heterostructure [194, 209–214]. In particular, only a few research groups can fabricate all-epitaxial FM metal/SC/FM metal heterostructures on a Si platform, which are very important for practical applications [194, 209].

In this section, recent progress in growth techniques of all-epitaxial Heusler alloy/Ge/Heusler alloy heterostructures on a Si platform and in observations of magnetoresistive effect in all-epitaxial Ge-based VSV devices is reviewed. First, crystal growth techniques of epitaxial Ge layers on a FM Heusler alloy are presented. Then, representative results of RT nonvolatile memory effect in Ge-based VSV devices with a Heusler alloy electrode are described. Finally, recent studies on all-epitaxial Co-based Heusler alloy/Ge/Co-based Heusler alloy heterostructures are presented. Future outlook on a vertical-type Ge-based spin transistor based on FM Heusler alloy electrodes is also presented.

4.2. Growth of single-crystalline Ge films on a FM Heusler compound

The concept of the formation of the vertically stacked Heusler alloy/Ge/Heusler alloy heterostructures is explained as follows. The crystal structure of Heusler alloys, X_2YZ, is different from that of Ge, as shown in figures 44(c) and (d). When the X and Y are the same element, it is called as a $D0_3$-ordered structure. The lattice mismatch between ideally ordered full-Heusler alloys such as Fe_3Si, Co_2MnSi, and $Co_2Fe(Al,Si)$ and Ge is less than 1% [193, 194]. Here it is found that there is a good atomic-arrangement matching at the (111) plane, as shown in the triangles of figures 44(c) and (d). For example, an $L2_1$-ordered X_2YZ has a periodic stacking structure consisting of two X, one Y, and one Z layers

along the <111> direction, as shown in figure 44(e). In this special condition, low-temperature epitaxial growth of some FM Heusler alloys on Ge(111) or Si(111) substrates has been explored by MBE [193, 194]. Basically, Knudsen cells have been used even for the Si evaporation to perform finely controlled supply of each element during the growth. In order to form highly ordered structures, atomic compositions for the Heusler alloy films were precisely adjusted [196, 215–221].

To realize two-dimensional epitaxial growth of Ge layers on a FM Heusler alloy, one of the binary Heusler alloys, Fe_3Si [222–224], has been used. The reasons are as follows. First, high-quality single-crystalline Fe_3Si films were obtained on Ge(111) [215, 216] or Si(111) substrates, indicating good compatibility with the Si technologies. Second, the crystal growth mechanism of epitaxial Fe_3Si films on Ge(111) has been well understood [215, 216]. Since the formed Fe_3Si/Ge(111) heterointerface is atomically flat, the surface of the grown Fe_3Si layer is also atomically smooth, leading to a favorable conditions for the epitaxial growth of Ge films. Using the surface of the Fe_3Si/Ge(111) heterostructure, epitaxial growth of Ge layers is explored by MBE [225, 226]. *In-situ* reflection high energy electron diffraction (RHEED) patterns of the Fe_3Si layers clearly exhibited symmetrical streaks, indicating good two-dimensional epitaxial growth (figure 45(g)). On top of the Fe_3Si surface, Ge layers are grown on the top of the Fe_3Si with rising the growth temperature from 200 to 400 °C [225, 226]. The RHEED pattern during the growth shows weakly spotty (see arrows in figure 45(d)), indicating that the precise temperature control could not fully prevent the three-dimensional epitaxial growth of Ge layers. From TEM observations, there were many stacking faults in the Ge layer and the surface of the Ge layer was rough [226]. The rough Ge surface prevents good two-dimensional epitaxial growth of a top-Fe_3Si layer (figure 45(a)).

To realize two-dimensional epitaxial growth of Ge layers on Fe_3Si, a new concept with an artificially controlled arrangement of the surface atoms on Fe_3Si was proposed [225]. Although the $D0_3$-ordered structure should have an Fe or a Si atomic layer on top of Fe_3Si(111), the actual top atomic layer of the grown Fe_3Si layer consists of the mixed layer with Fe and Si atoms as shown in the upper left figure of figure 45(j) because of some structural disorder [215, 216]. Since there is a Si atomic layer in the $D0_3$-ordered structure Fe_3Si at the (111) plane, a Si(111) atomic layer is artificially formed on the disordered surface of the grown Fe_3Si(111) by precisely controlling the evaporation of Si atoms, as shown in the upper center figure in figure 45(j). Even though the surface of the Fe_3Si layers is terminated with a few Si atomic layers, the RHEED pattern can still show streaks (figure 45(h)). It is noted that there is almost no difference in the RHEED patterns between disordered and Si-terminated surfaces. Using the Si-terminated surface, Ge layers are grown on Fe_3Si. Interestingly, two-dimensional epitaxial growth of the Ge layer is demonstrated (figure 45(e)) even in the same growth temperature condition. To confirm the effect of the Si termination, the growth for the Fe-terminated surface is also investigated, where the surface of the Fe_3Si layers is terminated with a few Fe atomic layers as shown in the upper right figure in figure 45(j). Although the Fe-terminated surface is also atomically flat (figure 45(i)), two-dimensional epitaxial growth of Ge layers cannot be demonstrated (see arrows in figure 45(f)). Therefore, it is concluded that the Si termination of the disordered Fe_3Si layers is very important to obtain the high-quality Ge layers on Fe_3Si(111) [225]. Reflecting the surface flatness of the Ge layers, two-dimensional growth of top-Fe_3Si layers is realized only for Si-terminated sample (figures 45(a)–(c)).

Figures 45(k) and (l) show cross-sectional TEM images of Fe_3Si/Ge/Fe_3Si/Ge(111) heterostructures for the Si-terminated sample and Fe-terminated Fe_3Si one, respectively. For the Si-terminated sample, uniform heterostructure is obtained over the observed area and the lattice images of the Ge layer are very clear. Also, the nanobeam electron diffraction (NED) patterns of the Ge layer were almost equivalent to that of the Ge substrate. Furthermore, from the NED patterns of the top- and bottom-Fe_3Si layers, the presence of $D0_3$-ordered structure was confirmed. For the Fe-terminated sample, in contrast, there are lots of stacking faults in the Ge layer (see blue arrows). Observing the region near the Ge/Fe_3Si interface, the presence of amorphous phases in the Ge layer (see the areas marked by blue dashed lines) can be seen. The stacking faults in the Ge layer occur at the position near the amorphous phases. Note that even though the growth temperature of Ge is the same between the Si-terminated sample and Fe-terminated one, there are clear differences in the crystal quality of the Ge layer. It is speculated that, compared to the Fe-terminated surface, the Si-terminated one can reduce the crystallization temperature of Ge and/or enhances the surface migration of Ge on the Fe_3Si(111), which is caused by the difference in the bonding energy between the Ge-Si bond and Ge-Fe bond. From these results, the Si-terminated surface on the Fe_3Si(111) is quite effective to realize the low-temperature two-dimensional epitaxial growth of Ge. Because the surface of the Ge layer for the Fe-terminated sample is largely rough, the surface of the top-Fe_3Si layer was also largely rough. Reflecting the large surface roughness of the Ge layer, the presence of $D0_3$-ordered structure in the top-Fe_3Si layer could not be confirmed. That is, it

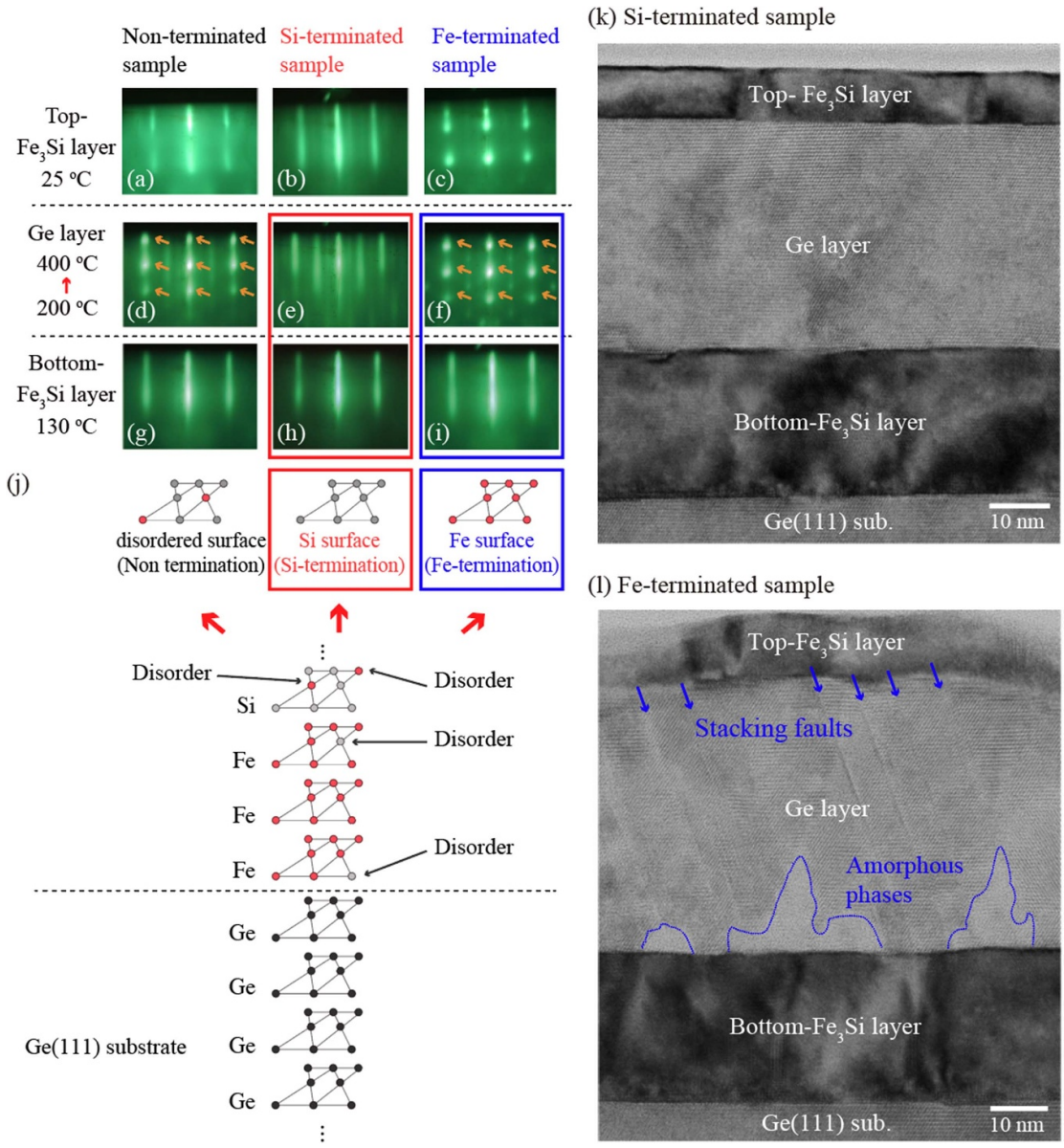


Figure 45. (a)–(j) Schematic diagrams of the atomic arrangements of as-grown Fe_3Si layers on Ge(111) (lower) and RHEED patterns for the top-Fe_3Si layers, the grown Ge layers, and the bottom-Fe_3Si layers for various surfaces of the bottom-Fe_3Si layers, observed along [221] azimuth. Cross-sectional TEM images of Fe_3Si/Ge/Fe_3Si heterostructures on Ge(111) substrates for the (k) Si-terminated and (l) Fe-terminated samples.

was revealed the crystal quality and the surface flatness of the Ge layer also influence of the crystal quality of the top-Fe_3Si layer. Since the Si-termination growth technique could also be used for the growth of Ge on Fe_3Si/Si(111) [227], all-epitaxial Fe_3Si/Ge/Fe_3Si trilayer structures, a basic structure of a Ge-based vertical magnetoresistive device, could be obtained on Ge(111) and Si(111).

In subsequent studies, however, it was revealed that when all-epitaxial Fe_3Si/Ge/Fe_3Si trilayers were formed only by MBE, the diffusion of Ge into the top-Fe_3Si layer could not be sufficiently suppressed [228]. To overcome this problem, CoFe has been used as a top FM layer [229–233]. As another factor for the degradation of the magnetization reversal processes, the elevation of the growth temperature during the initial growth of Ge from 200 to 400 ˚C could also induce the interfacial reaction and/or atomic interdiffusion [225, 226]. Although surfactant-mediated epitaxy [213, 234] or solid phase epitaxy (SPE) [211] was effective for demonstrating two-dimensional epitaxial growth of Ge even on FM materials, the thickness of the Ge layer was limited to less than 10 nm [211, 213, 234], resulting in some limitations for designing device structures. In [230], low-temperature growth technique of epitaxial Ge layers on Fe_3Si by combining SPE and MBE was developed. By introducing a few-nm-thick SPE-grown Ge layer between MBE-grown Ge and Fe_3Si, two-dimensional epitaxial growth of Ge layers was achieved by MBE

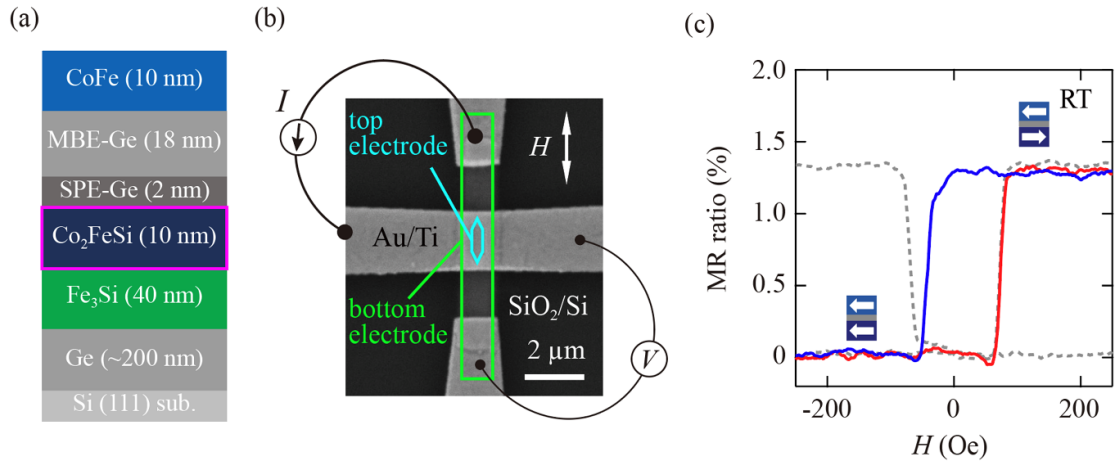


Figure 46. (a) Schematic of a CoFe/undoped *p*-Ge/Co_2FeSi/Fe_3Si heterostructure grown on Ge/Si(111). (b) High-magnification scanning electron micrograph image (top view) of the fabricated CoFe/undoped *p*-Ge/Co_2FeSi/Fe_3Si vertical spin-valve device. (c) Magnetoresistance major hysteresis (gray) and minor (red and blue) loops at room temperature for a representative VSV device. Reprinted from [233], with the permission of AIP Publishing.

even at a growth temperature of ∼175 °C. Thanks to the development of the low-temperature growth technique of Ge, all-epitaxial CoFe/undoped *p*-Ge/Fe_3Si layers with a reasonable magnetization reversal process was demonstrated. After that, low-temperature growth of antimony (Sb)-doped *n*-type Ge layer on Fe_3Si/Si(111) was also achieved [231]. Utilizing these studies [231], low-temperature growth of Ge-*pn* junctions between FM alloys, CoFe and Fe_3Si, on Si(111) was studied [232]. Current-voltage characteristics of the vertical CoFe/undoped *p*-Ge/Sb-doped *n*-Ge/Fe_3Si devices showed evident rectifying behavior, indicating *pn* diode, even at RT. However, at the time of this study, spin transport in the CoFe/Ge-pn junction/Fe_3Si devices could not be observed because of the following two critical issues. First, the thickness of the Ge-*pn* junction (*p*-Ge: ∼50 nm, *n*-Ge: ∼50 nm) had to be reduced because the spin diffusion length of *p*-Ge is very small (∼8.4 nm [235]). Second, the large impact of the spin-orbit interaction from the dopant species should be considered. After it was experimentally revealed that the RT spin diffusion length of P-doped *n*-Ge (440 nm [236]) is larger than that of Sb-doped *n*-Ge (150–290 nm [231]), low-temperature growth of phosphorus (P)-doped *n*-Ge in Ge-based VSV device structures has been explored [237].

4.3. VSV devices with a Co_2FeSi electrode

According to the standard models [2, 202], the two-terminal MR ratio in FM/SC/FM structures depends on the interface spin polarization at the FM/SC contacts, therefore, the performance of other highly spin-polarized FM materials in all-epitaxial Ge-based VSV device structures should be explored. Although all-epitaxial Co_2FeSi/Ge/Co_2FeSi structures on Ge have already been explored [234], and the RT spin polarization of Co_2FeSi (0.5–0.8) is higher than that of Fe_3Si (0.2) [238], the MR effect and its clear enhancement at RT have not yet been observed in VSV structures on Si. As a first step for all-epitaxial Ge-based VSV devices based on Co-based Heusler alloy electrodes, a Co_2FeSi layer was used as a bottom FM electrode in Ge-based VSV devices (figure 46(a)) [233]. The detailed growth procedure of the CoFe/Ge/Co_2FeSi/Fe_3Si structures on Ge/Si(111) was explained in [233]. Here the Fe_3Si layer was utilized as a buffer layer to obtain a smooth surface of the Co_2FeSi layer and the Ge/Si(111) substrates were used as a growth substrate because of the small lattice mismatch between Fe_3Si and Ge. As a result, a 10 nm-thick Co_2FeSi layer could be grown on Fe_3Si with a smooth surface. From *in situ* RHEED observations, an all-epitaxial CoFe/Ge/Co_2FeSi/Fe_3Si structure was successfully formed on the Si platform.

To characterize the electrical properties, the grown CoFe/undoped *p*-Ge/Co_2FeSi/Fe_3Si layer was patterned into VSV devices by conventional electron-beam lithography and Ar ion milling [233]. Figure 46(b) shows top-view scanning electron microscopy (SEM) images of a representative device. To achieve an antiparallel magnetization state between the top CoFe and bottom Co_2FeSi/Fe_3Si under MR measurements, a large shape anisotropy was intentionally applied to the top CoFe layer, where the CoFe layer was designed with a pointed end (cyan), as depicted in figure 46(b). On the other hand, the bottom Co_2FeSi/Fe_3Si bilayer was fabricated with a simple rectangular shape (green). The junction size of

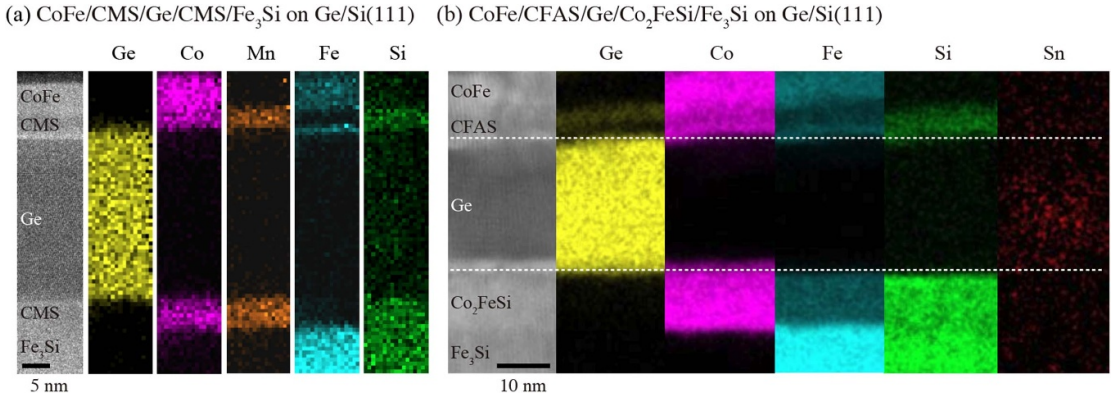


Figure 47. Cross-sectional HAADF-STEM images and EDX elemental maps for (a) CoFe/CMS/Ge/CMS/Fe_3Si on Ge/Si(111) [239, 246]and (b) CoFe/CFAS/Sn-doped Ge/Co_2FeSi/Fe_3Si on Ge/Si(111) [246]. Reprinted from [239], Copyright (2024), with permission from Elsevier. Reproduced from [246]. CC BY 4.0.

the CoFe/undoped *p*-Ge/Co_2FeSi was roughly estimated to be less than 0.7 μm^2 from the SEM observations. The Au/Ti bonding pad for the top CoFe layer was isolated from the bottom Co_2FeSi/Fe_3Si layer and Si substrate by a 100-nm-thick SiO_2 layer. Thus, each Au/Ti bonding pad was connected only to the top CoFe layer and the bottom Fe_3Si buffer layer. As a result, the fabricated VSV devices are conventional CPP-type devices.

For these VSV devices, the two-terminal MR effects are measured by applying in-plane external magnetic fields (H) along the long axis of the wire-shaped FM electrode, as depicted in figure 46(b). Figure 46(c) shows representative MR curves (gray) and minor loops (red and blue) at RT. Clear minor loops with abrupt magnetization switching between parallel and antiparallel states can be seen. The average MR ratio at RT is ∼1.4%, one order of magnitude larger than those observed for the CoFe/undoped *p*-Ge/Fe_3Si VSV devices reported in [229]. Although it is difficult to quantitatively estimate the spin polarization of Co_2FeSi because of lack of parameters in the VSV devices, it has been inferred that the large enhancement of the MR ratio for the CoFe/undoped *p*-Ge/Co_2FeSi VSV devices is due to the increase in the interface spin polarization resulting from Co_2FeSi, as previously discussed in [238].

4.4. All-epitaxial Co_2YZ/Ge/Co_2YZ VSV structure on a Si platform

To improve the performance of Ge-based VSV devices, vertically stacked FM/Ge/FM structures based on half-metallic Co_2YZ electrodes have been explored. In [234], the growth temperature of the intermediate Ge layer can be reduced by utilizing the surfactant effect of Sn during Ge growth. However, some issues were encountered including the interfacial reaction between the Co_2FeSi and Ge layers. To overcome these issues, some approaches have been currently explored. One is the use of another Heusler alloy, Co_2MnSi (CMS [237, 239] and $Co_2FeAl_{0.5}Si_{0.5}$ (CFAS), instead of Co_2FeSi [233, 240] where both CMS and CFAS are well known as highly spin polarized materials [63] and can be utilized for MTJs [33, 45, 51, 241], CPP-GMR [132, 133], SC-based LSV devices [242–244], and oxide-based structures [245]. Another is the further reduction in the growth temperature of Ge less than 200 °C by adding Tin (Sn) during the Ge growth [240]. In this subsection, recent studies for obtaining the vertically stacked Co_2YZ/Ge/Co_2YZ heterostructures are presented [237, 239, 246].

The detailed procedures for the growth of all-epitaxial CMS/Ge/CMS heterostructures and CFAS/Ge/Co_2FeSi ones were described in [240] and [246], respectively. For each sample, the CoFe layer was grown on the top Heusler alloy layer to make the difference in the magnetization switching fields between the top and bottom Heusler alloy layers. Figure 47(a) shows a cross-sectional bright-field-STEM image and EDX elemental mappings for the CoFe/CMS/Ge/CMS/Fe_3Si structure on Ge/Si(111). From the EDX elemental mappings, the CoFe, top-CMS, Ge, and bottom-CMS layers are clearly separated, and Co, Mn and Si atoms are detected in the range of ∼3 nm above the Ge intermediate layer as well as the range of ∼5 nm below the intermediate Ge layer. It is indicated that the atomic interdiffusion between the top-CMS, the intermediate Ge and the bottom-CMS layers is nearly suppressed at the interface by combining SPE, low-temperature MBE, and the Fe atomic layer termination technique [230, 242]. From these results, it is concluded that an all-epitaxial CMS/Ge/CMS VSV structure is demonstrated.

Cross-sectional high-resolution HAADF-STEM images and EDX elemental maps of the CoFe/CFAS/Ge/Co_2FeSi/Fe_3Si structure on Ge/Si(111) are displayed in figure 47(b). For this heterostructure, to reduce the growth temperature of Ge without surface segregation of Sn during the growth, Sn

doping was performed only at the initial stage of Ge growth [246]. In the left HAADF-STEM image, the Ge layer is epitaxially grown on CFS, and the top CoFe/CFAS layer is also epitaxially grown on Ge. The EDX elemental maps show that CoFe, CFAS, Ge, Co_2FeSi, and Fe_3Si layers are separately grown. Notably, the doped Sn was observed predominantly in the intermediate Ge layer. This indicates that the method of Sn doping only at the initial stage of Ge growth is effective. At the bottom interface between Co_2FeSi and Ge, atomic interdiffusion between Co and Ge with several nanometer regions is observed. However, at the top interface between CFAS and Ge, the presence of the Fe termination layer at the CFAS/Ge interface can suppress the diffusion of Co into the Ge layer, and the diffusion of Ge into the CFAS layer cannot be fully suppressed at present. Although the improvement in the quality of the bottom interface between CFS and Ge and the suppression of the diffusion of Ge into the CFAS layer are needed, all epitaxial CFAS/Sn-doped Ge/Co_2FeSi VSV structure has been experimentally demonstrated.

CPP-type SV devices were fabricated to observe spin-dependent transport properties in the all-epitaxial CoFe/CFAS/Ge/Co_2FeSi/Fe_3Si structure. The two-terminal MR ratio was defined as $(\Delta R_S/R_p) \times 100$, where ΔR_S and R_p are the spin accumulation signal ($\Delta V_S/I$) and the resistance between the FM electrodes through the Ge layer in the parallel magnetization state, respectively. $R_p \sim 6.02\ \Omega$ at 10 K and $R_p \sim 6.29\ \Omega$ at 300 K were close to the values obtained in [233]. Hysteresis spin signals depending on the parallel and antiparallel magnetization states between the top CoFe/CFAS and bottom Co_2FeSi/Fe_3Si electrodes are observed, clear evidence of the successful integration of the nonvolatile memory effect into the SC device structures. The values of the spin signal were ∼18 mΩ at 10 K and ∼6.0 mΩ at 300 K, corresponding to the MR values of ∼0.30% at 10 K and ∼0.11% at 300 K, respectively. Although Co-based Heusler alloy electrodes were utilized in the VSV devices, the value at 300 K was relatively small compared to that in [233] (∼1.4%, figure 46(c)). One possible cause is the atomic interdiffusion between Co and Ge in the bottom electrode. The spin polarization of the interface region at the bottom interface was probably lower than expected. In addition, it is considered that the formation of the disordered CFAS(Ge) affects the degradation of the spin polarization of the top FM layer. To enhance the MR ratio at RT, one should further develop methods for suppressing atomic interdiffusion at the top and bottom Co-based Heusler alloy electrodes.

Finally, future outlook on this research field is presented. From the viewpoint of low electric power switching characteristics, tunnel FETs (TFETs), where TFETs leverage a band-to-band tunneling (BTBT) injection of carriers as the primary transport of carriers, have been studied [195, 205–208, 247–249]. Quite recently, RT spin transport through BTBT using Ge-based lateral SV devices based on CFAS/Ge-*pn* junction electrodes was reported [250]. This implies the possibility of RT spin transport could also be emerged even in vertical device structures. For future work, it is important to study spin transport in both *p*-Ge and *n*-Ge in VSV devices based on Co_2YZ electrodes and develop low-temperature gate fabrication technologies.

Acknowledgment

This work was supported in part by MEXT Initiative to Establish Next-generation Novel Integrated Circuits Centers (X-NICS) Grant No. JPJ011438, MEXT Program: Data Creation and Utilization-Type Material Research and Development Project (Digital Transformation Initiative Center for Magnetic Materials; Grant No. JPMXP1122715503), and JST CREST (Grant No. JPMJCR21O1) to YS; JSPS-KAKENHI (Grant No. JP25K01266), Iketani Science and Technology Foundation (Grant No. J251103105), and Masuyakinen Basic Research Foundation (Grant No. J251103109) to SY; JSPS-KAKENHI (Grant Nos. 21K20434 and 23K03934) and Advanced Storage Research Consortium (ASRC) to HS; JSPS-KAKENHI (Grant Nos. JP21H05000, JP24H00034 and JP25K24637), MEXT X-NICS (Grant No. JPJ011438), JST-ASPIRE (Grant No. JPMJAP2413), JST-CREST (Grant No. JPMJCR18J1), and Spintronics Research Network of Japan (Spin-RNJ) to KH. SY and KH acknowledge Prof. K. Sawano, Prof. M. Yamada, and Prof. V. K. Lazarov for useful discussions and experimental support.

Data availability statement

No new data were created or analysed in this study.

Author contributions

Yuya Sakuraba 0000-0003-4618-9550
Conceptualization (equal), Supervision (lead), Writing – original draft (lead), Writing – review & editing (lead)

Shinya Yamada 0000-0001-6340-9151
Writing – original draft (equal), Writing – review & editing (equal)

Hirofumi Suto 0000-0003-4387-5862
Writing – original draft (equal), Writing – review & editing (equal)

Tomoya Nakatani 0000-0001-9590-216X
Writing – original draft (equal), Writing – review & editing (equal)

Kohei Hamaya 0000-0002-5473-6086
Visualization (equal), Writing – review & editing (supporting)

References

[1] Julliere M 1975 Tunneling between ferromagnetic films *Phys. Lett. A* **54** 225–6
[2] Valet T and Fert A 1993 Theory of the perpendicular magnetoresistance in magnetic multilayers *Phys. Rev. B* **48** 7099
[3] Slonczewski J C 1996 Current-driven excitation of magnetic multilayers *J. Magn. Magn. Mater.* **159** L1–7
[4] Schmidt G, Ferrand D, Molenkamp L W, Filip A T and van Wees B J 2000 Fundamental obstacle for electrical spin injection from a ferromagnetic metal into a diffusive semiconductor *Phys. Rev. B* **62** R4790–3
[5] Kamberský V 1976 On ferromagnetic resonance damping in metals *Czechoslovak J. Phys. B* **26** 1366–83
[6] de Groot R A, Mueller F M, van Engen P G and Buschow K H J 1983 New Class of Materials: Half-Metallic Ferromagnets *Phys. Rev. Lett.* **50** 2024–7
[7] Baibich M N, Broto J M, Fert A, Van Dau F N, Petroff F, Etienne P, Creuzet G, Friederich A and Chazelas J 1988 Giant magnetoresistance of (001)Fe/(001)Cr magnetic superlattices *Phys. Rev. Lett.* **61** 2472–5
[8] Binasch G, Grünberg P, Saurenbach F and Zinn W 1989 Enhanced magnetoresistance in layered magnetic structures with antiferromagnetic interlayer exchange *Phys. Rev. B* **39** 4828–30
[9] Schwarz K 1986 CrO_2 predicted as a half-metallic ferromagnet *J. Phys. F* **16** L211–2L215
[10] Pickett W and Singh D 1996 Electronic structure and half-metallic transport in the $La_{1-x}Ca_xMnO_3$ system *Phys. Rev. B* **53** 1146–60
[11] Zhang Z and Satpathy S 1991 Electron states, magnetism, and the Verwey transition in magnetite *Phys. Rev. B* **44** 13319–31
[12] Ishida S, Fujii S, Kashiwagi S and Asano S 1995 Search for half-metallic compounds in Co_2MnZ (Z=IIIb, IVb, Vb element) *J. Phys. Soc. Japan* **64** 2152–7
[13] Soulen R J *et al* 1998 Measuring the spin polarization of a metal with a superconducting point contact *Science* **282** 85–88
[14] Bowen M, Bibes M, Barthélémy A, Contour J P, Anane A, Lemaître Y and Fert A 2003 Nearly total spin polarization in $La_{2/3}Sr_{1/3}MnO_3$ from tunneling experiments *Appl. Phys. Lett.* **82** 233–5
[15] Galanakis I, Dederichs P H and Papanikolaou N 2002 Slater-Pauling behavior and origin of the half-metallicity of the full-Heusler alloys *Phys. Rev. B* **66** 174429
[16] Picozzi S, Continenza A and Freeman A J 2004 Role of structural defects on the half-metallic character of Co_2MnGe and Co_2MnSi Heusler alloys *Phys. Rev. B* **69** 094423
[17] Miura Y, Nagao K and Shirai M 2004 Atomic disorder effects on half-metallicity of the full-Heusler alloys $Co_2(Cr_{1-x}Fe_x)Al$: a first-principles study *Phys. Rev. B* **69** 144413
[18] Elphick K, Frost W, Samiepour M, Kubota T, Takanashi K, Sukegawa H, Mitani S and Hirohata A 2021 Heusler alloys for spintronic devices: review on recent development and future perspectives *Sci. Technol. Adv. Mater.* **22** 235–71
[19] Butler W H, Zhang X-G, Schulthess T C and MacLaren J M 2001 Spin-dependent tunneling conductance of Fe/MgO/Fe sandwiches *Phys. Rev. B* **63** 054416
[20] Mathon J and Umerski A 2001 Theory of tunneling magnetoresistance of an epitaxial Fe/MgO/Fe(001) junction *Phys. Rev. B* **63** 220403
[21] Yuasa S, Nagahama T, Fukushima A, Suzuki Y and Ando K 2004 Giant room-temperature magnetoresistance in single-crystal Fe/MgO/Fe magnetic tunnel junctions *Nat. Mater.* **3** 868–71
[22] Parkin S S P, Kaiser C, Panchula A, Rice P M, Hughes B, Samant M and Yang S H 2004 Giant tunnelling magnetoresistance at room temperature with MgO (100) tunnel barriers *Nat. Mater.* **3** 862–7
[23] Balke B, Fecher G H, Winterlik J and Felser C 2007 Mn_3Ga, a compensated ferrimagnet with high Curie temperature and low magnetic moment for spin torque transfer applications *Appl. Phys. Lett.* **90** 152504
[24] Tanaka C T, Nowak J and Moodera J S 1997 Magnetoresistance in ferromagnet-insulator-ferromagnet tunnel junctions with half-metallic ferromagnet NiMnSb compound *J. Appl. Phys.* **81** 5515–7
[25] Liu J, Girgis E, Bach P, Rüster C, Gould C, Schmidt G and Molenkamp L W 2006 Tunneling magnetoresistance in devices based on epitaxial NiMnSb with uniaxial anisotropy *J. Appl. Phys.* **99** 036110
[26] Inomata K, Okamura S, Goto R and Tezuka N 2003 Large tunneling magnetoresistance at room temperature using a Heusler alloy with the B2 structure *Japan. J. Appl. Phys. 2* **42** 419–22
[27] Rata A D, Braak H, Burgler D E and Schneider C M 2007 Large inverse tunneling magnetoresistance in $Co_2Cr_{0.6}Fe_{0.4}Al$/MgO/$Co_{80}Fe_{20}$ magnetic tunnel junctions *Appl. Phys. Lett.* **90** 162512–3
[28] Marukame T, Ishikawa T, Hakamata S, Matsuda K, Uemura T and Yamamoto M 2007 Highly spin-polarized tunneling in fully epitaxial $Co_2Cr_{0.6}Fe_{0.4}Al$/MgO/$Co_{50}Fe_{50}$ magnetic tunnel junctions with exchange biasing *Appl. Phys. Lett.* **90** 012508

[29] Oogane M, Nakata J, Kubota H, Ando Y, Sakuma A and Miyazaki T 2005 Temperature dependence of tunnel magnetoresistance in Co–Mn–Al/Al–oxide/Co–Fe junctions *Jpn. J. Appl. Phys.* **44** L760
[30] Sakuraba Y, Nakata J, Oogane M, Ando Y, Kato H, Sakuma A, Miyazaki T and Kubota H 2006 Magnetic tunnel junctions using B2-ordered Co_2MnAl Heusler alloy epitaxial electrode *Appl. Phys. Lett.* **88** 022503
[31] Schmalhorst J, Kämmerer S, Sacher M, Reiss G, Hütten A and Scholl A 2004 Interface structure and magnetism of magnetic tunnel junctions with a Co_2MnSi electrode *Phys. Rev. B* **70** 024426
[32] Sakuraba Y, Nakata J, Oogane M, Kubota H, Ando Y, Sakuma A and Miyazaki T 2005 Huge spin-polarization of $L2_1$-ordered Co_2MnSi epitaxial Heusler alloy film *Jpn. J. Appl. Phys.* **44** L1100–2
[33] Sakuraba Y, Hattori M, Oogane M, Ando Y, Kato H, Sakuma A, Miyazaki T and Kubota H 2006 Giant tunneling magnetoresistance in Co_2MnSi/Al–O/Co_2MnSi magnetic tunnel junctions *Appl. Phys. Lett.* **88** 192508
[34] Hattori M, Sakuraba Y, Oogane M, Ando Y and Miyazaki T 2008 Tunnel magnetoresistance effect in magnetic tunnel junctions using a $Co_2MnSi(110)$ electrode *Appl. Phys. Express* **1** 021301
[35] Tsunegi S, Sakuraba Y, Oogane M, Takanashi K and Ando Y 2008 Large tunnel magnetoresistance in magnetic tunnel junctions using a Co_2MnSi Heusler alloy electrode and a MgO barrier *Appl. Phys. Lett.* **93** 112506
[36] Tsunegi S, Sakuraba Y, Oogane M, Naganuma H, Takanashi K and Ando Y 2009 Enhancement in tunnel magnetoresistance effect by inserting CoFeB to the tunneling barrier interface in Co_2MnSi/MgO/CoFe magnetic tunnel junctions *Appl. Phys. Lett.* **94** 252503
[37] Ishikawa T, Liu H, Taira T, Matsuda K, Uemura T and Yamamoto M 2009 Influence of film composition in Co_2MnSi electrodes on tunnel magnetoresistance characteristics of Co_2MnSi/MgO/Co_2MnSi magnetic tunnel junctions *Appl. Phys. Lett.* **95** 232512–3
[38] Liu H, Honda Y, Taira T, Matsuda K, Arita M, Uemura T and Yamamoto M 2012 Giant tunneling magnetoresistance in epitaxial Co_2MnSi/MgO/Co_2MnSi magnetic tunnel junctions by half-metallicity of Co_2MnSi and coherent tunneling *Appl. Phys. Lett.* **101** 132418
[39] Kubota T, Tsunegi S, Oogane M, Mizukami S, Miyazaki T, Naganuma H and Ando Y 2009 Half-metallicity and Gilbert damping constant in $Co_2Fe_xMn_{1-x}Si$ Heusler alloys depending on the film composition *Appl. Phys. Lett.* **94** 122504
[40] Liu H, Kawami T, Moges K, Uemura T, Yamamoto M, Shi F and Voyles P M 2015 Influence of film composition in quaternary Heusler alloy $Co_2(Mn,Fe)Si$ thin films on tunnelling magnetoresistance of $Co_2(Mn,Fe)Si$/MgO-based magnetic tunnel junctions *J. Phys. D: Appl. Phys.* **48** 164001
[41] Moges K, Honda Y, Liu H, Uemura T, Yamamoto M, Miura Y and Shirai M 2016 Enhanced half-metallicity of off-stoichiometric quaternary Heusler alloy $Co_2(Mn,Fe)Si$ investigated through saturation magnetization and tunneling magnetoresistance *Phys. Rev. B* **93** 134403
[42] Marukame T, Ishikawa T, Matsuda K, Uemura T and Yamamoto M 2006 Tunnel magnetoresistance in epitaxial magnetic tunnel junctions using full-Heusler alloy Co_2MnGe thin film and MgO tunnel barrier *J. Appl. Phys.* **99** 08A904
[43] Verduijn E A and Westerholt K 2006 Tunneling magnetoresistance of Co_2MnGe/Al_2O_3/Co junctions *J. Appl. Phys.* **99** 084502
[44] Taira T, Ishikawa T, Itabashi N, Matsuda K, Uemura T and Yamamoto M 2009 Spin-dependent tunnelling characteristics of fully epitaxial magnetic tunnel junctions with a Heusler alloy Co_2MnGe thin film and a MgO barrier *J. Phys. D: Appl. Phys.* **42** 084015
[45] Yamamoto M, Ishikawa T, Taira T, Li G, Matsuda K and Uemura T 2010 Effect of defects in Heusler alloy thin films on spin-dependent tunnelling characteristics of Co_2MnSi/MgO/Co_2 MnSi and Co_2MnGe/MgO/Co_2MnGe magnetic tunnel junctions Journal of Physics: Condensed Mattera **22** 164212
[46] Wang W, Sukegawa H, Shan R, Mitani S and Inomata K 2009 Giant tunneling magnetoresistance up to 330% at room temperature in sputter deposited Co_2FeAl/MgO/CoFe magnetic tunnel junctions *Appl. Phys. Lett.* **95** 182502
[47] Scheike T, Sukegawa H, Inomata K, Ohkubo T, Hono K and Mitani S 2016 Chemical ordering and large tunnel magnetoresistance in $Co_2FeAl/MgAl_2O_4/Co_2FeAl(001)$ junctions *Appl. Phys. Express* **9** 053004
[48] Sterwerf C, Meinert M and Schmalhorst J 2013 High TMR ratio in Co_2FeSi and Fe_2CoSi based magnetic tunnel junctions IEEE Transactions on Magnetics **49** 4386–9
[49] Oogane M, Shinano M, Sakuraba Y and Ando Y 2009 Tunnel magnetoresistance effect in magnetic tunnel junctions using epitaxial Co_2FeSi Heusler alloy electrode *J. Appl. Phys.* **105** 07C903
[50] Tezuka N, Ikeda N, Sugimoto S and Inomata K 2007 Giant tunnel magnetoresistance at room temperature for junctions using Full-Heusler $Co_2FeAl_{0.5}$ $Si_{0.5}$ electrodes *Jpn. J. Appl. Phys.* **46** L454
[51] Shan R, Sukegawa H, Wang W H, Kodzuka M, Furubayashi T, Ohkubo T, Mitani S, Inomata K and Hono K 2009 Demonstration of half-metallicity in fermi-level-tuned Heusler alloy $Co_2FeAl_{0.5}Si_{0.5}$ at room temperature *Phys. Rev. Lett.* **102** 246601
[52] Galanakis I, Mavropoulos P and Dederichs P H 2006 Electronic structure and Slater–Pauling behaviour in half-metallic Heusler alloys calculated from first principles *J. Phys. D: Appl. Phys.* **39** 765–75
[53] Zhang M, Liu Z, Hu H, Liu G, Cui Y, Chen J, Wu G, Zhang X and Xiao G 2004 Is Heusler compound Co_2CrAl a half-metallic ferromagnet: electronic band structure, and transport properties *J. Magn. Magn. Mater.* **277** 130–5
[54] Kobayashi K, Kainuma R and Ishida K 2006 Phase separation and stability of $L2_1$-type phase in $Co_2(Cr_{1-x}Fe_x)(Ga_{1-y}Al_y)$ alloys *Mater. Trans.* **47** 20–24
[55] Kübler J, William A R and Sommers C B 1983 Formation and coupling of magnetic moments in Heusler alloys *Phys. Rev. B* **28** 1745–55
[56] Kubota H, Nakata J, Oogane M, Ando Y, Sakuma A and Miyazaki T 2004 Large magnetoresistance in magnetic tunnel junctions using Co-Mn-Al Full Heusler alloy *Jpn. J. Appl. Phys.* **43** L984–6
[57] Sakuraba Y, Nakata J, Oogane M, Kubota H, Ando Y, Sakuma A and Miyazaki T 2005 Fabrication of Co_2MnAl Heusler alloy epitaxial film using Cr buffer layer *Jpn. J. Appl. Phys. 1* **44** 6535–7
[58] Vilanova Vidal E, Stryganyuk G, Schneider H, Felser C and Jakob G 2011 Exploring Co_2MnAl Heusler compound for anomalous Hall effect sensors *Appl. Phys. Lett.* **99** 132509
[59] Kübler J and Felser C 2016 Weyl points in the ferromagnetic Heusler compound Co_2MnAl *EPL* **114** 47005
[60] Li P *et al* 2020 Giant room temperature anomalous Hall effect and tunable topology in a ferromagnetic topological semimetal Co_2MnAl *Nat. Commun.* **11** 3476
[61] Kämmerer S, Thomas A, Hütten A and Reiss G 2004 Co_2MnSi Heusler alloy as magnetic electrodes in magnetic tunnel junctions *Appl. Phys. Lett.* **85** 79–81
[62] Hülsen B, Scheffler M and Kratzer P 2009 Thermodynamics of the Heusler alloy $Co_{2-x}Mn_{1+x}Si$: a combined density functional theory and cluster expansion study *Phys. Rev. B* **79** 094407

[63] Balke B, Fecher G H, Kandpal H C, Felser C, Kobayashi K, Ikenaga E, Kim J-J and Ueda S 2006 Properties of the quaternary half-metal-type Heusler alloy $Co_2Mn_{1-x}Fe_xSi$ *Phys. Rev. B* **74** 104405

[64] Ikeda S, Hayakawa J, Ashizawa Y, Lee Y M, Miura K, Hasegawa H, Tsunoda M, Matsukura F and Ohno H 2008 Tunnel magnetoresistance of 604% at 300 K by suppression of Ta diffusion in CoFeB/MgO/CoFeB pseudo-spin-valves annealed at high temperature *Appl. Phys. Lett.* **93** 082508

[65] Scheike T, Wen Z, Sukegawa H and Mitani S 2023 631% room temperature tunnel magnetoresistance with large oscillation effect in CoFe/MgO/CoFe(001) junctions *Appl. Phys. Lett.* **122** 112404

[66] Li S, Nakatani T, Masuda K, Sakuraba Y, Xu X D, Sasaki T T, Tajiri H, Miura Y, Furubayashi T and Hono K 2018 Enhancement of current-perpendicular-to-plane giant magnetoresistive outputs by improving B2-order in polycrystalline $Co_2(Mn_{0.6}Fe_{0.4})Ge$ Heusler alloy films with the insertion of amorphous CoFeBTa underlayer *Acta Mater.* **142** 49–57

[67] Kushwaha V K, Sakuraba Y, Nakatani T, Sasaki T, Kurniawan I, Miura Y, Tajiri H and Hono K 2022 High. $L2_1$-atomic ordering and spin-polarization in Co_2MnZ (Z = Ge, Sn) Heusler thin films with low-temperature annealing process *APL Mater.* **10** 091119

[68] Nakatani T, Li S, Sakuraba Y, Furubayashi T and Hono K 2018 Advanced CPP-GMR spin-valve sensors for narrow reader applications *IEEE Trans. Magn.* **54** 3300211

[69] Wen Z, Sukegawa H, Mitani S and Inomata K 2011 Perpendicular magnetization of Co_2FeAl full-Heusler alloy films induced by MgO interface *Appl. Phys. Lett.* **98** 2011–4

[70] Wen Z, Hadorn J P, Okabayashi J, Sukegawa H, Ohkubo T, Inomata K, Mitani S and Hono K 2017 Interdiffusion in epitaxial ultrathin Co_2FeAl/MgO heterostructures with interface-induced perpendicular magnetic anisotropy *Appl. Phys. Express* **10** 013003

[71] Wurmehl S, Fecher G H, Kandpal H C, Ksenofontov V, Felser C and Lin H J 2006 Investigation of Co_2FeSi: the Heusler compound with highest Curie temperature and magnetic moment *Appl. Phys. Lett.* **88** 032503

[72] Bombor D, Blum C G F, Volkonskiy O, Rodan S, Wurmehl S, Hess C and Büchner B 2013 Half-metallic ferromagnetism with unexpectedly small spin splitting in the Heusler compound Co_2FeSi *Phys. Rev. Lett.* **110** 066601

[73] Sakuraba Y, Kokado S, Hirayama Y, Furubayashi T, Sukegawa H, Li S, Takahashi Y K and Hono K 2014 Quantitative analysis of anisotropic magnetoresistance in Co_2MnZ and Co_2FeZ epitaxial thin films: a facile way to investigate spin-polarization in half-metallic Heusler compounds *Appl. Phys. Lett.* **104** 172407

[74] Sumida K, Fujita Y, Zhou W, Masuda K, Kawasaki I, Fujimori S, Kimura A and Sakuraba Y 2023 Role of on-site Coulomb interactions in the half-metallic Weyl ferromagnet candidate thin-film Co_2FeSi *Phys. Rev. B* **108** L241101

[75] Zhou W, Masuda K, Sumida K, Fujita Y, Kimura A and Sakuraba Y 2025 Comparative experimental and theoretical study on anomalous Nernst effect of Heusler alloy Co_2FeSi thin film: estimation of on-site Coulomb interaction at Co site *Sci. Technol. Adv. Mater.* **26** 2564061

[76] Fecher G H and Felser C 2007 Substituting the main group element in cobalt–iron based Heusler alloys: $Co_2FeAl_{1-x}Si_x$ *J. Phys. D: Appl. Phys.* **40** 1582–6

[77] Wang W, Sukegawa H, Shan R, Furubayashi T and Inomata K 2008 Preparation and characterization of highly $L2_1$-ordered full-Heusler alloy $Co_2FeAl_{0.5}Si_{0.5}$ thin films for spintronics device applications *Appl. Phys. Lett.* **92** 221912

[78] Chioncel L, Katsnelson M I, de Groot R A and Lichtenstein A I 2003 Nonquasiparticle states in the half-metallic ferromagnet NiMnSb *Phys. Rev. B* **68** 144425

[79] Chioncel L, Sakuraba Y, Arrigoni E, Katsnelson M I, Oogane M, Ando Y, Miyazaki T, Burzo E and Lichtenstein A I 2008 Nonquasiparticle states in Co_2MnSi evidenced through magnetic tunnel junction spectroscopy measurements *Phys. Rev. Lett.* **100** 086402

[80] Miyamoto K *et al* 2009 Absence of temperature dependence of the valence-band spectrum of Co_2MnSi *Phys. Rev. B* **79** 100405

[81] Kurniawan I, Nawa K, Masuda K, Miura Y and Hono K 2021 First-principles disordered local-moment study on temperature dependence of spin polarization in $Co_2Fe(Ga_{0.5}Ge_{0.5})$ Heusler alloy *Acta Mater.* **218** 117218

[82] Seah M P and Dench W A 1979 Quantitative electron spectroscopy of surfaces: a standard data base for electron inelastic mean free paths in solids *Surf. Interface Anal.* **1** 2–11

[83] Jourdan M *et al* 2014 Direct observation of half-metallicity in the Heusler compound Co_2MnSi *Nat. Commun.* **5** 3974

[84] Ueda S and Sakuraba Y 2021 Direct observation of spin-resolved valence band electronic states from a buried magnetic layer with hard x-ray photoemission *Sci. Technol. Adv. Mater.* **22** 317–25

[85] Ueda S, Miura Y, Fujita Y and Sakuraba Y 2022 Direct probing of temperature-independent bulk half-metallicity in Co_2MnSi by spin-resolved hard x-ray photoemission *Phys. Rev. B* **106** 075101

[86] Ikhtiar Kasai S, Takahashi Y K, Furubayashi T, Mitani S and Hono K 2016 Temperature dependence of magneto-transport properties in $Co_2Fe(Ga_{0.5}Ge_{0.5})$/Cu lateral spin valves *Appl. Phys. Lett.* **108** 062401

[87] Kushwaha V K, Kokado S, Kasai S, Miura Y, Nakatani T, Kumara R, Tajiri H, Furubayashi T, Hono K and Sakuraba Y 2022 Prediction of half-metallic gap formation and Fermi level position in Co-based Heusler alloy epitaxial thin films through anisotropic magnetoresistance effect *Phys. Rev. Mater.* **6** 064411

[88] Sakuraba Y, Miyakoshi T, Oogane M, Ando Y, Sakuma A, Miyazaki T and Kubota H 2006 Direct observation of half-metallic energy gap in Co_2MnSi by tunneling conductance spectroscopy *Appl. Phys. Lett.* **89** 23–25

[89] Sakuraba Y, Takanashi K, Kota Y, Kubota T, Oogane M, Sakuma A and Ando Y 2010 Evidence of Fermi level control in a half-metallic Heusler compound Co_2MnSi by Al-doping: comparison of measurements with first-principles calculations *Phys. Rev. B* **81** 144422

[90] Mavropoulos P, Lezaic M and Bluegel S 2005 Half-metallic ferromagnets for magnetic tunnel junctions *Phys. Rev. B* **72** 174428

[91] Sakuma A, Toga Y and Tsuchiura H 2009 Theoretical study on the stability of magnetic structures in the surface and interfaces of Heusler alloys, Co_2MnAl and Co_2MnSi *J. Appl. Phys.* **105** 07C910

[92] Miura Y, Abe K and Shirai M 2011 Effects of interfacial noncollinear magnetic structures on spin-dependent conductance in Co_2MnSi/MgO/Co_2MnSi magnetic tunnel junctions: a first-principles study *Phys. Rev. B* **83** 214411

[93] Tsunegi S, Sakuraba Y, Amemiya K, Sakamaki M, Ozawa E, Sakuma A, Takanashi K and Ando Y 2012 Observation of magnetic moments at the interface region in magnetic tunnel junctions using depth-resolved x-ray magnetic circular dichroism *Phys. Rev. B* **85** 180408

[94] Miura Y, Uchida H, Oba Y, Abe K and Shirai M 2008 Half-metallic interface and coherent tunneling in Co_2YZ/MgO/ Co_2YZ (YZ=MnSi,CrAl) magnetic tunnel junctions: a first-principles study *Phys. Rev. B* **78** 064416

[95] Miura Y, Abe K and Shirai M 2010 Half-metallic behavior of Co_2MnSi/Co_2MnAl/MgO interface and its coherent tunneling conductance *J. Phys.: Conf. Ser.* **200** 052016

[96] Ozawa E, Tsunegi S, Oogane M, Naganuma H and Ando Y 2011 The effect of inserting thin Co_2MnAl layer into the Co_2MnSi/MgO interface on tunnel magnetoresistance effect *J. Phys.: Conf. Ser.* **266** 012104

[97] Bainsla L, Suzuki K Z, Tsujikawa M, Tsuchiura H, Shirai M and Mizukami S 2018 Magnetic tunnel junctions with an equiatomic quaternary CoFeMnSi Heusler alloy electrode *Appl. Phys. Lett.* **112** 052403

[98] Rogge J, Hetaba W, Schmalhorst J, Bouchikhaoui H, Stender P, Baither D, Schmitz G and Hütten A 2015 Co_2FeAl based magnetic tunnel junctions with BaO and MgO/BaO barriers *AIP Adv.* **5** 077173

[99] Wang Y P, Han G C, Lu H, Qiu J, Yap Q J, Ji R and Teo K L 2013 Tunnel magnetoresistance effect and interface study in magnetic tunnel junctions using epitaxial Fe_2CrSi Heusler alloy electrode *J. Appl. Phys.* **114** 013910

[100] Xi R, Feng Y, Zhang K, Yang W, Lu H, Jian A, Han J, Sang S and Gao G 2025 Large tunneling magnetoresistance and perpendicular magnetic anisotropy in magnetic tunneling junction based on spin gapless semiconductor CoFeCrAl *Appl. Phys. Lett.* **127**

[101] Roy T, Tsujikawa M and Shirai M 2023 Ballistic spin-transport properties of magnetic tunnel junctions with MnCr-based ferrimagnetic quaternary Heusler alloys *Phys. Rev. Mater.* **7**

[102] Lalrinkima Kastuar S M, Zadeng L, Zosiamliana R, Chettri B, Singh Y T, Zuala L, Rai D P and Ekuma C E 2023 Giant intrinsic magnetoresistance in spin-filtered tunnel junctions with ferrimagnetic electrode *Phys. Rev. B* **107** 155305

[103] Feng Y, Ding H, Li X, Wu B and Chen H 2022 Spin transport properties of highly lattice-matched all-Heusler-alloy magnetic tunnel junction *J. Appl. Phys.* **131** 133901

[104] Asif Akhtar S P, Prasad S and Islam A 2025 Excellent spin-filtering and giant tunneling magnetoresistance in a van der Waals magnetic tunnel junction based on full-Heusler alloys Co_2FeX (X = Si/Al) and 2D vdW materials WSe_2/MoS_2 *Physica E* **173** 116299

[105] Chand Rachakonda T, Parveen Asif Akhtar S and Islam A 2024 High tunneling magneto-resistance ratio in Co_2FeAl Heusler alloy and WSe_2 2D material tunnel barrier-based magnetic tunnel junctions *J. Magn. Magn. Mater.* **606** 172365

[106] Iwasaki Y, Jaekyun H, Sakuraba Y, Kotsugi M and Igarashi Y 2022 Efficient autonomous material search method combining ab initio calculations, autoencoder, and multi-objective Bayesian optimization *Sci. Technol. Adv. Mater.: Methods* **2** 365–71

[107] Hiratsuka T *et al* 2010 Fabrication of perpendicularly magnetized magnetic tunnel junctions with $L1_0$-CoPt/Co_2MnSi hybrid electrode *J. Appl. Phys.* **107** 09C714

[108] Ikeda S, Miura K, Yamamoto H, Mizunuma K, Gan H D, Endo M, Kanai S, Hayakawa J, Matsukura F and Ohno H 2010 A perpendicular-anisotropy CoFeB-MgO magnetic tunnel junction *Nat. Mater.* **9** 721–4

[109] Watanabe K, Jinnai B, Fukami S, Sato H and Ohno H 2018 Shape anisotropy revisited in single-digit nanometer magnetic tunnel junctions *Nat. Commun.* **9** 663

[110] Taniguchi, Yujiro & Miura, Yoshio & Abe, Kazutaka & Shirai and Masafumi 2008 Theoretical Studies on Spin-Dependent Conductance in FePt/MgO/FePt(001) Magnetic Tunnel Junctions. Magnetics, IEEE Transactions on **44** 2585–8

[111] Kim G, Sakuraba Y, Oogane M, Ando Y and Miyazaki T 2008 Tunneling magnetoresistance of magnetic tunnel junctions using perpendicular magnetization L10-CoPt electrodes *Appl. Phys. Lett.* **92** 172502–3

[112] Yoshikawa M, Kitagawa E, Nagase T, Daibou T, Nagamine M, Nishiyama K, Kishi T and Yoda H 2008 Tunnel magnetoresistance Over 100% in MgO-based magnetic tunnel junction films with perpendicular magnetic $L1_0$-FePt electrodes *IEEE Trans. Magn.* **44** 2573–6

[113] Mizukami S, Kubota T, Wu F, Zhang X, Miyazaki T, Naganuma H, Oogane M, Sakuma A and Ando Y 2012 Composition dependence of magnetic properties in perpendicularly magnetized epitaxial thin films of Mn-Ga alloys *Phys. Rev. B* **85** 014416

[114] Mizukami S *et al* 2011 Long-lived ultrafast spin precession in manganese alloys films with a large perpendicular magnetic anisotropy *Phys. Rev. Lett.* **106** 117201

[115] Miura Y and Shirai M 2014 Theoretical study on tunneling magnetoresistance of magnetic tunnel Tunctions with $D0_{22}$-Mn_3Z(Z= Ga, Ge) *IEEE Trans. Magn.* **50** 1400504

[116] Kubota T *et al* 2011 Magnetoresistance effect in tunnel junctions with perpendicularly magnetized. $D0_{22}$-$Mn_{3-\delta}Ga$ electrode and MgO barrier *Appl. Phys. Express* **4** 043002

[117] Kubota T, Ma Q, Mizukami S, Zhang X, Naganuma H, Oogane M, Ando Y and Miyazaki T 2012 Dependence of tunnel magnetoresistance effect on Fe thickness of perpendicularly magnetized $L1_0$-$Mn_{62}Ga_{38}$/Fe/MgO/CoFe junctions *Appl. Phys. Express* **5** 043003

[118] Sugihara A, Suzuki K, Miyazaki T and Mizukami S 2015 Tunnel magnetoresistance in full-epitaxial magnetic tunnel junctions with a top electrode consisting of a perpendicularly magnetized $D0_{22}$-Mn_3Ge film *Jpn. J. Appl. Phys.* **54** 078002

[119] Suzuki K Z, Miura Y, Ranjbar R, Bainsla L, Ono A, Sasaki Y and Mizukami S 2018 Perpendicular magnetic tunnel junctions with Mn-modified ultrathin MnGa layer *Appl. Phys. Lett.* **112** 062402

[120] Suzuki K Z, Ichinose T, Iihama S, Monma R and Mizukami S 2021 Enhanced tunnel magnetoresistance in Mn-based perpendicular magnetic tunnel junctions utilizing antiferromagnetically coupled bcc-Co-based interlayer *Appl. Phys. Lett.* **118** 172412

[121] Suzuki K Z and Mizukami S 2023 Tunnel magnetoresistance exceeding 100% in magnetic tunnel junctions using Mn-based tetragonal alloy electrodes with perpendicular magnetic anisotropy *AIP Adv.* **13** 035225

[122] Filippou P, Jeong J, Ferrante Y, Yang S-H, Topuria T, Samant M G and Parkin S S P 2018 Chiral domain wall motion in unit-cell thick perpendicularly magnetized Heusler films prepared by chemical templating *Nat. Commun.* **9** 4653

[123] Garg C *et al* 2025 Ferrimagnetic Heusler tunnel junctions with fast spin-transfer torque switching enabled by low magnetization *Nat. Nanotechnol.* **20** 360–5

[124] Faleev S V, Ferrante Y, Jeong J, Samant M G, Jones B and Parkin S S P 2017 Heusler compounds with perpendicular magnetic anisotropy and large tunneling magnetoresistance *Phys. Rev. Mater.* **1** 024402

[125] Yamada S *et al* 2019 Experimental verification of the origin of positive linear magnetoresistance in $CoFe(V_{1-x}Mn_x)Si$ Heusler alloys *Phys. Rev. B* **100** 195137

[126] Yakushiji K, Saito K, Mitani S, Takanashi K, Takahashi Y K and Hono K 2006 Current-perpendicular-to-plane magnetoresistance in epitaxial Co_2MnSi/Cr/Co_2MnSi trilayers *Appl. Phys. Lett.* **88** 222504

[127] Kodama K, Furubayashi T, Sukegawa H, Nakatani T M, Inomata K and Hono K 2009 Current-perpendicular-to-plane giant magnetoresistance of a spin valve using Co_2MnSi Heusler alloy electrodes *J. Appl. Phys.* **105** 07E905

[128] Furubayashi T, Kodama K, Nakatani T M, Sukegawa H, Takahashi Y K, Inomata K and Hono K 2010 Structure and transport properties of current-perpendicular-to-plane spin valves using $Co_2FeAl_{0.5}Si_{0.5}$ and Co_2MnSi Heusler alloy electrodes *J. Appl. Phys.* **107** 113917

[129] Furubayashi T, Kodama K, Sukegawa H, Takahashi Y K, Inomata K and Hono K 2008 Current-perpendicular-to-plane giant magnetoresistance in spin-valve structures using epitaxial $Co_2FeAl_{0.5}Si_{0.5}$/Ag/$Co_2FeAl_{0.5}Si_{0.5}$ trilayers *Appl. Phys. Lett.* **93** 122507

[130] Iwase T, Sakuraba Y, Bosu S, Saito K, Mitani S and Takanashi K 2009 Large interface spin-asymmetry and magnetoresistance in fully epitaxial Co_2MnSi/Ag/Co_2 MnSi current-perpendicular-to-plane magnetoresistive devices *Appl. Phys. Express* **2** 063003
[131] Yuasa H, Yoshikawa M, Kamiguchi Y, Koi K, Iwasaki H, Takagishi M and Sahashi M 2002 Output enhancement of spin-valve giant magnetoresistance in current-perpendicular-to-plane geometry *J. Appl. Phys.* **92** 2646–50
[132] Sakuraba Y, Izumi K, Iwase T, Bosu S, Saito K, Takanashi K, Miura Y, Futatsukawa K, Abe K and Shirai M 2010 Mechanism of large magnetoresistance in Co_2MnSi/Ag/Co_2MnSi devices with current perpendicular to the plane *Phys. Rev. B* **82** 094444
[133] Nakatani T M, Furubayashi T, Kasai S, Sukegawa H, Takahashi Y K, Mitani S and Hono K 2010 Bulk and interfacial scatterings in current-perpendicular-to-plane giant magnetoresistance with $Co_2Fe(Al_{0.5}Si_{0.5})$ Heusler alloy layers and Ag spacer *Appl. Phys. Lett.* **96** 212501
[134] Nakatani T M, Furubayashi T and Hono K 2011 Interfacial resistance and spin-dependent scattering in the current-perpendicular-to-plane giant magnetoresistance using $Co_2Fe(Al_{0.5Si0.5})$ Heusler alloy and Ag *J. Appl. Phys.* **109** 07B724
[135] Sato J, Oogane M, Naganuma H and Ando Y 2011 Large magnetoresistance effect in epitaxial $Co_2Fe_{0.4}Mn_{0.6}Si$/Ag/$Co_2Fe_{0.4}Mn_{0.6}Si$ devices *Appl. Phys. Express* **4** 113005
[136] Takahashi Y K, Srinivasan A, Varaprasad B, Rajanikanth A, Hase N, Nakatani T M, Kasai S, Furubayashi T and Hono K 2011 Large magnetoresistance in current-perpendicular-to-plane pseudospin valve using a $Co_2Fe(Ge_{0.5}Ga_{0.5})$ Heusler alloy *Appl. Phys. Lett.* **98** 152501
[137] Simalaotao K, Miura Y and Sakuraba Y 2024 Origin of the difference in spin-dependent transport properties between half-metallic $Co_2FeGa_{0.5}Ge0_{0.5}$and $Co_2Mn_{0.5}Fe_{0.5}Si$ with the Ag spacer *Phys. Rev. Mater.* **8** 104409
[138] Li S, Takahashi Y K, Furubayashi T and Hono K 2013 Enhancement of giant magnetoresistance by $L2_1$ ordering in $Co_2Fe(Ge_{0.5}Ga_{0.5})$ Heusler alloy current-perpendicular-to-plane pseudo spin valves *Appl. Phys. Lett.* **103** 042405
[139] Jung J W, Sakuraba Y, Sasaki T T, Miura Y and Hono K 2016 Enhancement of magnetoresistance by inserting thin NiAl layers at the interfaces in $Co_2FeGa_{0.5}Ge_{0.5}$/Ag/$Co_2FeGa_{0.5}Ge_{0.5}$ current-perpendicular-to-plane pseudo spin valves *Appl. Phys. Lett.* **108** 102408
[140] Chikaso Y, Inoue M, Tanimoto T, Kikuchi K, Yamanouchi M, Uemura T, Inubushi K, Nakada K, Shinya H and Shirai M 2022 Effect of off-stoichiometric composition on half-metallic character of $Co_2Fe(Ga,Ge)$ investigated using saturation magnetization and giant magnetoresistance effect *J. Appl. Phys.* **55** 345003
[141] Büker B, Jung J, Sasaki T, Sakuraba Y, Miura Y, Nakatani T, Hütten A and Hono K 2021 Elucidation of the strong effect of an interfacial monolayer on magnetoresistance in giant magnetoresistive devices with current perpendicular to the plane *Phys. Rev. B* **103** L140405
[142] Sakuraba Y, Ueda M, Miura Y, Sato K, Bosu S, Saito K, Shirai M, Konno T J and Takanashi K 2012 Extensive study of giant magnetoresistance properties in half-metallic $Co_2(Fe,Mn)Si$-based devices *Appl. Phys. Lett.* **101** 252408
[143] Barwal V, Suto H, Toyama R, Simalaotao K, Sasaki T, Miura Y and Sakuraba Y 2024 Large magnetoresistance and high spin-transfer torque efficiency of $Co_2Mn_xFe_{1-x}Ge$ ($0 \leqslant x \leqslant 1$) Heusler alloy thin films obtained by high-throughput compositional optimization using combinatorially sputtered composition-gradient film *APL Mater.* **12** 111114
[144] Fujita Y, Miura Y, Sasaki T, Nakatani T, Hono K and Sakuraba Y 2021 Spin-scattering asymmetry at half-metallic-ferromagnet|ferromagnet interface *Phys. Rev. B* **104** L140403
[145] Sakuraba Y, Izumi K, Koganezawa T, Bosu S, Okura R, Ueda M, Kojima T, Saito K and Takanashi K 2013 Fabrication of fully-epitaxial Co_2MnSi/Ag/Co_2MnSi giant magnetoresistive devices by elevated temperature deposition *IEEE Trans. Magn.* **49** 5464–8
[146] Chen J *et al* 2020 Fully epitaxial giant magnetoresistive devices with half-metallic Heusler alloy fabricated on poly-crystalline electrode using three-dimensional integration technology *Acta Mater.* **200** 1038–45
[147] Chen J, Liu J, Sakuraba Y, Sukegawa H, Li S and Hono K 2016 Realization of high quality epitaxial current- perpendicular-to-plane giant magnetoresistive pseudo spin-valves on Si(001) wafer using NiAl buffer layer *APL Mater.* **4** 056104
[148] Zhu J-G, Zhu X and Tang Y 2008 Microwave assisted magnetic recording *IEEE Trans. Magn.* **44** 125–31
[149] Bosu S, Sepehri-Amin H, Sakuraba Y, Hayashi M, Abert C, Suess D, Schrefl T and Hono K 2016 Reduction of critical current density for out-of-plane mode oscillation in a mag-flip spin torque oscillator using highly spin-polarized $Co_2Fe(Ga_{0.5}Ge_{0.5})$ spin injection layer *Appl. Phys. Lett.* **108** 072403
[150] Bosu S, Sepehri-Amin H, Sakuraba Y, Kasai S, Hayashi M and Hono K 2017 High frequency out-of-plane oscillation with large cone angle in mag-flip spin torque oscillators for microwave assisted magnetic recording *Appl. Phys. Lett.* **110** 142403
[151] Sepehri-Amin H, Zhou W, Bosu S, Abert C, Sakuraba Y, Kasai S, Suess D and Hono K 2019 Design of spin-injection-layer in all-in-plane spin-torque-oscillator for microwave assisted magnetic recording *J. Magn. Magn. Mater.* **476** 361–70
[152] Suto H, Nakatani T, Asam N, Iwasaki H and Sakuraba Y 2023 Evaluation of spin-transfer-torque efficiency using magnetization reversal against a magnetic field: comparison of FeCr with negative spin polarization and NiFe *Appl. Phys. Express* **16** 013003
[153] Özdoğan K, Galanakis I, Şaşioglu E and Aktas B 2006 Search for half-metallic ferrimagnetism in V-based Heusler alloys Mn_2VZ($Z \leqslant$ Al, Ga, In, Si, Ge, Sn) *J. Phys.* **18** 2905–14
[154] Suto H, Barwal V, Masuda K, Simalaotao K, Sasaki T, Miura Y, Tajiri H, Kumara L S R, Koganezawa T and Sakuraba Y 2024 Negative spin polarization and effect of composition on the atomic order and electronic structure of Mn_2VAl Heusler alloy thin films *Phys. Rev. Mater.* **8** 114408
[155] Suto H, Nakatani T, Kota Y, Asam N, Iwasaki H, Amemiya K, Mitsui T, Sakai S, Li S and Sakuraba Y 2022 Study on FeCr thin film for a spintronic material with negative spin polarization *J. Magn. Magn. Mater.* **557** 169474
[156] Suto H, Barwal V, Simalaotao K, Li Z, Masuda K, Sasaki T, Miura Y and Sakuraba Y 2024 Negative spin polarization of Mn_2VGa Heusler alloy thin films studied in current-perpendicular-to-plane giant magnetoresistance devices *J. Appl. Phys.* **135** 203901
[157] Hase N, Nakatani T M, Kasai S, Takahashi Y K, Furubayashi T and Hono K 2012 Effect of NiAl underlayer and spacer on magnetoresistance of current-perpendicular-to-plane spin valves using $Co_2Mn(Ga_{0.5}Sn_{0.5})$ Heusler alloy *J. Magn. Magn. Mater.* **324** 440–4
[158] Furubayashi T, Takahashi Y K, Sasaki T T and Hono K 2015 Enhancement of current-perpendicular-to-plane giant magnetoresistance in Heusler-alloy based pseudo spin valves by using a CuZn spacer layer *J. Appl. Phys.* **118** 163901
[159] Simalaotao K, Kurniawan I, Miura Y and Sakuraba Y 2025 Searching for Cu-. *X* spacers using a half-metallic $Co_2FeGa_{0.5}Ge_{0.5}$ electrode to boost magnetoresistance in CPP-GMR devices: a first-principles study *J. Appl. Phys.* **58** 395303
[160] Kubota T, Ina Y, Tsujikawa M, Morikawa S, Narisawa H, Wen Z, Shirai M and Takanashi K 2017 Current perpendicular-to-plane giant magnetoresistance devices using half-metallic $Co_2Fe_{0.4}Mn_{0.6}Si$ electrodes and a Ag-Mg spacer *J. Phys. D: Appl. Phys.* **50** 014004
[161] Taparia D *et al* 2024 Improvement in CPP-GMR read head sensor performance using [001]-oriented polycrystalline half-metallic Heusler alloy $Co_2FeGa_{0.5}Ge_{0.5}$ and CoFe bilayer electrode *Sci. Technol. Adv. Mater.* **25** 2388503

[162] Nikolaev K, Kolbo P, Pokhil T, Peng X, Chen Y, Ambrose T and Mryasov O 2009 "All-Heusler alloy" current-perpendicular-to-plane giant magnetoresistance *Appl. Phys. Lett.* **94** 222501
[163] Li S, Takahashi Y K, Sakuraba Y, Chen J, Furubayashi T, Mryasov O, Faleev S and Hono K 2016 Current-perpendicular-to-plane giant magnetoresistive properties in $Co_2Mn(Ge_{0.75}Ga_{0.25})/Cu_2TiAl/Co_2Mn(Ge_{0.75}Ga_{0.25})$ all-Heusler alloy pseudo spin valve *J. Appl. Phys.* **119** 093911
[164] Diao Z *et al* 2014 Half-metal CPPGMR sensor for magnetic recording *J. Magn. Magn. Mater.* **356** 73–81
[165] Nikolaev K, Anderson P, Kolbo P, Dimitrov D, Xue S, Peng X, Pokhil T, Cho H and Chen Y 2008 Heusler alloy based current-perpendicular-to-the-plane giant magnetoresistance heads for high density magnetic recording *J. Appl. Phys.* **103** 07F533
[166] Mizuno T, Tsuchiya Y, Machita T, Hara S, Miyauchi D, Shimazawa K, Chou T, Noguchi K and Tagami K 2008 Transport and magnetic properties of CPP-GMR sensor with CoMnSi Heusler alloy *IEEE Trans. Magn.* **44** 3584–7
[167] Carey M J, Maat S, Chandrashekariaih S, Katine J A, Chen W, York B and Childress J R 2011 Co_2MnGe-based current-perpendicular-to-the-plane giant-magnetoresistance spin-valve sensors for recording head applications *J. Appl. Phys.* **109** 093912
[168] Takagishi M, Yamada K, Iwasaki H, Fuke H N and Hashimoto S 2010 Magnetoresistance ratio and resistance area design of CPP-MR film for 25 Tb/in 2 read sensors *IEEE Trans. Magn.* **46** 2086–9
[169] Albuquerque G, Hernandez S, Kief M T, Mauri D and Wang L 2022 HDD reader technology roadmap to an areal density of 4 Tbpsi and beyond *IEEE Trans. Magn.* **58** 3100410
[170] Tsunoda M, Takahashi H, Nakamura T, Mitsumata C, Isogami S and Takahashi M 2010 Linear correlation between uncompensated antiferromagnetic spins and exchange bias in Mn–Ir/$Co_{100-x}Fe_x$ bilayers *Appl. Phys. Lett.* **97** 072501
[171] Page M R, Nakatani T M, Stewart D A, York B R, Read J C, Choi Y-S and Childress J R 2016 Temperature-dependence of current-perpendicular-to-the-plane giant magnetoresistance spin-valves using $Co_2(Mn_{1-x}\ Fe_x)Ge$ Heusler alloys *J. Appl. Phys.* **119** 153903
[172] Choi Y, Nakatani T, Read J C, Carey M J, Stewart D A and Childress J R 2017 Enhancement of current-perpendicular-to-plane giant magnetoresistance by insertion of amorphous ferromagnetic underlayer in Heusler alloy-based spin-valve structures *Appl. Phys. Express* **10** 013006
[173] Henke B L, Gullikson E M and Davis J C 1993 X-ray interactions: photoabsorption, scattering, transmission, and reflection at E = 50–30,000 eV, Z = 1–92 *At. Data Nucl. Data Tables* **54** 181–342
[174] Nakatani T, Krishna S, Singgappulige L, Kumara R, Tajiri H, Sakuraba Y and Hono K 2020 Thickness dependence of degree of B2 order of polycrystalline $Co_2(Mn_{0.6}Fe_{0.4})$ Ge Heusler alloy films measured by anomalous x-ray diffraction and its impacts on current-perpendicular-to-plane giant magnetoresistance properties *Scr. Mater.* **189** 63–66
[175] Nakatani T M, Du Y, Takahashi Y K, Furubayashi T and Hono K 2013 Structure and magnetoresistive properties of current-perpendicular-to-plane pseudo-spin valves using polycrystalline Co_2fe-based Heusler alloy films *Acta Mater.* **61** 3695–702
[176] Read J C, Nakatani T M, Smith N, Choi Y-S, York B R, Brinkman E and Childress J R 2015 Current-perpendicular-to-the-plane giant magnetoresistance in spin-valves with AgSn alloy spacers *J. Appl. Phys.* **118** 043907
[177] Yang Q, Holody P, Lee S-F, Henry L L, Loloee R, Schroeder P A, Pratt W P and Bass J 1994 Spin flip diffusion length and giant magnetoresistance at low temperatures *Phys. Rev. Lett.* **72** 3274–7
[178] Bass J and Pratt W P 2007 Spin-diffusion lengths in metals and alloys, and spin-flipping at metal/metal interfaces: an experimentalist's critical review *J. Phys.* **19** 183201
[179] Mihajlovi G, Nakatani T M, Smith N, Read J C, Choi Y, Tseng H and Childress J R 2015 Enhanced signal-to-noise ratio in current-perpendicular-to-plane giant-magnetoresistance sensors by suppression of spin-torque effects *IEEE Magn. Lett.* **6** 3001104
[180] Fukuzawa H, Yuasa H, Hashimoto S, Koi K, Iwasaki H, Takagishi M, Tanaka Y and Sahashi M 2004 MR ratio enhancement by NOL current-confined-path structures in CPP spin valves *IEEE Trans. Magn.* **40** 2236–8
[181] Fukuzawa H, Yuasa H, Hashimoto S, Iwasaki H and Tanaka Y 2005 Large magnetoresistance ratio of 10% by $Fe_{50}Co_{50}$ layers for current-confined-path current-perpendicular-to-plane giant magnetoresistance spin-valve films *Appl. Phys. Lett.* **87** 2005–7
[182] Fukuzawa H, Yuasa H and Iwasaki H 2007 CPP-GMR films with a current-confined-path nano-oxide layer (CCP-NOL) *J. Phys. D: Appl. Phys.* **40** 1213–20
[183] Sato Y, Hoshino K, Okamura S, Kato K and Hoshiya H 2010 Localized spin-torque effect in CPP-GMR sensor *IEEE Trans. Magn.* **46** 1610–3
[184] Shimazawa K, Tsuchiya Y, Mizuno T, Hara S, Chou T, Miyauchi D, MacHita T, Ayukawa T, Ichiki T and Noguchi K 2010 CPP-GMR film with ZnO-based novel spacer for future high-density magnetic recording *IEEE Trans. Magn.* **46** 1487–90
[185] Tsuchiya Y, Chou T, Matsuzawa H, Hara K S and Terunuma K N 2012 CPP-GMRFilm with GaOx based novel spacer *Intremag 2012* p HA–02
[186] Nakatani T, Mihajlović G, Read J C, Choi Y S and Childress J R 2015 High signal output in current-perpendicular-to-the-plane giant magnetoresistance sensors using In-Zn-O-based spacer layers *Appl. Phys. Express* **8** 093003
[187] Nakatani T, Sasaki T T, Li S, Sakuraba Y, Furubayashi T and Hono K 2018 The microstructural origin of the enhanced current-perpendicular-to-the-plane giant magnetoresistance by Ag/In-Zn-O/Zn spacer layer *J. Appl. Phys.* **124** 223904
[188] Nakatani T, Sasaki T T, Sakuraba Y and Hono K 2019 Improved current-perpendicular-to-plane giant magnetoresistance outputs by heterogeneous Ag-In:Mn-Zn-O nanocomposite spacer layer prepared from Ag-In-Zn-O precursor *J. Appl. Phys.* **126** 173904
[189] Sato J, Matsushita K and Imamura H 2008 Effective resistance mismatch and magnetoresistance of a CPP-GMR system with current-confined-paths *IEEE Trans. Magn.* **44** 2608–11
[190] Suto H, Katayama K, Tanaka Y, Taparia D, Nattamon S, Nakatani T and Sasaki T Hisato Yabuta and Yuya Sakuraba Excimer-laser-annealing-induced crystallization and atomic ordering of $Co_2Mn_{0.5}Fe_{0.5}Ge$ Heusler alloy thin films for spintronic applications *J. Appl. Phys.* **139** 083903 (Accepted 28 February 2026)
[191] Datta S and Das B 1990 Electronic analog of the electro-optic modulator *Appl. Phys. Lett.* **56** 665–7
[192] Tanaka M and Sugahara S 2007 MOS-based Spin Devices for Reconfigurable Logic *IEEE Trans. Electron. Devices* **54** 961–76
[193] Hamaya K and Yamada M 2022 Semiconductor spintronics with Co_2-Heusler compounds *MRS Bull.* **47** 584–92
[194] Hamaya K, Fujita Y, Yamada M, Kawano M, Yamada S and Sawano K 2018 Spin transport and relaxation in germanium *J. Phys. D: Appl. Phys.* **51** 393001
[195] Oltscher M, Eberle F, Kuczmik T, Bayer A, Schuh D, Bougeard D, Ciorga M and Weiss D 2017 Gate-tunable large magnetoresistance in an all-semiconductor spin valve device *Nat. Commun.* **8** 1807
[196] Bruski P, Manzke Y, Farshchi R, Brandt O, Herfort J and Ramsteiner M 2013 All-electrical spin injection and detection in the Co_2FeSi/GaAs hybrid system in the local and non-local configuration *Appl. Phys. Lett.* **103** 052406

[197] Bratkovsky A M 2008 Spintronic effects in metallic, semiconductor, metal–oxide and metal–semiconductor heterostructures *Rep. Prog. Phys.* **71** 026502
[198] Appelbaum I, Huang B and Monsma D J 2007 Electronic measurement and control of spin transport in silicon *Nature* **447** 295–8
[199] Lou X, Adelmann C, Crooker S A, Garlid E S, Zhang J, Reddy K S M, Flexner S D, Palmstrøm C J and Crowell P A 2007 Electrical detection of spin transport in lateral ferromagnet-semiconductor devices *Nat. Phys.* **3** 197–202
[200] Dery H, Dalal P, Cywiński Ł and Sham L J 2007 Spin-based logic in semiconductors for reconfigurable large-scale circuits *Nature* **447** 573–6
[201] Žutić I, Fabian J and Das S S 2004 Spintronics: Fundamentals and applications *Rev. Mod. Phys.* **76** 323
[202] Fert A and Jaffrès H 2001 Conditions for efficient spin injection from a ferromagnetic metal into a semiconductor *Phys. Rev. B* **64** 184420
[203] Tahara T, Koike H, Kameno M, Sasaki T, Ando Y, Tanaka K, Miwa S, Suzuki Y and Shiraishi M 2015 Room-temperature operation of Si spin MOSFET with high on/off spin signal ratio *Appl. Phys. Express* **8** 113004
[204] Kanaki T, Yamasaki H, Koyama T, Chiba D, Ohya S and Tanaka M 2018 Large current modulation and tunneling magnetoresistance change by a side-gate electric field in a GaMnAs-based vertical spin metal-oxide-semiconductor field-effect transistor *Sci. Rep.* **8** 7195
[205] Seabaugh A C and Zhang Q 2010 Low-voltage tunnel transistors for beyond CMOS logic *Proc. IEEE* vol 98 (Institute of Electrical and Electronics Engineers Inc.) pp 2095–110
[206] Ionescu A M and Riel H 2011 Tunnel field-effect transistors as energy-efficient electronic switches *Nature* **479** 329–37
[207] Tomioka K, Yoshimura M and Fukui T 2012 *2012 Symp. VLSI Technology (VLSIT)* (IEEE) pp 47–48
[208] Bernstein K, Cavin R K, Porod W, Seabaugh A and Welser J 2010 Device and Architecture Outlook for Beyond CMOS Switches *Proc. IEEE* **98** 2169–84
[209] Tarasov A S *et al* 2021 Asymmetric Interfaces in Epitaxial Off-Stoichiometric $Fe_{3+x}Si_{1-x}$/Ge/$Fe_{3+x}Si_{1-x}$ Hybrid Structures: Effect on magnetic and Electric Transport Properties *Nanomaterials* **12** 131
[210] Gaucher S, Jenichen B and Herfort J 2018 Ferromagnet/semiconductor/ferromagnet hybrid trilayers grown using solid-phase epitaxy *Semicond. Sci. Technol.* **33** 104005
[211] Gaucher S, Jenichen B, Kalt J, Jahn U, Trampert A and Herfort J 2017 Growth of Fe_3Si/Ge/Fe_3Si trilayers on GaAs(001) using solid-phase epitaxy *Appl. Phys. Lett.* **110** 102103
[212] Jenichen B, Herfort J, Jahn U, Trampert A and Riechert H 2014 Epitaxial Fe_3Si/Ge/Fe_3Si thin film multilayers grown on GaAs(001) *Thin Solid Films* **556** 120–4
[213] Maafa I, Hajjar-Garreau S, Jaafar R, Berling D, Pirri C, Mehdaoui A, Denys E, Florentin A and Garreau G 2013 Room-temperature ferromagnetism of all-epitaxial β-Fe–Ge/diamond–Ge/β-Fe–Ge trilayers *J. Phys.* **25** 256007
[214] Maafa I, Jaafar R, Hajjar-Garreau S, Berling D, Mehdaoui A, Pirri C, Deny E, Florentin A, Uhlaq-Bouillet C and Garreau G 2013 Interfacial properties of all-epitaxial Fe–Ge/Ge heterostructures on Ge(111) *Thin Solid Films* **545** 257–66
[215] Hamaya K, Murakami T, Yamada S, Mibu K and Miyao M 2011 Local structural ordering in low-temperature-grown epitaxial $Fe_{3+x}Si_{1-x}$ films on Ge(111) *Phys. Rev. B* **83** 144411
[216] Yamada S, Sagar J, Honda S, Lari L, Takemoto G, Itoh H, Hirohata A, Mibu K, Miyao M and Hamaya K 2012 Room-temperature structural ordering of a Heusler compound Fe_3Si *Phys. Rev. B* **86** 174406
[217] Hoffmann G, Herfort J and Ramsteiner M 2019 Spin generation in completely MBE-grown Co_2FeSi/MgO/GaAs lateral spin valves *Phys. Rev. Mater.* **3** 074402
[218] Manzke Y, Herfort J and Ramsteiner M 2017 Bias-dependent electrical spin generation in Fe_3Si/GaAs : Consistent behavior in nonlocal and local spin valves and in the three-terminal configuration *Phys. Rev. B* **96** 245308
[219] Ramsteiner M, Brandt O, Flissikowski T, Grahn H T, Hashimoto M, Herfort J and Kostial H 2008 Co_2FeSi/GaAs/(Al,Ga)As spin light-emitting diodes: Competition between spin injection and ultrafast spin alignment *Phys. Rev. B* **78** 121303
[220] Herfort J, Schönherr H-P, Friedland K-J and Ploog K H 2004 Structural and magnetic properties of epitaxial Fe_3Si/GaAs(001) hybrid structures *J. Vac. Sci. Technol. B* **22** 2073–8
[221] Herfort J, Schönherr H-P and Ploog K H 2003 Epitaxial growth of Fe_3Si/GaAs(001) hybrid structures *Appl. Phys. Lett.* **83** 3912–4
[222] Niculescu V A, Burch T J and Budnick J I 1983 A local environment description of hyperfine fields and atomic moments in $Fe_{3-x}T_xSi$ alloys *J. Magn. Magn. Mater.* **39** 223–67
[223] Hines W A, Menotti A H, Budnick J I, Burch T J, Litrenta T, Niculescu V and Raj K 1976 Magnetization studies of binary and ternary alloys based on Fe_3Si *Phys. Rev. B* **13** 4060–8
[224] Bansil A, Kaprzyk S, Mijnarends P E and Toboła J 1999 Electronic structure and magnetism of $Fe_{3-x}V_xX$ (X = Si, Ga, and A)alloys by the KKR-CPA method *Phys. Rev. B* **60** 13396–412
[225] Yamada S, Tanikawa K, Miyao M and Hamaya K 2012 Atomically Controlled Epitaxial Growth of Single-Crystalline Germanium Films on a Metallic Silicide *Cryst. Growth Des.* **12** 4703–7
[226] Ueda K, Ando Y, Kumano M, Sadoh T, Maeda Y and Miyao M 2008 Low temperature formation of multi-layered structures of ferromagnetic silicide Fe_3Si and Ge *Appl. Surf. Sci.* **254** 6215–7
[227] Kawano M, Yamada S, Tanikawa K, Sawano K, Miyao M and Hamaya K 2013 An ultra-thin buffer layer for Ge epitaxial layers on Si *Appl. Phys. Lett.* **102** 121908
[228] Ikawa M, Kawano M, Sakai S, Yamada S, Kanashima T and Hamaya K 2017 Influence of the Ge diffusion on the magnetic and structural properties in Fe_3Si and CoFe epilayers grown on Ge *J. Cryst. Growth* **468** 676–9
[229] Kawano M, Ikawa M, Santo K, Sakai S, Sato H, Yamada S and Hamaya K 2017 Electrical detection of spin accumulation and relaxation in p -type germanium *Phys. Rev. Mater.* **1** 034604
[230] Sakai S, Kawano M, Ikawa M, Sato H, Yamada S and Hamaya K 2017 Low-temperature growth of fully epitaxial CoFe/Ge/Fe_3Si layers on Si for vertical-type semiconductor spintronic devices *Semicond. Sci. Technol.* **32** 094005
[231] Shiihara T, Yamada M, Honda M, Yamada A, Yamada S and Hamaya K 2020 Spin transport in antimony-doped germanium detected using vertical spin-valve structures *Appl. Phys. Express* **13** 023001
[232] Honda M, Shiihara T, Yamada M, Yamada S and Hamaya K 2020 Germanium pn junctions between ferromagnetic CoFe and Fe_3Si layers for spintronic applications *Mater. Sci. Semicond. Process.* **116** 105066
[233] Yamada A, Yamada M, Honda M, Yamada S, Sawano K and Hamaya K 2021 Magnetoresistance ratio of more than 1% at room temperature in germanium vertical spin-valve devices with Co_2FeSi *Appl. Phys. Lett.* **119** 192404
[234] Kawano M, Ikawa M, Arima K, Yamada S, Kanashima T and Hamaya K 2016 All-epitaxial Co_2FeSi/Ge/Co_2FeSi trilayers fabricated by Sn-induced low-temperature epitaxy *J. Appl. Phys.* **119** 045302

[235] Yamada A, Yamada M, Shiihara T, Ikawa M, Yamada S and Hamaya K 2021 Experimental estimation of the spin diffusion length in undoped. *p* -Ge on Fe_3Si using vertical spin-valve devices *J. Appl. Phys.* **129** 013901
[236] Yamada M, Tsukahara M, Fujita Y, Naito T, Yamada S, Sawano K and Hamaya K 2017 Room-temperature spin transport in n-Ge probed by four-terminal nonlocal measurements *Appl. Phys. Express* **10** 093001
[237] Watahiki S, Yamada S, Obinata S, Kikuoka S, Yamada M, Sawano K and Hamaya K 2026 Lateral spin-valve devices on germanium on insulator Materials Science in Semiconductor Processing **209** 110602
[238] Hamaya K, Hashimoto N, Oki S, Yamada S, Miyao M and Kimura T 2012 Estimation of the spin polarization for Heusler-compound thin films by means of nonlocal spin-valve measurements: Comparison of Co_2FeSi and Fe_3Si *Phys. Rev. B* **85** 100404
[239] Yamada A, Yamada M, Kusumoto S, Do Nascimento J A, Murrill C, Yamada S, Sawano K, Lazarov V K and Hamaya K 2024 Growth of all-epitaxial Co_2MnSi/Ge/Co_2MnSi vertical spin-valve structures on Si *Mater. Sci. Semicond. Process.* **173** 108140
[240] Yamada M, Kusumoto S, Yamada A, Sawano K and Hamaya K 2024 Effect of Sn doping on low-temperature growth of Ge epilayers on half-metallic Co_2FeSi *Mater. Sci. Semicond. Process.* **171** 107987
[241] Fetzer R *et al* 2015 Spin-resolved low-energy and hard x-ray photoelectron spectroscopy of off-stoichiometric Co_2MnSi Heusler thin films exhibiting a record TMR *J. Phys. D: Appl. Phys.* **48** 164002
[242] Yamada M, Kuroda F, Tsukahara M, Yamada S, Fukushima T, Sawano K, Oguchi T and Hamaya K 2020 Spin injection through energy-band symmetry matching with high spin polarization in atomically controlled ferromagnet/ferromagnet/semiconductor structures *NPG Asia Mater.* **12** 47
[243] Yamada S, Kato M, Ichikawa S, Yamada M, Naito T, Fujiwara Y and Hamaya K 2023 Half-Metallic Heusler Alloy/GaN Heterostructure for Semiconductor Spintronics Devices *Adv. Electron. Mater.* **9** 2300045
[244] Lin Z, Pan D, Rasly M and Uemura T 2019 Electrical spin injection into AlGaAs/GaAs-based two-dimensional electron gas systems with Co_2MnSi spin source up to room temperature *Appl. Phys. Lett.* **114** 012405
[245] Kudo K, Yamada S, Yafuso M, Kimura T, Lazarov V K and Hamaya K 2021 Half-metallic nature of the low-temperature grown Co_2MnSi films on $SrTiO_3$ *J. Alloys Compd.* **854** 155571
[246] Watahiki S, Kusumoto S, Yamada A, Obinata S, Yamada S, Kikuoka S, Yamada M, Sawano K and Hamaya K 2025 Observation of room-temperature magnetoresistance effect in $Co_2Fe(Al,Si)$/Ge/Co_2FeSi vertical spin-valve devices on Si *Mater. Sci. Semicond. Process.* **199** 109809
[247] Kohda M, Ohno Y, Takamura K, Matsukura F and Ohno H 2001 A Spin Esaki Diode *Jpn. J. Appl. Phys.* **40** L1274–6
[248] Oltscher M, Ciorga M, Utz M, Schuh D, Bougeard D and Weiss D 2014 Electrical Spin Injection into High Mobility 2D Systems *Phys. Rev. Lett.* **113** 236602
[249] Thanh Tu N, Otsuka T, Arakawa Y, Anh L D, Tanaka M and Hai P N 2022 Spin transport in fully ferromagnetic. *p–n* junctions *J. Appl. Phys.* **131** 013902
[250] Oki K, Ueda S, Usami T, Fujii S, Kikuoka S, Yamamoto K, Sawano K and Hamaya K 2025 Room-temperature spin transport through band-to-band tunneling at semiconductor *p-n* junctions *Phys. Rev. Appl.* **23** L051005